ROYAUME DU MAROC
Université Mohammed V - RABAT -
جامعة محمد الخامس – الرباط –
Faculté des sciences
كلية العلوم
CENTRE D'ÉTUDES DOCTORALES - SCIENCES ET TECHNOLOGIES

N° d'ordre : 4120

THÈSE

en vue de l'obtention du : **DOCTORAT**

Structure de Recherche : Laboratoire de Matière Condensée et Sciences Interdisciplinaires : Unité de Recherche Labellisée CNSRT
Discipline : Physique
Spécialité : Physique des particules

Présentée et Soutenue le : 12 / 07 / 2025
par :

Asmaa ABOULHORMA

Exploring a new scalar particle with the ATLAS experiment at CERN's Large Hadron Collider and investigating jet energy resolution in the forward region with the HGTD

Devant le JURY :

Yassine HASSOUNI	**PES, Faculté des Sciences, Université Mohammed V,Rabat**	**Président**
Mohamed CHABAB	**PES, Faculté des Sciences Semlalia, Université Cadi Ayyad, Marrakech**	**Rapporteur/ Examinateur**
Hamid EZ-ZAHRAOUY	**PES, Faculté des Sciences, Université Mohammed V, Rabat**	**Rapporteur/ Examinateur**
Morad EL BAZ	**PES, Faculté des Sciences, Université Mohammed V, Rabat**	**Rapporteur/ Examinateur**
Mohammed LOULIDI	**PES, Faculté des Sciences, Université Mohammed V, Rabat**	**Examinateur**
Abdesslam ARHRIB	**PES, Faculté des Sciences et Techniques, Tanger**	**Invité**
Kétévi Adikle ASSAMAGAN	**Physicien chercheur, Brookhaven National Laboratory, États-Unis**	**Co-director de thèse**
Farida FASSI	**PES, Université Mohammed V, Faculté des Sciences,Rabat**	**Directrice de thèse**

Année Universitaire : 2024 - 2025

Dedication

With all my heart, I dedicate this work to the memory of my dear father, whose values, strength, and aspirations have been a guiding light throughout my life. Every step of this journey has been inspired by the desire to honor him, and his memory has remained my greatest source of motivation and resilience. I also wish to express my deepest gratitude to my mother for her boundless love, sacrifices, and unwavering support. Above all, I dedicate this thesis to my sister, Najia Aboulhorma, who has truly been like a mother to me. Her steadfast support, love, and selflessness have made everything possible. Without her encouragement and presence, none of this would have been achievable. This work stands above all as a tribute to her remarkable strength and devotion.

I would like to extend my special thanks to all the colleagues I have worked with within the ATLAS collaboration, as well as those from other collaborations during this period. Their team spirit, availability, and the richness of our scientific exchanges have greatly contributed to the completion of this work. I have learned a great deal alongside them, and I am grateful for their support and friendship.

Acknowledgements

I would like to express my heartfelt gratitude to the Laboratory of Condensed Matter and Interdisciplinary Sciences (Unit of Research Labeled CNSRT), directed by **Prof. Hamid EZ-ZAHRAOUY**, for providing an excellent scientific environment and all the necessary resources for the successful completion of this work. The lab's unwavering support and outstanding facilities have played a pivotal role in the progress of my research.

I also extend my sincere thanks to the **ATLAS Collaboration** for their tremendous support and for granting access to invaluable data that was essential for this thesis.

My deepest appreciation goes to **Prof. Farida FASSI**, PES, Faculty of Sciences, Mohammed V University, Rabat, my thesis director. Her guidance, dedication, and commitment to academic excellence have profoundly shaped the course of my work and personal growth.

I am also very grateful to **Dr. Kétévi Adikle ASSAMAGAN**, Research Physicist, Brookhaven National Laboratory, États-Unis, my thesis co-director, whose expertise and encouragement have been instrumental at every stage of this journey.

I would like to thank **Prof. Yassine HASSOUNI**, PES, Faculty of Sciences, Mohammed V University, Rabat, President of the jury, for his exceptional leadership, insightful evaluation, and constructive feedback that greatly contributed to the scholarly rigor of this thesis.

My sincere thanks to **Prof. Mohamed CHABAB**, PES, Faculty of Sciences Semlalia, Cadi Ayyad University, Marrakech, Reviewer/Examiner, for his thorough review, pertinent remarks, and thoughtful assessment.

Special thanks to **Prof. Morad EL BAZ**, PES, Faculty of Sciences, Mohammed V University, Rabat, Reviewer/Examiner, for his meticulous evaluation and valuable suggestions that enriched this work.

I am truly grateful to **Prof. Hamid EZ-ZAHRAOUY**, PES, Faculty of Sciences, Mohammed V University, Rabat, Reviewer/Examiner, for his scientific leadership and insightful guidance throughout the research process.

Warm thanks to **Prof. Mohammed LOULIDI**, PES, Faculty of Sciences, Mo-

hammed V University, Rabat, Examiner, for his careful evaluation and constructive comments that contributed to the quality of this thesis.
Each of these distinguished professors and researchers played a vital role in the completion of this thesis. Their collective expertise, encouragement, and commitment were instrumental to my academic journey, and I am sincerely honored and grateful for their support.

Abrégé

Cette thèse s'inscrit dans le cadre de la recherche de nouvelles particules au-delà du Modèle Standard, en s'appuyant sur les données de l'expérience ATLAS au Grand Collisionneur de Hadrons (LHC). L'analyse se concentre sur la recherche de bosons vecteurs sombres (Z_d) et de nouveaux scalaires (S), à travers deux états finaux complémentaires : le canal entièrement leptonique ($Z_dZ_d \to 4\ell$) et le canal semi-leptonique ($Z_dZ_d \to 2\ell 2j$). Pour maximiser la sensibilité aux signaux recherchés, des techniques avancées de sélection d'événements et de reconstruction sont mises en œuvre. Les résultats sont interprétés dans le cadre du Modèle de Higgs Abélien Caché.
Parallèlement à cette étude phénoménologique, la thèse comprend un volet instrumental dédié à l'amélioration des performances du détecteur ATLAS dans les conditions d'interactions multiples (pileup) attendues au LHC à haute luminosité. Des études sont menées sur l'échelle énergétique et la résolution des jets pour le Détecteur Temporel à Haute Granularité (HGTD), mettant en évidence des gains significatifs dans la région avant ($2.4 < \eta < 4$). En complément, une analyse des performances thermiques des modules à bandes du trajectographe interne (ITk), réalisée au Brookhaven National Laboratory (BNL), permet de contribuer à l'optimisation de la reconstruction des traces et des performances globales du détecteur dans un environnement à pileup élevé.

Mots-clefs: LHC, nouvelle physique, matière noire, au-delà du modèle standard, expérience ATLAS.

Abstract

This thesis is dedicated to the search for new particles beyond the Standard Model, based on data from the ATLAS experiment at the Large Hadron Collider (LHC). The analysis focuses on the search for dark vector bosons (Zd) and new scalar particles (S), through two complementary final states: the fully leptonic channel (ZdZd$\rightarrow$ 4ℓ) and the semi-leptonic channel (ZdZd$\rightarrow$2ℓ2j). Advanced event selection and reconstruction techniques are employed to maximize sensitivity to the targeted signals. The results are interpreted within the framework of the Hidden Abelian Higgs Model. In parallel with this phenomenological study, the thesis includes an instrumental component aimed at enhancing the ATLAS detector's performance under the high pileup conditions expected at the High-Luminosity LHC. Studies of the energy scale and jet resolution for the High Granularity Timing Detector (HGTD) show significant improvements in the forward region (2.4$<\eta<$4). Additionally, thermal performance analyses of strip modules for the Inner Tracker (ITk), conducted at Brookhaven National Laboratory (BNL), contribute to the optimization of track reconstruction capabilities and the overall detector performance in a high pileup environment.

Keywords:: LHC, New physics, Dark matter, Beyond Standard Model, ATLAS experiment.

Résumé détaillé

Cette thèse s'inscrit pleinement dans le cadre de la recherche de nouvelles physiques au-delà du Modèle Standard (MS), en étudiant plus précisément la présence de bosons vectoriels sombres (Z_d) et de nouveaux scalaires (S) à l'aide des données collectées par l'expérience ATLAS au LHC. Malgré son succès prédictif indéniable, le Modèle Standard reste incomplet : il ne rend pas compte de la nature de la matière noire, de l'asymétrie matière-antimatière, ni d'autres phénomènes cosmologiques majeurs. Ces limitations motivent l'exploration de théories alternatives, dont le modèle du Higgs abélien invisible constitue un exemple prometteur. Ce modèle introduit un secteur sombre couplé faiblement au secteur visible via la brisure d'une symétrie supplémentaire ($U(1)'$), conduisant à l'apparition de nouveaux états massifs tels que le boson Z_d et le scalaire singulet S.

Motivation et Cadre Théorique

Dans le modèle considéré, le scalaire S agit comme un portail entre les secteurs visible et sombre, permettant la production de paires de bosons Z_d via le processus $S \to Z_d Z_d$. Cette chaîne de désintégration offre un signal expérimental particulièrement intéressant, dans la mesure où les Z_d peuvent se désintégrer en leptons ou en quarks, générant ainsi deux topologies signatures dans ATLAS :

- Le canal entièrement leptonique ($Z_d Z_d \to 4\ell$, avec $\ell = e, \mu$), caractérisé par la présence de quatre leptons isolés dans l'état final.
- Le canal semi-leptonique ($Z_d Z_d \to 2\ell 2j$), composé de deux leptons et de deux jets hadroniques.

L'intérêt de combiner ces deux canaux réside dans leur complémentarité en termes de sensibilité, la topologie semi-leptonique permettant notamment d'explorer des masses de Z_d plus faibles, tandis que le canal leptonique confère une grande pureté au signal.

Sélection et Analyse des Événements

L'analyse s'appuie sur les données du Run 2 du LHC, soit une collision proton-proton à $\sqrt{s} = 13$ TeV couvrant une large gamme de masses pour le nouveau secteur. La sélection des événements repose sur :

- Une identification fine des leptons et jets, exploitant les algorithmes les plus récents de reconstruction et d'isolation,
- Des variables discriminantes comme le rapport des masses invariantes $m_{\ell\ell}/m_{jj}$, sensibles à la cinématique spécifique du processus $S \to Z_d Z_d$,
- Des techniques d'intelligence artificielle (multivariées), telles que les BDT (Boosted Decision Trees), pour optimiser la séparation signal/bruit de fond en exploitant des corrélations complexes entre variables observables.

Une attention particulière est portée à la maîtrise des bruits de fond majeurs, principalement issus des processus standards produisant quatre leptons ou deux leptons et deux jets (ZZ, $t\bar{t}$, etc.), via l'usage de régions de contrôle dédiées et une estimation systématique des incertitudes associées.

Développements Instrumentaux

Sur le plan instrumental, la thèse a comporté un important volet R&D visant à préparer les détecteurs d'ATLAS au défi du HL-LHC, où le taux d'empilement d'événements (pile-up) atteindra des niveaux inédits. Deux sous-détecteurs de pointe ont été étudiés :

- **Le High-Granularity Timing Detector (HGTD)** : ce détecteur permet une mesure précise du temps de vol des particules, avec une résolution temporelle de 30 ps pour les particules faiblement ionisantes. Cette performance exceptionnelle se traduit par une amélioration significative de la résolution des jets dans la zone avant du détecteur ($2.4 < \eta < 4.0$), ainsi qu'une capacité accrue à rejeter l'empilement grâce à la séparation temporelle des interactions.
- **Le trajectographe interne ITk (Inner Tracker)** : des tests thermiques menés au Brookhaven National Laboratory ont permis de valider la robustesse et la stabilité des modules de silicium de l'ITk face à des conditions extrêmes de radiation et de flux de particules. Ces performances sont cruciales pour assurer une reconstruction fiable des traces à haute luminosité.

Ces développements instrumentaux conditionnent la capacité future d'ATLAS à maintenir voire améliorer la sensibilité aux nouveaux phénomènes, en particulier dans la recherche de signatures discrètes et rares telles que celles du secteur sombre.

Résultats et Portée

L'analyse des données du Run 2 a permis d'établir de nouvelles limites expérimentales sur la section efficace du processus $S \to Z_d Z_d$, selon divers scénarios de masse pour S et Z_d. Ces résultats contraignent significativement l'espace des paramètres du modèle abélien invisible, et définissent des bases solides pour les recherches futures avec les données du HL-LHC.

La combinaison des approches phénoménologique et instrumentale permet de tirer le meilleur parti de la physique exploratoire actuelle tout en anticipant les défis technologiques à venir. Les progrès accomplis dans cette thèse démontrent non seulement la faisabilité de rechercher des signatures du secteur sombre dans les données du LHC, mais également l'importance capitale de l'innovation instrumentale pour en repousser les limites.

En somme, ce travail contribue de manière significative à la quête de nouvelles particules au-delà du Modèle Standard, en mettant en œuvre des outils analytiques de pointe et en participant activement au développement des futurs détecteurs d'ATLAS. Il établit des bases solides pour de futures investigations dans des régions encore inexplorées de la physique des particules.

List of publications

- ATLAS Collaboration."Search for a new scalar decaying into new spin-1 bosons in four-lepton final states with the ATLAS detector", arXiv:2410.16781. Phys. Lett. B 865 (2025) 139472.[1]
- ATLAS Collaboration. "Search for new $spin^{-0}$ or $spin^{-1}$ particles in four-lepton final states with the ATLAS detector with 139 fb^{-1} of pp collision data at $\sqrt{s} = 13$ TeV. JHEP: 03 (2022) 041 [2].
- ATLAS Collaboration. "Measurement of ZZ production cross-sections in the four-lepton final state in pp collisions at $\sqrt{s} = 13.6$ TeV with the ATLAS experiment". arXiv: 2311.09715 [hep-ex] (Nov. 2023) [3].
- ATLAS Collaboration. "Measurement of the Higgs boson mass in the $H \to ZZ^* \to 4\ell$ decay channel using 139 fb^{-1} of $\sqrt{s} = 13$ TeV pp collisions recorded by the ATLAS detector at the LHC". Physics Letters B 843, 137880. issn: 0370-2693. (Aug. 2023) [4].
- Asmaa Aboulhorma, on behalf of the ATLAS HGTD Collaboration. "A High-Granularity Timing Detector for the ATLAS Phase-II upgrade." Proceedings of Science (LHCP2021) 176 (2021). The Ninth Annual Conference on Large Hadron Collider Physics - LHCP2021, 7-12 June 2021, Online. [5].
- Asmaa Aboulhorma and Farida Fassi. "Jet Energy Scale and Resolution in the High-Granularity Timing Detector in ATLAS Upgrades at HL-LHC." Andromeda Proceedings, BSM 2021, Online. DOI: 10.31526/ACP.BSM-2021.5[6].
- ATLAS Collaboration. "Search for new phenomena in events with an energetic jet and missing transverse momentum in pp collisions at $\sqrt{s} = 13$ TeV with the ATLAS detector". Physical Review D 103. issn: 2470-0029(2021) [7].

- Scopus author ID: 57246251500
- ORCID: 0000-0002-9987-2292
- INSPIRE ID: 1910447

Contribution

Throughout my thesis, I actively participated in the following tasks:

High Granularity Timing Detector (HGTD) Studies:

- Developed an algorithm to improve the jet energy resolution in the forward region using HGTD by reducing the pileup track contamination in hard-scatter jets from nearby pileup interactions
- Studied particle-flow reconstruction in the forward region and investigated the impact of HGTD in reducing pileup track contamination
- Evaluated performance in terms of jet energy response and resolution as a function of jet p_T, η, and pileup density
- Documented the code in `GIT` and created comprehensive documentation on a Twiki for both experts and users

Dark Sector Studies with the 4-Lepton Final State:

- Worked on cut flow optimization for the 4-lepton channel to improve signal sensitivity
- Contributed to regenerating the limit setting framework for dark sector searches

Development of 2-Lepton 2-Jet Analysis Framework:

- Served as the contact person for the $2\ell 2j$ analysis
- Worked on the complete $2\ell 2j$ analysis chain, developing all steps from job option configuration to final results
- Generated Monte Carlo samples for signal and background processes

- Conducted truth-level studies for lepton and jets selection to optimize acceptance
- Developed and optimized cut flow for jet selection to maximize signal efficiency while reducing background
- Performed TMVA (Toolkit for Multivariate Analysis) studies for both dijet selection and background rejection
- Implemented data-driven background estimation techniques for major background sources
- Updated the Z_dZ_d analysis framework to accommodate recent developments in event reconstruction, ensuring compatibility with new algorithms and improved performance in signal selection and background suppression

Development of Slow Control System for ITk Strip Stave Thermal Cycling:

- Created a Python script to gather data from a USB temperature logger and two humidity sensors, capturing:
  - Eight temperature measurements
  - Two humidity values
- The instrumentation interfaces with two parallel boxes designed for two ITk strip staves
- Explored the effects of thermal cycling on the operational efficiency of the Inner Tracker stave within a coldbox
- Implemented a USB logger for comprehensive measurements of:
  - Four temperature points
  - Two humidity sensors

List of Figures

1.1 Standard Model elementary particles [8]. 5
1.2 Feynman diagrams for the main Higgs boson production modes. . . . 9
1.3 (a) Cross-sections for different Higgs boson production modes at a proton-proton collider with a centre-of-mass energy of 6–15 TeV. (b) A Higgs boson mass of 125 GeV is assumed in this plot. cross-sections as a function of Higgs boson mass are shown [12]. 11
1.4 Higgs boson branching ratio of the possible Higgs boson decay channels as a function of the Higgs boson mass [13]. 12
1.5 Feynman diagrams for $H \to \gamma\gamma$ decay 12
1.6 The distribution of the four-lepton invariant mass, m4l, for the selected candidates, compared to the background expectation in the 80-250GeV mass range, $\sqrt{s} = 7$ TeV $\sqrt{s} = 8$ TeV data in both ATLAS (a) [15] and CMS (b) [16] detectors, the signal expectation for a SM Higgs with $m_H = 125GeV$ is also shown. 13
1.7 Possible dark matter detection methods. 14
1.8 Four-lepton decay modes of the Higgs boson through Z and dark Z intermediaries, demonstrating hypercharge and Higgs portal couplings. 17
1.9 Constraints on ε for pure kinetic mixing for $m_{Z_d} \sim$ MeV $-$ 60 GeV. The black dashed line separates prompt ($c\tau < 1\mu$m) from non-prompt Z_d decays. The three blue lines are contours of Br($H \to ZZ_d$) of 10^{-4}, 10^{-5}, 10^{-6} respectively [22]. 19
1.10 Branching Ratios ($a \to f\bar{f}$) in 2HDM+S Model Type I. Decays to quarkonia likely invalidate our simple calculations in the shade regions [22]. 21
1.11 Branching Ratios ($a \to f\bar{f}$) in 2HDM+S Model Type II . Decays to quarkonia likely invalidate our simple calculations in the shade regions [22]. 22

1.12 Branching Ratios ($a \to f\bar{f}$) in 2HDM+S Model Type III . Decays to quarkonia likely invalidate our simple calculations in the shade regions [22]. 22
1.13 Pseudoscalar Branching Ratios ($a \to f\bar{f}$) in 2HDM+S Model Type IV. Decays to quarkonia likely invalidate our simple calculations in the shade regions [22]. 23

2.1 Overview of CERN's accelerator complex showing the proton acceleration chain through LINAC 2, Booster, PS, and SPS before injection into the LHC ring, where four major experiments are positioned at beam intersection points [34]. 26
2.2 Cut-away view of the ATLAS detector [40]. 27
2.3 The ATLAS Coordinate System, showing the x, y, and z axes, as well as the angles ϕ and η, and the location of other LHC experiments[40]. 28
2.4 Structure of the ATLAS ID and particle track reconstruction [41]. . . 29
2.5 Cutaway view of the ATLAS calorimeter system [43]. 32
2.6 Sketch of a barrel module in the electromagnetic calorimeter at $\eta = 0$. The granularities of the cells in three different layers in η and ϕ are also shown [44]. 33
2.7 Sketch of a barrel module in the tile Calorimeter, showing the major components of the optical read-out, including the tiles, the fibers and the PMTs [45]. 35
2.8 The general layout of the ATLAS Muon Spectrometer [46]. 37
2.9 The core LHC program and the upcoming HL-LHC operation 39
2.10 Schematic layout of the ITk for HL-LHC phase of ATLAS [52]. . . . 41
2.11 Layout and sensor performance of the HGTD [54]. 42
2.12 Layout and sensor performance of the HGTD [54]. 43

3.1 Schematic view of the electron path through the detector [57]. 47
3.2 The electron identification efficiency in $Z \to e^+e^-$ events as function of E_T (a) and as function of η (b) for the three Working Points, (WPs): Loose, Medium, and Tight [58]. 48
3.3 The transformed LH-based identification discriminant dL for reconstructed electron candidates with good quality tracks with $30GeV < E_T < 35GeV$ and $|\eta| < 0.6$, where the signal is for prompt electrons in a $Z \to ee$ process [58]. 49

3.4 Muon-identification efficiency, as a function of η (left) and p_{T} (right), for three different selections (`Loose`, `Medium`, and `Tight`) WPs requirements in simulated $t\bar{t}$ events, shown separately for prompt muons and muons from light hadron decays [60]. 52
3.5 Illustration of the anti-k_t algorithm [62]. 53
3.6 E_T^{miss} distribution comparison in $Z + jet$ events where no genuine E_T^{miss} is expected due to neutrino non-reconstruction [72]. 58

4.1 (a): Current and HL-LHC local pileup vertex density. (b): The resolution of the longitudinal track impact parameter, Z_0, as a function of η for different p_T values [73]. 61
4.2 Position and time of the interaction points during a single bunch crossing $< \mu >= 200$ [6]. 62
4.3 Illustration of the HGTD.The blue represent the active region and the green the off detector electronic [74]. 64
4.4 The HGTD hybrid module with its associated flexible reading cable tail [74]. 64
4.5 The orientation of the readout rows for the first and second layer encountered by a particle, separately and with the overlay of both. Each layer is rotated in alternating directions by 20° . In the figures the staves of the three rings are separated by the circular lines [74]. . 65
4.6 The schematic drawing shows the overlap between the modules on the front and back of the cooling disk. There is a sensor overlap of 20% for $r > 470mm$, 54% for $230mm < r < 470mm$ and 70 % for $r < 230mm$ [74]. 66
4.7 (a) A diagram showing the cross-sectional view of an LGAD [74]. (b) A simulated current signal for an LGAD sensor measuring 50 m in thickness. [75]. 67
4.8 Schematic of a single pixel readout [76]. 69
4.9 All tracks associated with primary vertices illustrating the PU contamination [6]. 70
4.10 (a) show JER as a function of η and as a function of $p_{T_{truth}}$ is illustrated in (b), for raw calorimeter jets [6]. 71
4.11 (a) show The transverse jet energy resolution as a function of η, and as a function of $p_{T_{truth}}$ is illustrated in (b), for raw calorimeter jets [6]. 72
4.12 (a) show the JER as a function of η and as a function of $p_{T_{truth}}$ (b) before and after correction [6]. 73

4.13 (a) show the transverse jet energy resolution as a function of η and as a function of $p_{T_{truth}}$ (b) before and after correction [6]. 74

5.1 Layout of the ATLAS ITk detector. 77
5.2 Sketch of barrel short strip stave. 78
5.3 View of Short-Strip Module. 79
5.4 Prototype modules of LS (a) and SS (b). 80
5.5 Coldbox (a) with a stave installed inside (b). 82
5.6 USB TC-08 data logger (a) with Type K thermocouple (b). 83
5.7 USB TC-08 data logger (a) with Type K thermocouple (b). 83
5.8 A peripheral interface overview of the Raspberry Pi4. 84
5.9 setup used for the thermal cycle testing at the BNL clean room. . . . 85
5.10 The humidity (top) and temperature (down) variations during the thermal cycle testing of the stave in the function of the measurement's time. 86
5.11 Real-Time Monitoring of Stave Thermal Cycling and Humidity Trends Using Grafana 87
5.12 Electrical Performance During Thermal Cycling: HV, LV, and AMAC Current Analysis. 88

6.1 $E'_{ab}/m_{4\ell}$ distributions for additional scalar signal hypotheses and the two leading SM background processes. The dotted lines delimit the cut applied using this variable. 95
6.2 Width of the SM Higgs boson compared to that of a BSM dark Higgs boson as a function of mass. 99
6.3 Distributions of $\langle m_{\ell\ell}\rangle = \frac{1}{2}(m_{ab}+m_{c,d})$ in validation region 3 in 2015–8 data and MC for the $4e$ channel (top left), the 4μ channel (top right), the $2e2\mu$ channel (bottom left), and all channels combined (bottom right). In this region, events are required to have $m_{4\ell}$ outside of the $115 < m_{4\ell} < 130\,\text{GeV}$ window and pass the inverted "medium SR" cut. 103
6.4 Width of the SM Higgs boson compared to that of a BSM dark Higgs boson as a function of mass. 104
6.5 Distributions of the average dilepton mass $\langle m_{\ell\ell}\rangle = \frac{1}{2}(m_{ab}+m_{cd})$ for the two signal regions (a) SR1 and (b) SR2. The hatched bands show the uncertainty in the background prediction. The uncertainties on the data points are asymmetric Poisson errors (Eqs. (40.76a) and (40.76b) 112

6.6 Distributions of the total invariant mass $m_{4\ell}$ for the two signal regions (a) SR1 and (b) SR2. In (a), the requirement $m_{4\ell} < 115$ GeV is not applied, but is shown by the arrow. The hatched bands show the uncertainty in the background prediction; however, in (b), background uncertainties are not shown for $m_{4\ell} > 115$ GeV. The uncertainties on the data points are asymmetric Poisson errors (Eqs. (40.76a) and (40.76b) 113
6.7 Events selected in signal regions (a) SR1 and (b) SR2, represented in the $(m_{4\ell}, \langle m_{\ell\ell} \rangle)$ plane. The points are differentiated by final state ($4e$, $2e2\mu$, and 4μ) and by data-taking period (2015–2016, 2017, and 2018). 114
6.8 (a) Estimated background and (b) expected signal shape for $(m_S, m_{Z_d}) = (110\text{ GeV}, 30\text{ GeV})$ in SR1 in the $(m_{4\ell}, \langle m_{\ell\ell} \rangle)$ plane, using both histograms and box representations. The signal normalization is arbitrary. 114
6.9 Local p_0-values in the $(m_{4\ell}, \langle m_{\ell\ell} \rangle)$ plane for (a) SR1 and (b) SR2, evaluated in slices in $m_{4\ell}$. The horizontal band in the SR2 figure shows the region excluded by the Z boson veto requirement, $|m_{ab,cd} - m_Z| > 8$ GeV. 115

7.1 (a) represent the Background Rejection versus Signal Efficiency for BDT Classifier, while (b) show the BDT Response Distribution for Signal and Background Samples. 122
7.2 Efficiency of Jet Pairing Methods as a Function of (m_{Z_d}, m_S) Mass Points in $Z_d Z_d \to 2\ell 2j$ Events 123
7.3 Lepton selection efficiency as a function of (m_{Z_d}, m_S) for different identification and p_T thresholds. 124
7.4 Feynman diagram illustrating the signal process: a scalar particle (S) decays into two dark vector bosons (Z_d), with one Z_d decaying leptonically ($\ell\ell$) and the other hadronically (jj). 130
7.5 Scatter plot of simulated mass points in the (m_S, m_{Z_d}) plane, showing the range of scalar and dark vector boson masses probed in the analysis. 132
7.6 Normalized distribution of the mass ratio $m_{\ell\ell}/m_{jj}$ for background processes (Z+jets, W+jets, Top+Diboson) and $S \to Z_d Z_d \to 2\ell 2j$ signal samples with $m_S = 110$ GeV and $m_{Z_d} = 20, 30, 42, 55$ GeV. . . 133
7.7 Three-dimensional distributions of $m_{\ell\ell}$ versus m_{jj} for $S \to Z_d Z_d \to 2\ell 2j$ signal events, for $m_S = 110$ GeV and $m_{Z_d} = 20, 30, 42, 55$ GeV. The prominent peaks demonstrate the strong correlation between the dilepton and dijet masses, both centered around the Z_d mass. 135

7.8 Distribution of the dilepton invariant mass ($m_{\ell\ell}$) versus dijet invariant mass (m_{jj}) for simulated $S \to Z_d Z_d \to 2\ell 2j$ signal samples with $m_S = 110$ GeV and $m_{Z_d} = 20, 30, 42, 55$ GeV. Each panel shows the characteristic clustering of events around the true Z_d mass for different mass hypotheses. 136

List of Tables

6.1 Triggers used in the 2015-2018 analysis. Triggers are only used when they are unprescaled (a separate GRL is maintained for each trigger that records which lumiblocks the trigger was unprescaled for). Prescaled triggers are not included because of their low thresholds (the events that pass only prescaled triggers would not pass our lepton p_T cuts). 92

6.2 Summary of the event selection of SR1 and SR2 for the AS search. . . 96

6.3 Cut flow for the simulated $ZZ^* \to 4\ell$ background with all production modes combined, corresponding to the full 2015–2018 data set, expressed as the number of predicted events and the fraction of events with a same-flavour opposite-sign quadruplet. Yields from each simulation campaign are individually normalized to the corresponding integrated luminosities (2015–2016: 36.2 fb^{-1}; 2017: 44.3 fb^{-1}; 2018: 58.45 fb^{-1}) and then combined (2015–2018: 139 fb^{-1}). Per-channel, the quadruplet cutflow can increase because events can move from one channel to another during the quadruplet selection if a higher-ranked quadruplet fails a cut that a lower-ranked one can pass (however, the cutflow summed across all channels can only decrease). 100

6.4 Cut-flow for the simulated signals with $(m_{Z_d}, m_S) = (20, 50)$ and $(m_{Z_d}, m_S) = (50, 400)$. The represented yields from simulation are for the combined campaigns (2015-18). 101

6.5 Cut-flow efficiency in SR1 and SR2. 101

6.6 Correlation coefficient for the isolation and impact parameter requirements for the channels $4e$, $2e2\mu$, and 4μ, for the 2015–16, 2017 and 2018 data sets. All selections have been applied through the quarkonia vetoes. 105

6.7 Estimation of the $t\bar{t}$ background in HM and AS search for the 2015–16 data (with mc16a MC) and the 2017 data (with mc16d MC), by channel. 106

6.8 Estimation of the Z + jets background in HM and AS search for the 2015–16 data (with mc16a MC) and the 2017 data (with mc16d MC), by channel. 107
6.9 Expected event yields of the SM background processes and observed data in the two signal regions SR1 and SR2. The first uncertainty is the statistical component of the total uncertainty and the second the systematic component. 111

7.1 Baseline object definitions and mass range requirements. 119
7.2 Summary of cuts and signal region selections. 128
7.3 Cutflow for $(m_S, m_{Z_d}) = (110, 50)$ showing the number of events passing each selection criterion for the 2e2j and 2m2j channels, as well as the total. 134

Contents

Dedication i

Acknowledgements ii

Abrégé iv

Abstract v

Résumé détaillé vi

List of publications ix

Contribution x

List of Figures xii

List of Tables xvii

Introduction 1

1 Theoretical Framework 3

1.1 The Standard Model 4

1.1.1 Particles and Forces 4

1.1.2 The Higgs Boson 8

1.1.3 Higgs Boson Discovery. 11

1.1.4 Dark Matter 14

1.2 Beyond The Standard Model 16

1.2.1 Hidden Abelian Higgs Model 16

1.2.2 2HDM + Scalar 18

1.2.3 Additional Scalar Channel(AS) 20

2 Experimental Setup **24**
2.1 The Large Hadron Collider . . . 25
2.2 ATLAS Detector . . . 27
2.2.1 ATLAS Coordinate System . . . 27
2.2.2 Inner Detector . . . 29
2.2.3 Calorimeters . . . 31
2.2.4 Muon Spectrometer . . . 36
2.2.5 Trigger and Data Acquisition System . . . 38
2.3 ATLAS Experiment Phase II Upgrade: . . . 39
2.3.1 The Inner Tracker: . . . 40
2.3.2 The High-Granularity Timing Detector (HGTD): . . . 40

3 Physics Object Reconstruction **44**
3.1 Physics Objects Reconstruction and Identification . . . 45
3.2 Tracks and Vertices . . . 45
3.3 Leptons . . . 46
3.3.1 Electrons Reconstruction . . . 46
3.3.2 Electrons Identification . . . 47
3.3.3 Muons Reconstruction . . . 50
3.3.4 Muons Identification . . . 50
3.4 Jets . . . 51
3.4.1 Jet Reconstruction Algorithms . . . 51
3.4.2 Small-R jets . . . 53
3.4.3 Large-R jets . . . 54
3.4.4 Track-Jets . . . 54
3.5 Missing Transverse Momentum . . . 55
3.5.1 Reconstruction of the Missing Transverse Momentum . . . 56
3.5.2 E_T^{miss} Performance . . . 56
3.6 Overlap Removal . . . 57

4 Jet Energy Scale and Resolution in the High Granularity Timing Detector **60**
4.1 Physics Motivation . . . 61
4.2 High Granularity Timing Detector . . . 62
4.3 Detector Description . . . 63
4.3.1 Detector Design . . . 63

4.3.2 LGAD sensors . . . 65
4.3.3 Front-end Electronics . . . 68
4.4 Physics Prospects . . . 69
4.4.1 Suppression of pileup jets . . . 69
4.4.2 Jet Energy Response and Resolution . . . 71
4.4.3 Jet Energy Response . . . 71
4.4.4 Jet Energy Resolution . . . 72
4.4.5 Jet pT correction . . . 73
4.5 Results . . . 73

5 Thermal Performance Study of the ATLAS ITk Strip Modules at BNL **75**
5.1 Introduction to ITk Strip Modules . . . 76
5.2 ITk Strip Detector: Staves, Petals, and Modules . . . 76
5.2.1 ITk Strip Staves and Petals . . . 76
5.2.2 ITk Strip Modules . . . 78
5.3 Experimental Setup for Thermal Performance Study . . . 80
5.3.1 USB-TC08 Data Logger . . . 81
5.3.2 SHT85 sensor . . . 82
5.3.3 Raspberry Pi4: . . . 84
5.4 Results and Analysis . . . 85

6 Search for Dark Vector Bosons and New Scalars in $Z_dZ_d \to 4\ell$ Final State **89**
6.1 Analysis Strategy . . . 90
6.2 Object and Event selection . . . 90
6.2.1 Event preselection . . . 90
6.2.2 Baseline lepton selection . . . 91
6.2.3 Selection and ranking of quadruplets . . . 91
6.2.4 Event selection . . . 91
6.2.5 Kinematic requirements in event selection . . . 94
6.3 Background simulation . . . 97
6.3.1 Irreducible Backgrounds . . . 97
6.3.2 Reducible Backgrounds . . . 97
6.4 Signal simulation . . . 98
6.5 Background estimation . . . 99

6.5.1 Estimation of irreducible backgrounds . . . 102
6.5.2 Estimation of reducible backgrounds . . . 102
6.6 Systematics uncertainties . . . 105
6.6.1 Experimental systematic uncertainties . . . 105
6.6.2 Theoretical systematic uncertainties . . . 110
6.7 Results . . . 110

7 Search for Dark Vector Bosons and New Scalars in ZdZd→2l2j Final State 116
7.1 Analysis overview . . . 117
7.2 Data and Monte Carlo Samples . . . 118
7.2.1 LHC dataset . . . 118
7.2.2 Monte Carlo Samples . . . 118
7.3 Event selection and reconstruction . . . 118
7.3.1 Event Preselection . . . 119
7.3.2 Truth Study for Jet Selection . . . 119
7.3.3 Leptons Selection . . . 122
7.3.4 Jets Selection . . . 124
7.3.5 Kinematic Variables and Event Selection Framework . . . 125
7.4 Background composition . . . 127
7.4.1 Irreducible Backgrounds . . . 127
7.4.2 Reducible Backgrounds . . . 129
7.5 Signal simulation . . . 129
7.5.1 Production Mechanism . . . 129
7.5.2 Monte Carlo Generation . . . 130
7.5.3 Signal Regions Definition . . . 131
7.6 Background Estimation Strategy . . . 131
7.7 Event yields and Kinematic distributions . . . 132

Conclusions and Future Work 1

Introduction

The Standard Model of particle physics is one of humanity's greatest achievements, as it provides a complete framework that describes the fundamental particles and their interactions through three of the four known forces of nature: the electromagnetic, weak and strong forces. With the discovery of the Higgs boson in 2012 at the Large Hadron Collider (LHC), further refinement of the Standard Model has been achieved, confirming its extraordinary predictive power through decades of experimental validation.

Despite this success, compelling evidence points to the Standard Model remaining incomplete. It fails to explain the gravitational force, it cannot account for the observed dark matter, representing around 27% of the mass-energy balance of our universe, and it is unable to explain the matter-antimatter asymmetry observed in the cosmos. Such fundamental limitations motivate the investigation of physics beyond the Standard Model, with special focus on the mysterious "dark sector" that could harbor new particles and new forces.

This thesis features a detailed study of the potential dark sector physics through the search for dark vector bosons (Z_d) and new scalar particles at the ATLAS experiment. Dark vector bosons emerge from the extensions of the Standard Model that introduce a new U(1) gauge symmetry, notably the Hidden Abelian Higgs Model discussed in chapiter 1. These theoretical frameworks provide strong candidates for mediators between the visible and dark sectors of our universe.

The experimental studies outlined in this thesis exploit the full capabilities of the ATLAS detector at the Large Hadron Collider (LHC), one of the most sophisticated scientific instruments yet constructed. Operating at the energy frontier of particle physics, the LHC provides a unique opportunity to probe physics at the TeV scale, gaining potential access to the phase space where new phenomena might arise. Chapter 2 describes the experimental set-up, highlighting the detection systems essential for the analyses presented.

Two complementary searches for dark vector bosons produced in pairs from the decay of a scalar particle ($S \to Z_d Z_d$) are at the core of this thesis, covering different

final states: the fully leptonic channel ($Z_dZ_d \to 4\ell$) and the semileptonic channel ($Z_dZ_d \to 2\ell 2j$). These analyses, detailed in Chapters 6 and 7, exploit the ATLAS detector's outstanding capabilities to identify and reconstruct electrons, muons and jets with high precision. This search strategy employs innovative advanced reconstruction techniques and event selection criteria, optimized to distinguish potential signals from Standard Model background.

In addition, this work includes contributions to detector performance studies which enhance the capabilities of the ATLAS detector. Chapter 4 covers jet energy scaling and resolution in the high granularity timing detector, while Chapter 5 reports on thermal performance measurements of ITk strip modules at Brookhaven National Laboratory. These technical studies provide support for the ATLAS experiment's physics program, providing a better understanding of the detector and boosting future measurement capabilities.

The analyses presented in this thesis provide a complete search of dark sector physics, covering a wide range of dark vector boson masses from 20 GeV to several hundred GeV. By considering both fully leptonic and semileptonic final states, it achieves an increased sensitivity compared to previous studies, while evolving new analysis techniques that can be applied to future dark sector searches.

With careful experimental design, stringent data analysis and detailed theoretical interpretation, this thesis aims to provide meaningful constraints upon models of dark sector physics, while developing methodologies that will inform the next generation of research at the Large Hadron Collider and beyond.

1

Theoretical Framework

The Standard Model (SM) of particle physics, developed in the 1970s, is a framework describing the fundamental particles and three of the four electromagnetic forces , weak nuclear, and strong nuclear–based on Quantum Field Theory (QFT). The Higgs boson, discovered in 2012, is central to this model, providing mass to particles through the Higgs field. However, the SM leaves many questions unanswered, such as gravity, dark matter, and dark energy, which make up 95% of the universe. It also fails to explain neutrino masses, matter-antimatter asymmetry, and anomalies in particle properties. The discovery of the Higgs boson raises further questions about its uniqueness and stability. These gaps drive physicists to seek theories beyond the SM. This chapter provides an overview of the SM and Beyond Standard Model (BSM) physics, along with a detailed exploration of the Higgs sector and its associated phenomenology. The theoretical framework establishes fundamental principles throughout the Standard Model, with particular emphasis on the role of the Higgs boson in symmetry breaking and mass generation. Experimental observations validate theoretical predictions while revealing the limits of current models. Extensions beyond the Standard Model, including hidden abelian Higgs models and 2HDM + scalar configurations. Studying scalar particles decaying into Z_d boson offers promising insights into hidden sectors.

1.1 The Standard Model

The Standard Model (SM) is a fundamental theoretical framework that appeared in the late 1970s, and has fundamentally changed the understanding of elementary particles and their interactions. It classifies all known elementary particles into two main categories: fermions, the half-integer spin particles that make up matter, and bosons, the integer spin particles that mediate the forces between fermions. The model offers a solid ontological framework to interpret the nature of matter at different scales, and its predictions have been validated by numerous experimental results in particle physics. Four fundamental interactions govern the behavior of matter: the electromagnetic, weak, strong and gravitational forces. Yet the Standard Model successfully describes only three of these interactions at the microscopic level: the electromagnetic force mediated by photons, the weak force mediated by the W and Z bosons, and the strong force mediated by gluons. Interactions within the Standard Model are built around local relativistic quantum field theory (QFT), based on gauge invariance principles represented by the symmetry group $SU(3)_C \otimes SU(2)_L \otimes U(1)_Y$. This framework provides a comprehensive interpretation of phenomena ranging from atomic structures to subnuclear processes through the exchange of bosons between fermions.

1.1.1 Particles and Forces

The SM is a comprehensive classification of the fundamental constituents of the universe and the forces that govern their interactions, as depicted in the figure 1.1. It outlines two essential categories of particles: fermions, which are the building blocks of matter, and bosons, which serve as force carriers facilitating interactions between fermions. Fermions are characterized by their half-integer spin and include quarks and leptons, while bosons possess an integer spin and mediate the fundamental forces.

a. **Fermions:**
Fermions are classified into two main groups: quarks and leptons. Both groups play a crucial role in defining the structure of matter:

- **Quarks:** Quarks represent the fundamental particles combining to create protons, neutrons and other hadrons. Six types of quark exist – up, down, charm, strange, top and bottom – grouped into three generations. All quarks have a fractional electric charge: up quarks (up, charm, top) carry a charge of$-\frac{2}{3}e$, while down quarks (down, strange, bottom) carry a charge of$-\frac{1}{3}e$. Notably, quarks also hold a property known as color charge, crucial to their interactions via the gluon-mediated strong force.

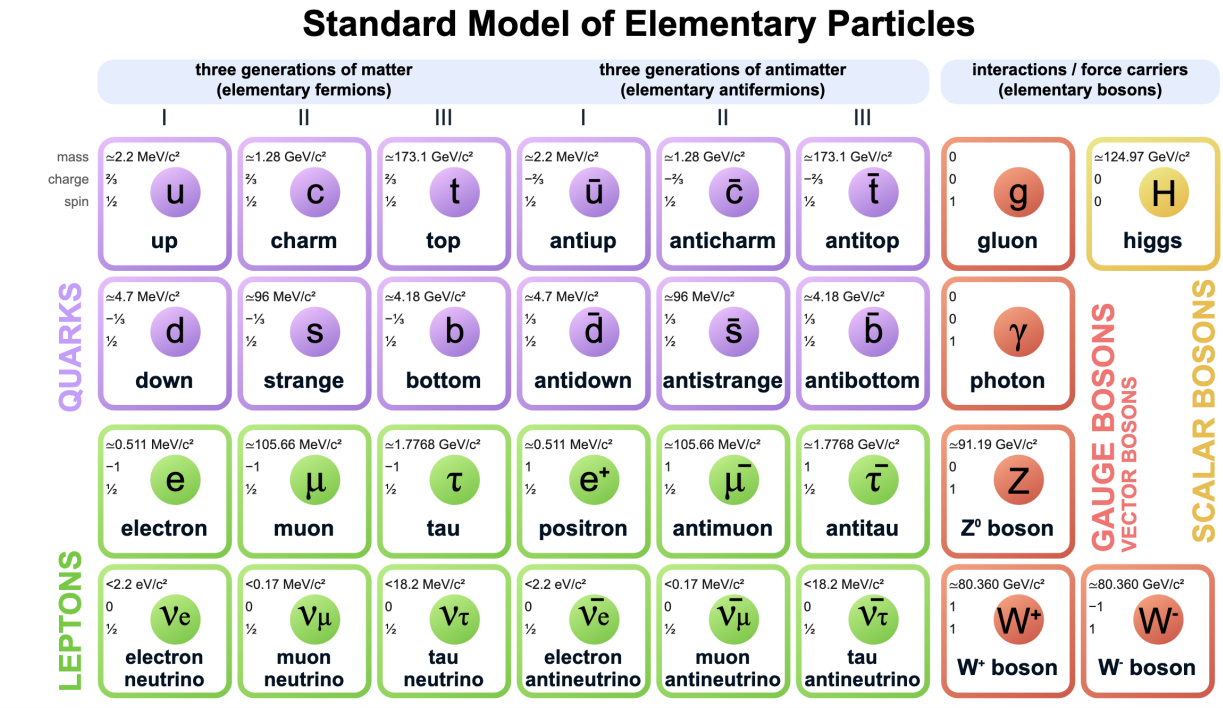


Figure 1.1: Standard Model elementary particles [8].

- **Leptons:** Leptons are another fundamental class of particle that doesn't experience strong interactions. They include three charged leptons: electron (e), muon (μ), tau (τ), and their corresponding neutrinos ($\bar{\nu}$, $\bar{\nu}_\mu$, $\bar{\nu}_\tau$).

b. **Bosons:**
Bosons are the force-carrying particles which mediate the interactions between fermions:

- **Photon:** Photons are vectors of the electromagnetic force. It is massless with light-speed motion, facilitating interactions between charged particles.
- **Gluon:** Gluons mediate the strong force binding quarks within protons and neutrons. They exist in eight different types, each with a different color charge.
- **W & Z Bosons:** These massive gauge bosons mediate weak nuclear

interactions. The W bosons (W^+, W^-) facilitate processes, while the Z boson mediates neutral interactions.

- **Higgs Bosons:** The elementary particle generated by the quantum excitation of the Higgs field that gives mass to some particles.

c. **Interactions**
The Standard Model encompasses three fundamental forces that dictate the behavior of matter:

- **The electromagnetic force:**
Electromagnetic force, mediated by photons, is described by quantum electrodynamics (QED). Acting on all charged particles, such as electrons and quarks, its dynamics are encapsulated in the Lagrangian of quantum electrodynamics. Its density is formulated as follows:

$$\mathcal{L} = \bar{\psi} i\gamma^\mu \partial_\mu \psi - m\bar{\psi}\psi + q\bar{\psi}\gamma^\mu A_\mu \psi - \frac{1}{4} F^{\mu\nu} F_{\mu\nu}$$

where:

  - $\psi(x,t)$ represents the fermion field (e.g., electron), describing the particle's quantum mechanical behavior across spacetime.
  - m is the mass of the fermion, a fundamental property characterizing its inertia.
  - γ^μ are the Dirac matrices, a set of 4x4 matrices satisfying a specific anticommutation relation (the Clifford algebra), essential for representing relativistic spin-1/2 particles.
  - A_μ represents the photon field, the quantum excitation of the electromagnetic field.
  - $F^{\mu\nu} = -F^{\nu\mu} = \partial^\mu A^\nu - \partial^\nu A^\mu$. is the electromagnetic field strength tensor, which describes the dynamics of the electromagnetic field.

The gauge group of this interaction is U(1). To ensure the Lagrangian's invariance under this group, the local phase transformation of the fermion field must satisfy:

$$\psi \to e^{i\alpha(x)}\psi.$$

where $\alpha(x)$ is a space-time dependent phase. The equation illustrates how charged particles interact by exchanging photons. The first two terms describe the kinetic energy and mass of the fermion, while the third term

describes the interaction between the fermion and the photon field. The last term refers to the dynamics of the photon field itself. In the U(1) abelian gauge group, the photons do not self-interact, and the electromagnetic tensor does not include a term for photon self-interactions. That distinguishes QDE from non-Abelian gauge theories such as QCD, where force carriers (gluons) interact with each other.

- **Electroweak Force:**
  The electroweak interaction unifies the electromagnetic and weak forces, and is formulated within the Weinberg–Salam–Glashow model. This theoretical framework relies on the gauge symmetry group $SU(2)_L \times U(1)_Y$, where the $SU(2)_L$ component is associated with weak isospin and acts exclusively on left-handed fermions, while $U(1)_Y$ is linked to weak hypercharge. The mediators of the electroweak force are the photon (γ), the charged W^+ and W^- bosons, and the neutral Z^0 boson. Although the Lagrangian describing this interaction is intricate, it can be separated into distinct elements. One essential element is the covariant derivative, which governs how fermions couple to the gauge bosons. For left-handed fermion doublets, the explicit form of this covariant derivative is: The covariant derivative for left fermion doublets is given by:

$$\mathrm{D}_\mu = \partial_\mu + ig\frac{\tau^i}{2}W_\mu^i + ig'\frac{Y}{2}B_\mu$$

  Where:

  - ∂_μ is the standard four-derivative.
  - g is the coupling constant for the $\mathrm{SU}(2)_L$ gauge group.
  - τ^i are the Pauli matrices, which are the generators of the $\mathrm{SU}(2)_L$ group.
  - W_μ^i are the three gauge bosons associated with the $\mathrm{SU}(2)_L$ group (W^1, W^2, and W^3).
  - g' is the coupling constant for the $\mathrm{U}(1)_Y$ gauge group.
  - Y is the weak hypercharge.
  - B_μ is the gauge boson associated with the $\mathrm{U}(1)_Y$ group.

  After electroweak symmetry breaking, the W^1, W^2, and W^3 bosons mix to form the physical W^+, W^-, and Z^0 bosons, while the B boson mixes with the W^3 boson to form the physical photon (γ) and Z^0 boson.

  The expressions linking the gauge bosons before and after symmetry breaking can be given as follows:

$$A_\mu = B_\mu \cos(\theta_W) + W_\mu^3 \sin(\theta_W) \tag{1.1}$$
$$Z_\mu = W_\mu^3 \cos(\theta_W) - B_\mu \sin(\theta_W) \tag{1.2}$$

Where θ_W is the Weinberg angle (also known as the weak mixing angle), which relates the coupling constants of the electromagnetic and weak interactions.

- **Strong Force:**
  The strong force, mediated by gluons, connects quarks to form hadrons like protons and neutrons. It is described by quantum chromodynamics (QCD).

  Quarks carry color charges (red, green, blue), while gluons also carry colors. Unlike photons in electromagnetism, the interaction between gluons is due to their color charge. As a result, quarks are never observed separately; they must exist within color-neutral hadrons. The QCD Lagrangian includes terms for quark dynamics and gluon interactions:

  $$\mathrm{L_{QCD}} = \sum_f \bar{\psi}_f (i\gamma^\mu D_\mu - m_f)\psi_f - \tfrac{1}{4} G^a_{\mu\nu} G^{a\mu\nu}$$

  Where: $D_\mu = \partial_\mu + i g_s T^a G^a_\mu$ is the covariant derivative with g_s being the strong coupling constant.

  This formulation highlights how QCD differs from QED due to gluon self-interactions.

1.1.2 The Higgs Boson

The last missing piece of the SM concerns the basic question of mass generation, resolved by the Brout-Englert-Higgs (BEH) mechanism. This mechanism, proposed in 1964 by three groups of theorists (Brout & Englert; Higgs; Guralnik, Hagen & Kibble), involves spontaneous symmetry breaking in the electroweak sector, where a scalar Higgs field acquires a non-zero vacuum expectation value, enabling particles to acquire mass through interactions with this field[9, 10]. At the Large Hadron Collider (LHC), Higgs bosons are produced by various processes and decay into different pairs of particles, providing a unique window into the mass-generating dynamics of the BEH mechanism. The production and decay modes are directly influenced by other particles of the SM, which is proportional to their mass.

a. **Higgs Boson Production Mode**

At the Large Hadron Collider (LHC) with proton–proton collisions in the energy range 7–13 TeV, several distinct mechanisms contribute to Higgs boson production. Diagrams for these processes are shown in Figure 1.2 and their corresponding cross sections in Figure 1.3 In order of decreasing production cross section, they are:

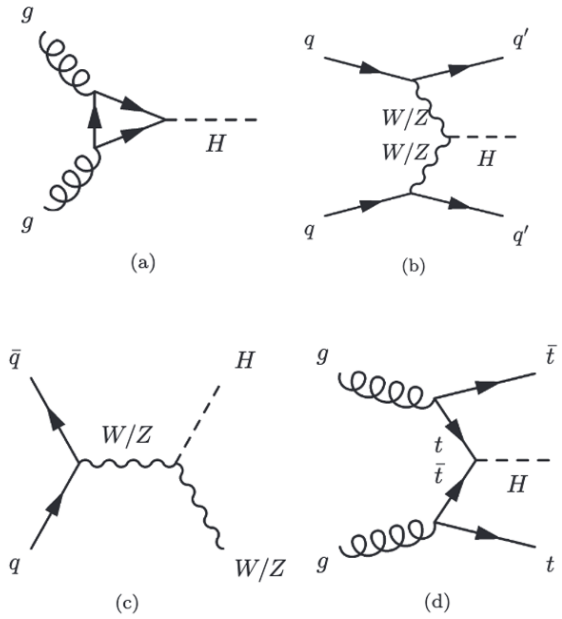


Figure 1.2: Feynman diagrams for the main Higgs boson production modes.

Gluon–gluon fusion (ggF, Figure 1.2a) is the main production process at the LHC. It occurs as two gluons merge through a heavy quark loop, mainly involving the top quark, to generate a Higgs boson.

Vector-boson fusion (VBF, Figure 1.2b) is the second most important mechanism. In this process, two quarks each emit a W or Z boson, which then interact to form a Higgs boson.

The VBF process can be distinguished by the presence of two energetic jets in the forward regions, separated by a wide pseudorapidity gap where particle activity is considerably reduced. Although the VBF cross-section is ten times smaller than that of the ggF process for the observed Higgs boson mass, theoretical calculations indicate that it would approach the

ggF magnitude for a hypothetical Higgs boson mass of 1 TeV.

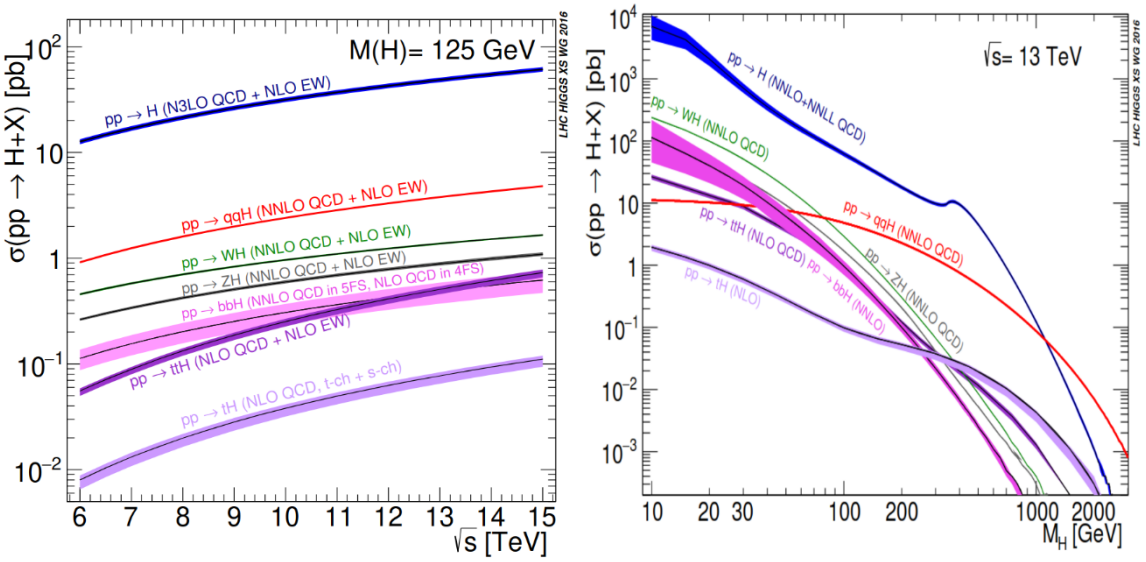
The third mechanism is associated vector boson production (VH), also referred as Higgs-strahlung, involving the emission of a Higgs boson from a $W^{\pm}$ or Z^0 boson, Figure 1.2(c).The VH process has a cross section comparable to that of the VBF process at the observed Higgs mass, although significantly less at higher masses as shown in Figure 1.3(b).

Finally, a Higgs boson can be produced in association with a pair of top quarks, as shown in Figure 1.2(d). This process is particularly interesting, as it allows direct measurement of the coupling between the Higgs boson and the top quark. The related bbH process has a similar cross section.

The Standard Model Higgs boson's production cross section varies with its mass and the collision center-of-mass energy, as shown in Figure 1.3. Since the Higgs boson is an unstable particle, its decay is quantified by the decay width Γ, which is inversely related to its lifetime τ by the relation $\Gamma\tau = \hbar$, where $\hbar$ represents the reduced Planck constant. For a Higgs boson of mass $m_H = 125$ GeV, the decay width is around 4 MeV [11]. To detect and study the Higgs boson and its various production mechanisms, scientists reconstruct it using the decay products in the decay channels selected.

b. **Higgs Boson Decays**

The Higgs boson has several distinct decay channels that depend on the Higgs boson's mass, as shown in Figure 1.4. Interesting decay modes include two-photon decay ($H \to \gamma\gamma$), which, although has a relatively low branching ratio of 0.23%, provides a clear experimental signature; two-Z boson decay ($H \to ZZ^*$), which can then decay into four leptons; and two-W boson decay ($H \to WW^*$). The $H \to WW^*$ and $H \to ZZ^*$ modes would have dominated the decay, if the Higgs boson were sufficiently heavy to decay into two real vector bosons, with a small contribution from the Higgs boson to a top-antitop quark pair. The dominant decay channel for the 125 GeV Higgs boson is in an actual lower quark-antiquark pair ($H \to b\bar{b}$), accounting for around 58% of all decays. The $H \to \gamma\gamma$ decay occurs via a loop processes, as shown in Figure 1.7. In particular, the total decay width of the Higgs boson varies considerably with its mass, ranging from around 10^{-3} GeV for the lowest masses to nearly 1000 GeV for the highest masses.



(a) (b)

Figure 1.3: (a) Cross-sections for different Higgs boson production modes at a proton-proton collider with a centre-of-mass energy of 6–15 TeV. (b) A Higgs boson mass of 125 GeV is assumed in this plot. cross-sections as a function of Higgs boson mass are shown [12].

1.1.3 Higgs Boson Discovery.

The discovery of the Higgs boson in 2012 at CERN's Large Hadron Collider (LHC) represented a milestone in particle physics, confirming an essential aspect of the Standard Model: the Higgs mechanism. This mechanism describes how fundamental particles gain mass through interactions with the Higgs field. Since its discovery, research has focused on understanding its properties and interactions. Solid evidence of the behavior predicted by the Standard Model has been observed between the Higgs boson and the W/Z bosons. These observations include lower-quark decays with high statistical levels. ATLAS and CMS collaborations have provided direct measurements of the Higgs boson decay into four leptons ($H \rightarrow ZZ^* \rightarrow 4l$) [14], with clear signal peaks around 125 GeV, demonstrating the Higgs boson's existence and the determination of its mass through these decay channels. These measurements are exemplified in Figure 1.6 (a) and (b), which illustrate the invariant mass distribution of four-lepton events from the ATLAS and CMS experiments, respectively, with

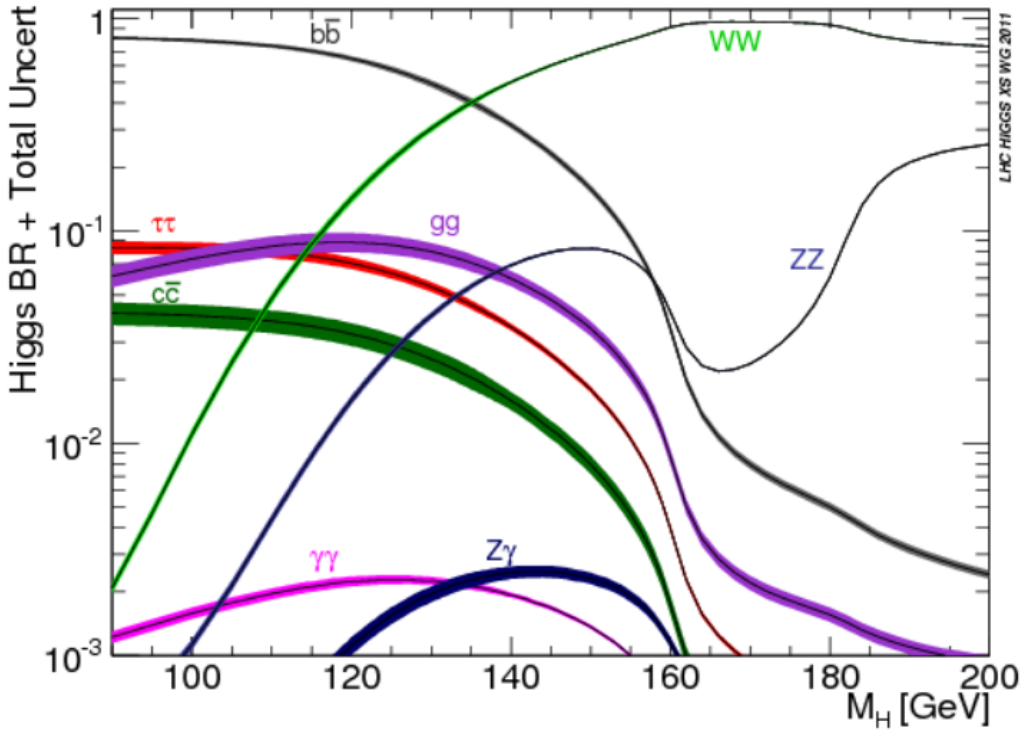


Figure 1.4: Higgs boson branching ratio of the possible Higgs boson decay channels as a function of the Higgs boson mass [13].

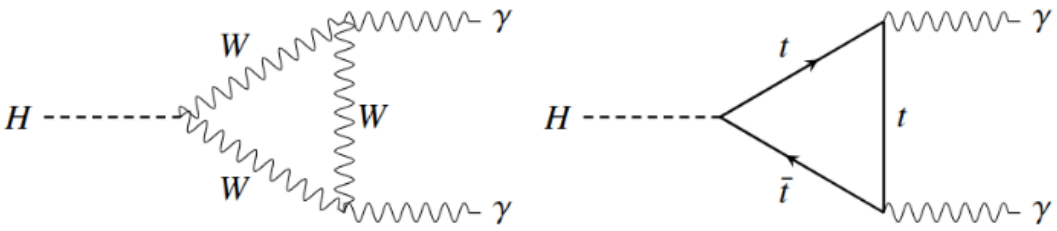


Figure 1.5: Feynman diagrams for $H \to \gamma\gamma$ decay

distinct peaks around the expected mass of the Higgs boson. Specifically, as shown in Figure 1.6 (a), the ATLAS experiment at $\sqrt{s} = 7$ TeV (integrated luminosity of 4.8 fb^{-1}) and 8 TeV (integrated luminosity of 5.8 fb^{-1}) shows a clear signal (blue) above the background (red and purple) around the mass

of 125 GeV in the m_{4l} distribution. Similarly, Figure 1.6 (b) from the CMS experiment at $\sqrt{s} = 7\ TeV$ (integrated luminosity of 5.1 fb^{-1}) and 8 TeV (integrated luminosity of 5.3 fb^{-1}) shows a signal peak in the four-lepton invariant mass distribution around 125 GeV.

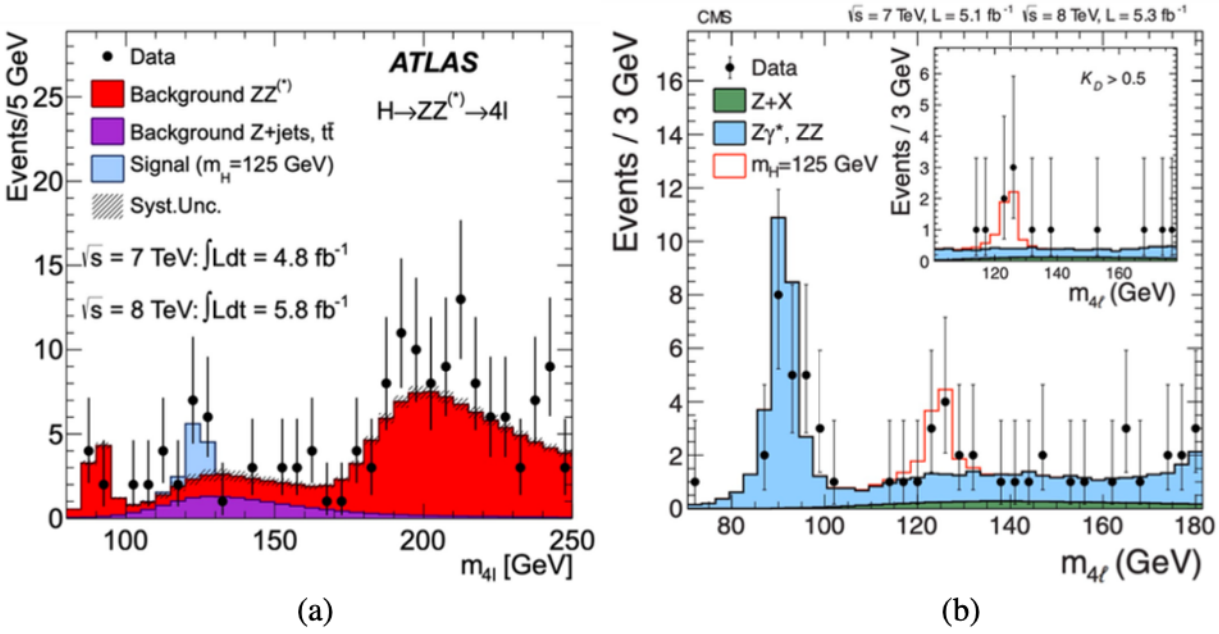


Figure 1.6: The distribution of the four-lepton invariant mass, m4l, for the selected candidates, compared to the background expectation in the 80-250GeV mass range, $\sqrt{s} = 7$ TeV $\sqrt{s} = 8$ TeV data in both ATLAS (a) [15] and CMS (b) [16] detectors, the signal expectation for a SM Higgs with $m_H = 125GeV$ is also shown.

State-of-the-art results on the Higgs boson have been achieved by investigating three channels, including precision measurements, searches for rare decays and measurements of differential cross sections. The studies not only confirm the predictions of the Standard Model, but also open the possibility of discovering new physics beyond the Standard Model. However, while the Standard Model has been highly effective in providing explanations for the particles and forces known, it fails to account for all observed phenomena. One of the greatest mysteries is dark matter, a non-luminous substance that makes up a substantial fraction of our universe's mass and energy density. Which brings us to the next major boundary in particle physics: the nature and properties of dark matter.

1.1.4 Dark Matter

Current research into dark matter is providing a better understanding of how this elusive form of matter provides the structure and development of the universe. Constituting up to 27% of the mass and energy density of the universe, dark matter is only visible through its gravitational influence. At CERN's Large Hadron Collider (LHC), the ATLAS experiment is at the forefront of the search for dark matter.

a. **Detection Methods:**
   ATLAS uses a multi-faceted approach in its investigation of dark matter, which can be summarized visually in figure 1.7:

   - **Direct and Indirect Detection Methods:**
     These methods are designed to capture dark matter particles through their interactions with Standard Model (SM) particles. Figure 1.7 (a) illustrates indirect detection (ID), where dark matter (DM) particles annihilate or decay into Standard Model particles, giving rise to detectable particles that we can observe using our detectors. Figure 1.7 (b) illustrates direct detection (DD), where dark matter particles scatter on dense matter particles, resulting in a detectable recoil.
   - **Collider Searches:**
     Besides traditional approaches, the LHC is used to produce dark matter directly. Figure 1.7 (c) illustrates dark matter searches in colliders, where SM particles collide and produce dark matter particles at the same time as other SM particles. These events are characterized by missing energy and momentum, a signature indicative of dark matter production.

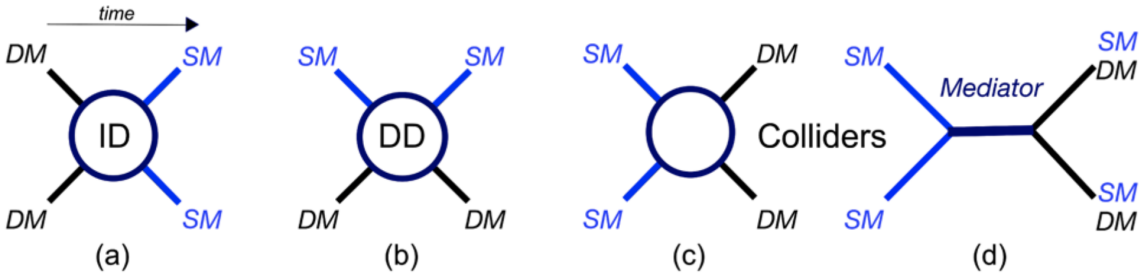


Figure 1.7: Possible dark matter detection methods.

b. **Mediator Searches:**
In addition, the search for new mediator particles that could interact with dark matter particles is also underway. These mediators are hypothetical particles that would mediate interactions between dark matter and magnetic matter particles, which could lead to observable signatures in our detectors. This approach is illustrated in figure 1.7 (d), which depicts a mediator particle linking dark matter and magnetic matter particles.

d. **Candidate Particles:**

Various particles are considered to be potential candidates for dark matter:

- **Weakly Interacting Massve Particles**: They interact via the weak nuclear forces and are stable on cosmic timescales. WIMPs are popular candidates due to their potential to explain observed dark matter phenomena [17, 18, 19].
- **Supersymmetric Particles** : Supersymmetry proposes novel particles which could be candidates for dark matter. ATLAS has conducted extensive research into these particles, placing strict constraints on their masses and interactions [20].
- **Axions**:Very low-mass hypothetical particles, axions, could also contribute to dark matter. However, they are more difficult to detect directly [21].

e. **Future Directions:**

Future research at ATLAS will continue to develop detection methods and explore new models:

- **Hight-Luminosity LHC (HL-LHC)**:The upgrades improve sensitivity by increasing brightness, allowing more precise searches and potentially revealing new forms of physics beyond the Standard Model.
- **Combined Analyses** :ATLAS will continue combining different investigation channels in order to enhance the constraints on dark matter models, thereby increasing sensitivity to new physics.

Ongoing research into dark matter and other invisible particles reveals the limitations of the Standard Model as a complete explanation of all observed phenomena. Although the Standard Model has been remarkably effective in describing the particles and forces we know, it fails to consider dark matter or dark energy, which together account for around 95% of the mass and energy density of the universe.

This observation is prompting physicists to explore theories beyond the Standard Model.

1.2 Beyond The Standard Model

As the standard model cannot fully explain the mysteries of the universe, researchers have been looking to various extensions that offer new perspectives. Especially the promising models that modify or extend the scalar sector of the Standard Model. The hidden Abelian Higgs model, for example, introduces additional scalar fields that could interact with dark matter particles or provide new channels for particle production. Similarly, the two-dragon-doublet (2HDM) + scalar model [22] offers a potential framework to understand new scalar interactions. In addition, the additional scalar channels (AS) provide a wider context for exploring new physics beyond the Standard Model. These models offer not only potential explanations for dark matter, but also testable predictions that can be explored experimentally.

1.2.1 Hidden Abelian Higgs Model

The Hidden Abelian Higgs Model (HAHM) is an extension of the Standard Model (SM) by expanding its gauge group $G = SU(3)_C \otimes SU(2)_L \otimes U(1)_Y$ with an additional $U(1)_d$ symmetry, resulting in $G' = SU(3)_C \otimes SU(2)_L \otimes U(1)_Y \otimes U(1)_d$. This extension is mediated via a relatively light vector boson, known as the dark Z boson (Z_d), acting as a portal between the SM and the hidden sectors. A prediction of this model is the decay channel of the Higgs boson SM (H) into two light Z_d bosons: $H \to Z_d Z_d$, where the mass of Z_d is limited to the interval $m_{Z_d} \in [\sim \text{MeV}, 60\ \text{GeV}]$. The interaction between the SM and the hidden sector manifests as kinetic mixing, described by the Lagrangian gauge interaction [23]:

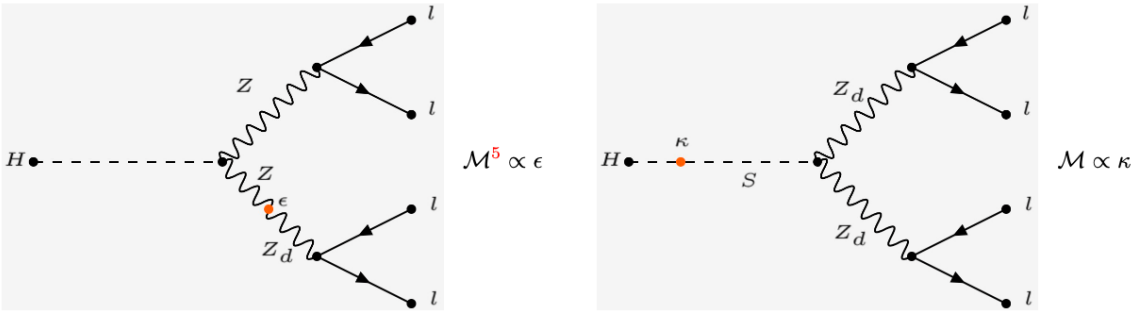
$$\mathcal{L}_{\text{gauge}} = -\frac{1}{4} B_{\mu\nu} B^{\mu\nu} + \frac{1}{2} \frac{\epsilon}{\cos\theta_W} B_{\mu\nu} Z_d^{\mu\nu} - \frac{1}{4} Z_{d\mu\nu} Z_d^{\mu\nu}, \tag{1.3}$$

where $B_{\mu\nu} = \partial_\mu B_\nu - \partial_\nu B_\mu$ represents the $U(1)_Y$ field tensor, $Z^d_{\mu\nu} = \partial_\mu Z^d_\nu - \partial_\nu Z^d_\mu$ is the $U(1)_d$ field tensor, and ε is the kinetic mixing parameter bounded by $\varepsilon \in [10^{-17}, 10^{-2}]$. The Weinberg mixing angle θ_W appears as a fundamental parameter in the mixing term, and the entire interaction is gauge invariant under the two symmetries $U(1)$.

An additional coupling mechanism allows the Standard Model to interface with the hidden sector: the Higgs mixing interaction. This coupling is expressed mathematically by the Higgs potential V_0:

$$V_0 = -\mu^2 |H|^2 + \lambda |H|^4 - \mu_d^2 |S|^2 + \lambda_d |S|^4 + \kappa |H|^2 |S|^2. \tag{2.21}$$

κ in this formulation represents the Higgs mixing parameter, which governs the interaction strength between the dark Higgs boson (S) and the Standard Model Higgs boson (H).
As illustrated in Figure 1.8, two distinct mechanisms facilitate the interaction between the Standard Model and the dark sector: The hypercharge portal, parameterized by ε, which enables $H \to Z_{Zd}$ decay processes (figure 1.8a), or through Higgs-portal coupling $H \to Z_d Z_d$ and $S \to Z_d Z_d$ (figure 1.8b) mediated by κ.



(a) Hypercharge portal

(b) Higgs portal

Figure 1.8: Four-lepton decay modes of the Higgs boson through Z and dark Z intermediaries, demonstrating hypercharge and Higgs portal couplings.

Dark Z boson (Z_d) interactions are characterized by two distinct mixing scenarios that drive its decay mechanisms. A viable phenomenology requires Z_d to have a mass greater than 10 MeV [22] in order to guarantee rapid decay. as illustrated in Figure 1.9 In the regime dominated by kinetic mixing ($\varepsilon \gg \kappa$), the main decay channel is the $H \to Z Z_d$, with a partial width of:

$$\Gamma(H \to Z Z_d) = \frac{\varepsilon^2 \tan^2 \theta_W m_Z^2 (m_H^2 - m_Z^2)^3}{16\pi m_H^3 m_Z^2 v^2} \tag{1.4}$$

where $v \approx 246$ GeV stands for the vacuum expectation value of the Higgs SM. Notably, while $H \to Z_d Z_d$ decay is possible by kinetic mixing, it incurs significant suppression ($\propto \varepsilon^4$) due to the requirement of double Z-Z_d mixing. Reversely, in the regime dominated by Higgs mixing ($\kappa \gg \varepsilon$), $H \to Z_d Z_d$ decay becomes significant, with a partial width of [24]:

$$\Gamma(H \to Z_d Z_d) = \frac{\kappa^2 v^2}{32\pi m_H} \sqrt{1 - \frac{4m_{Z_d}^2}{m_H^2}} \frac{(m_H^2 + 2m_{Z_d}^2)^2 - 8(m_H^2 - m_{Z_d}^2)m_{Z_d}^2}{m_H^4}, \tag{1.5}$$

where $\kappa' = \kappa \frac{m_H^2}{|m_H^2 - m_S^2|}$ considers dark and standard Higgs masses.
The Standard Model interaction between Zd and fermions follows:

$$\mathcal{L}_{Z_d ff} = g_{Z_d ff} \bar{f} \gamma^\mu Z_{d,\mu} f \tag{1.6}$$

where the coupling constant $g_{Z_d ff}$ is :

$$g_{Z_d f\bar{f}} = \frac{g}{\cos\theta_W} \left(-\sin\alpha \left(t^3 \cos^2\theta_W - Y \sin^2\theta_W \right) + \eta \cos\alpha \sin\theta_W Y \right) \tag{1.7}$$

given a decay width in fermion pairs of:

$$\Gamma(Z_d \to f\bar{f}) = \frac{N_c}{24\pi m_{Z_d}} \sqrt{1 - \frac{4m_f^2}{m_{Z_d}^2}} \left[m_{Z_d}^2 (g_L^2 + g_R^2) - m_f^2 (-6 g_L g_R + g_L^2 + g_R^2) \right] \tag{1.8}$$

where N_c equals 1 for leptons and 3 for quarks, demonstrating how the dark Z boson interacts with known particles via these distinct mechanisms.

1.2.2 2HDM + Scalar

The Two Higgs Doublet Model plus scalar (2HDM+S) represents a significant extension of the Standard Model, characterized by two SU(2)L scalar doublets i (i = 1,2) with hypercharge Y = 1/2, defined by:

$$\Phi_i = \phi_i^+ \frac{(v_i + \phi_i^0 + iG_i^0)}{\sqrt{2}} \tag{1.9}$$

Where the vacuum expectation values follow $v = \sqrt{v_1^2 + v_2^2} = 246$ GeV. The model's potential is governed by:

$$\begin{aligned} V(\Phi_1, \Phi_2) = {} & m_{11}^2 \Phi_1^\dagger \Phi_1 + m_{22}^2 \Phi_2^\dagger \Phi_2 - m_{12}^2 (\Phi_1^\dagger \Phi_2 + \Phi_2^\dagger \Phi_1) + \frac{\lambda_1}{2} (\Phi_1^\dagger \Phi_1)^2 + \\ & \frac{\lambda_2}{2} (\Phi_2^\dagger \Phi_2)^2 + \lambda_3 \Phi_1^\dagger \Phi_1 \Phi_2^\dagger \Phi_2 + \lambda_4 \Phi_1^\dagger \Phi_2 \Phi_2^\dagger \Phi_1 + \frac{\lambda_5}{2} \left[(\Phi_1^\dagger \Phi_2)^2 + (\Phi_2^\dagger \Phi_1)^2 \right] \end{aligned} \tag{1.10}$$

featuring four distinct types of Yukawa couplings along with unique branching ratio characteristics:

- Type I: All fermions couple exclusively to one Higgs doublet, Φ_2 (by convention).
- Type II:

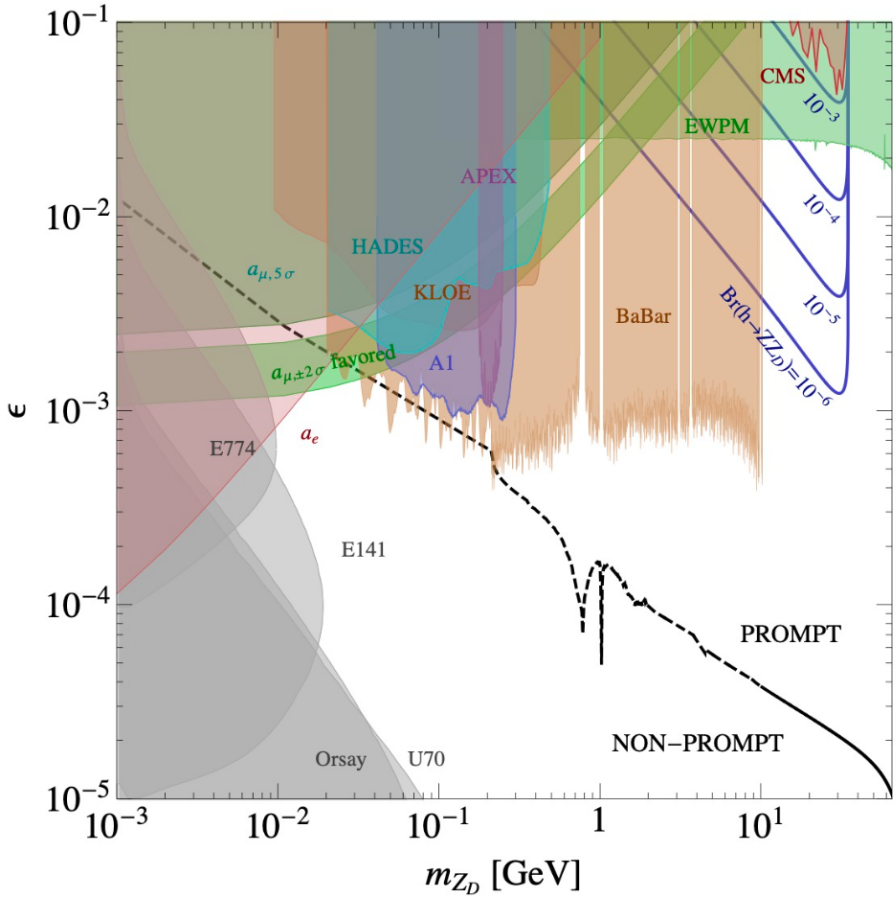


Figure 1.9: Constraints on ε for pure kinetic mixing for $m_{Z_d} \sim$ MeV $-$ 60 GeV. The black dashed line separates prompt ($c\tau < 1\mu$m) from non-prompt Z_d decays. The three blue lines are contours of Br($H \to ZZ_d$) of 10^{-4}, 10^{-5}, 10^{-6} respectively [22].

  - $Q = \frac{2}{3}$ right-handed (RH) quarks couple to Φ_2
  - $Q = -\frac{1}{3}$ RH quarks and RH leptons couple to Φ_1
- Type III (Lepton-specific):
  - All RH quarks couple to Φ_2
  - RH leptons couple to Φ_1
- Type IV (Flipped):
  - $Q = \frac{2}{3}$ RH quarks couple to Φ_2

- $Q = -\frac{1}{3}$ RH quarks couple to Φ_1
- RH leptons couple to Φ_2

The Two Higgs Doublet Model (2HDM) [25, 26] presents a rich phenomenology of exotic Higgs decays, where the observed Higgs particle (H or H^0) at 125 GeV can decay through several unique channels: $H \to AA$, $H^0 \to HH$, AA, or $H \to ZA$. These exotic particles subsequently cascade into Standard Model fermions or gauge bosons, creating distinctive experimental signatures. While experimental data have placed significant constraints on this phenomenology, certain regions in the parameter space remain unexplored. To accommodate these experimental constraints, the 2HDM is typically considered in the decoupling limit, defined by:

$$\alpha \to \beta - \pi/2 \tag{1.11}$$

where β is a rotation angle characterized by $\tan\beta = v_2/v_1$, with $v_{1,2}$ representing the vacuum expectation values of the two Higgs doublets $H_{1,2}$. In this decoupling regime, the observed 125 GeV state (H) emerges as the lightest state, with its fermion couplings becoming identical to those of the Standard Model Higgs. Notably, when $\tan\beta$ is greater than or equal to 5, the gauge boson couplings closely approximate Standard Model-like behavior. The specific properties of H and the nature of fermion couplings are intricately determined by both $\tan\beta$ and α, with the Higgs spectrum and phenomenology parameters being heavily constrained by measured production and decay rates of H. An alternative approach to navigating these constraints involves extending the 2HDM by adding a complex scalar singlet, defined as:

$$S = \frac{1}{\sqrt{2}}(S_R + iS_I) \tag{1.12}$$

This extension, known as 2HDM+S, introduces a singlet that can acquire its own vacuum expectation value. Unlike the original Higgs doublets, this singlet couples exclusively to $H_{1,2}$ in the potential without direct Yukawa couplings, instead interacting with Standard Model fermions through its mixing with $H_{1,2}$. To maintain the observed Standard Model-like nature of H, this mixing must remain small, providing a natural mechanism for preserving the successful predictions of the Standard Model while allowing for potential new physics in the scalar sector.

1.2.3 Additional Scalar Channel(AS)

The study explores an extended model of the dark sector consisting of a dark scalar (S) decaying into leptons and jets via dark Z bosons ($S \to Z_d Z_d \to 4\ell$ and $S \to Z_d Z_d \to 2\ell 2j$), where S differs in mass from the SM Higgs boson discovered at 125

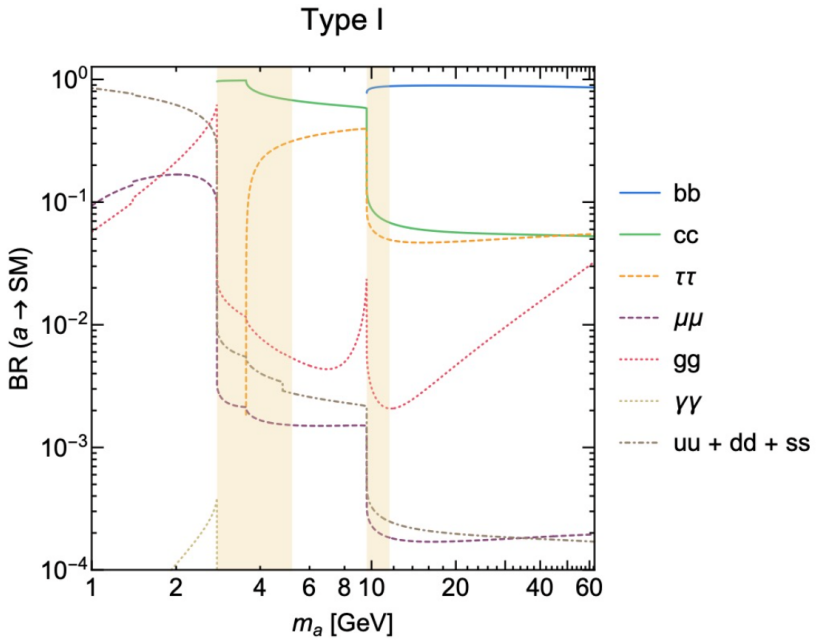


Figure 1.10: Branching Ratios ($a \to f\bar{f}$) in 2HDM+S Model Type I. Decays to quarkonia likely invalidate our simple calculations in the shade regions [22].

GeV.

The dark Higgs field is introduced to break dark U(1) gauge symmetry spontaneously, mixing with SM (H) Higgs through a κ Higgs gate mixing parameter. This mixing allows all Higgs SM-producing processes to also produce the dark Higgs, with gluon fusion being the dominant mechanism. The search covers a range of dark scalar masses from [30,800] GeV, with dark boson masses between 15 and 250 GeV resulting in $4e$, 4μ, or $2e2\mu$ final states for $S \to Z_d Z_d \to 4\ell$. For $S \to Z_d Z_d \to 2\ell 2j$ a range of dark scalar masses from [70,110] GeV, with dark boson masses between 20 and 55 GeV resulting in $2e$, 2μ. The lower mass limit of 15 GeV for Z_d is necessary because lighter dark bosons would produce strongly boosted leptons that would not meet the isolation requirements. For heavier Z_d scenarios, in order to maintain the observable $Z_d \to \ell\ell$ decay mode and prevent decays into invisible dark sector states, it must be expected that Z_d is the lightest dark sector state. The ε parameter continues to be crucial to ensure the decay of dark bosons into SM fermions. This search channel, although implicit in previous studies, opens up new possibilities for the search for dark matter through the dark Higgs portal, although it requires careful consideration of any constraints from both LEP data ($e^+e^- \to \ell^+\ell^-$) and potential

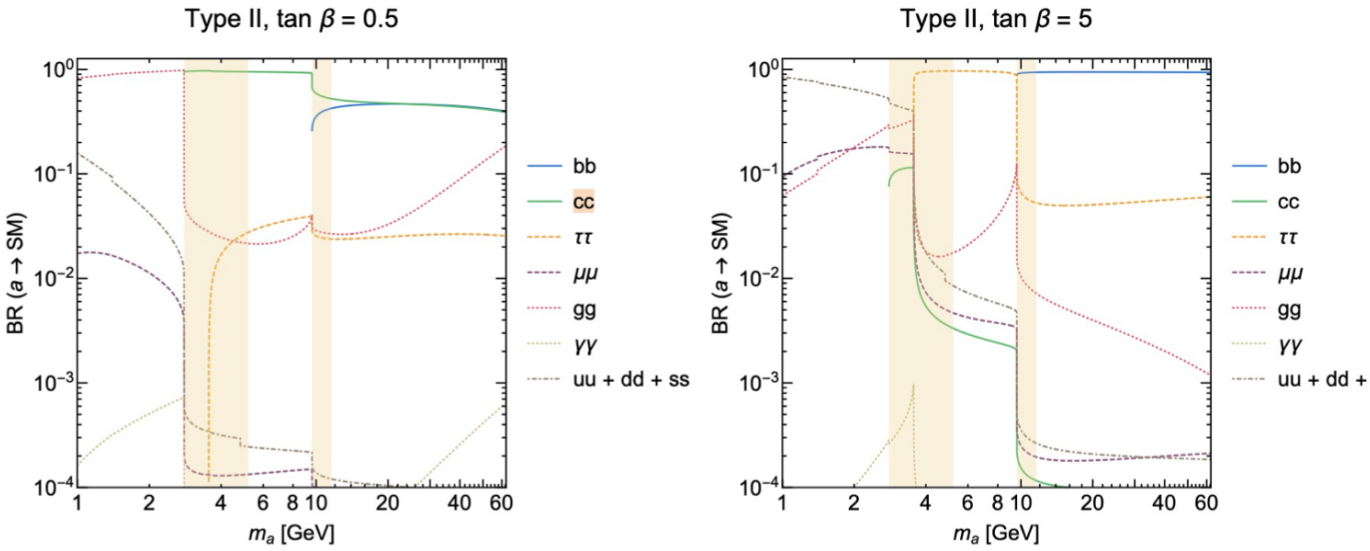


Figure 1.11: Branching Ratios ($a \to f\bar{f}$) in 2HDM+S Model Type II . Decays to quarkonia likely invalidate our simple calculations in the shade regions [22].

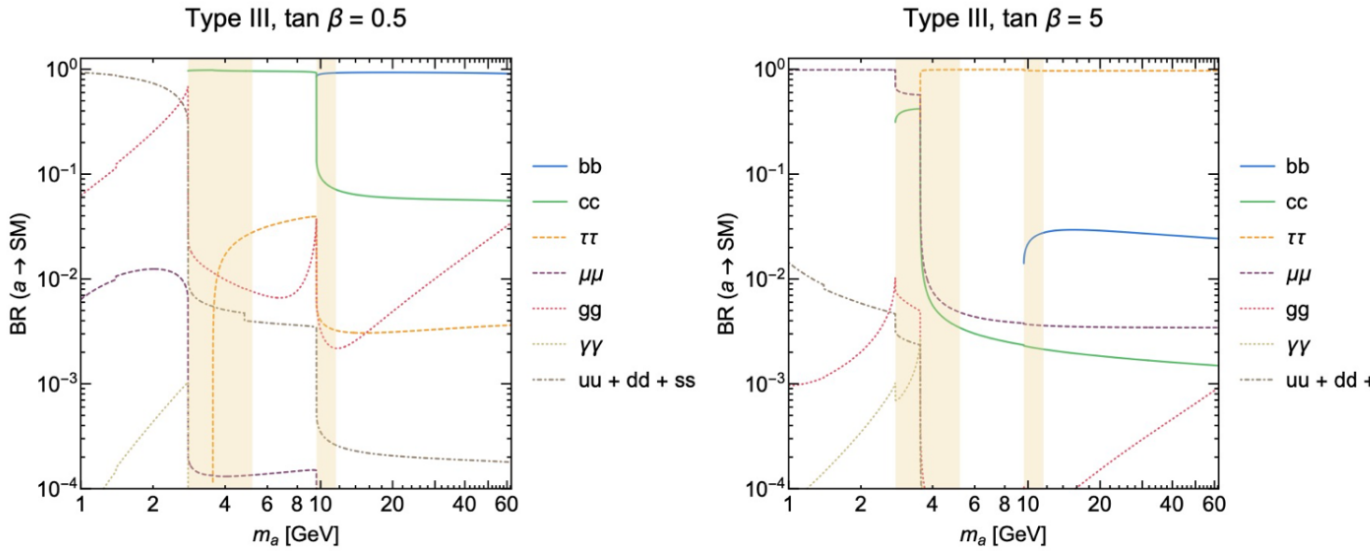


Figure 1.12: Branching Ratios ($a \to f\bar{f}$) in 2HDM+S Model Type III . Decays to quarkonia likely invalidate our simple calculations in the shade regions [22].

Drell-Yan processes ($pp \to Z_d \to \ell^+\ell^-$).

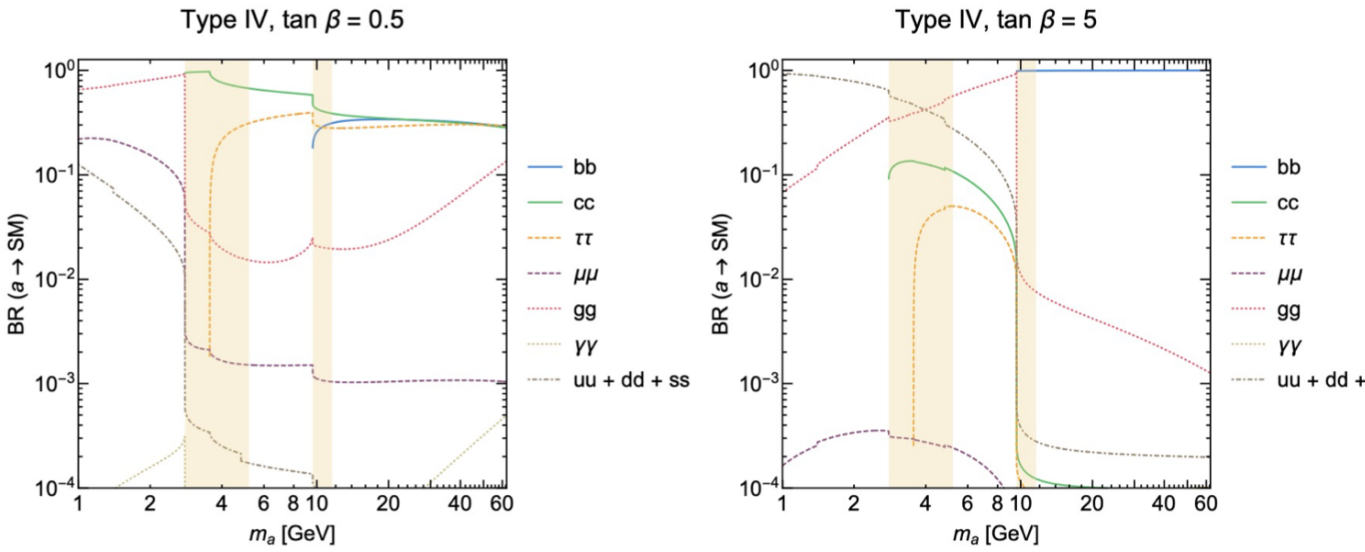


Figure 1.13: Pseudoscalar Branching Ratios ($a \to f\bar{f}$) in 2HDM+S Model Type IV. Decays to quarkonia likely invalidate our simple calculations in the shade regions [22].

2

Experimental Setup

Understanding the experimental framework is essential for interpreting the physics analysis presented in this dissertation. This analysis exploits a dataset of 140 fb^{1} of proton-proton collision events at a center-of-mass energy of 13 TeV, recorded by the ATLAS experiment during LHC Run 2 (2015–2018). At the heart of this study lies the Large Hadron Collider (LHC), the most powerful particle accelerator ever built. It is the only facility capable of colliding protons at s = 14 TeV and heavy ions at s = 5.6 TeV, making it an unparalleled tool for high-energy physics research. The ATLAS experiment, one of the four major detectors at the LHC, is a general-purpose detector designed to capture and analyze the complex interactions resulting from these high-energy collisions. Its intricate system of sub-detectors is engineered to identify and measure different types of particles with high precision. This chapter is structured as follows: Section 3.1 provides an overview of the LHC and its operation. Section 3.2 delves into the technical design of the ATLAS detector and its sub-systems. Section 3.3 offers a brief look at the Phase II upgrade, which will enhance ATLAS's capabilities for future runs. Through this discussion, we establish the foundation necessary to understand the experimental conditions and data acquisition process underpinning the subsequent analysis.

2.1 The Large Hadron Collider

Deep beneath the Swiss-French border, near Geneva, lies one of humanity's greatest scientific achievements, the Large Hadron Collider (LHC) [27]. This 27-kilometer underground ring, installed and operated by the European Organisation for Nuclear research (CERN), is the most powerful particle accelerator ever built. Here, scientists push the boundaries of knowledge by smashing protons together at nearly the speed of light, recreating conditions that existed just moments after the Big Bang. The LHC's journey began in 2010 with its first run. At that time, it was operating at 7 and 8 TeV, an energy level high enough to make history. And it did. In 2012, two of its massive detectors, ATLAS [28] and CMS [29], made a groundbreaking discovery, the Higgs boson, the missing piece in our understanding of how particles gain mass. This discovery was so essential that it earned a Nobel Prize soon after. But the LHC was just getting started. After a two-year pause, known as Long Shutdown 1, it returned in 2015 with even greater power. Now running at 13 TeV, it began a new era of discoveries. Scientists observed the Higgs boson decaying into bottom quarks [30, 31], confirming another key prediction of particle physics. They also witnessed the rare four-top-quark production [32, 33], an event so elusive that detecting it was a triumph of precision and technology. Today, the LHC is in the middle of its third run, which began in 2022 and will continue until 2026. The energy has been pushed even higher to 13.6 TeV, and researchers are expecting an enormous amount of data, enough to reveal phenomena never seen before. But how does this incredible machine work? At its core, the LHC is a symphony of engineering and physics. Two beams of protons race in opposite directions inside a vacuum tube, guided by powerful magnetic fields. These fields, created by over 1,200 superconducting magnets, are strong enough to bend the paths of the speeding protons, keeping them on track. However, to function properly, these magnets must be kept at -271°C, colder than outer space. This is achieved by a sophisticated cooling system that uses liquid helium. Before the protons even reach the LHC, they take a long journey through a series of smaller accelerators. This injector system gradually boosts their energy step by step, ensuring they are moving fast enough for the final collision. Once inside the LHC, the protons continue accelerating until they reach their maximum speed. Then, at four key points along the ring, they are smashed together, releasing a burst of energy that scientists capture using giant detectors. Each of these four detectors has a unique role. ATLAS [35], and CMS [36], act as the all-seeing eyes of the experiment, searching for new particles and unexpected phenomena. LHCb [37], specializes in studying subtle differences between matter and antimatter, hoping to solve the mystery of why our universe exists. Meanwhile, ALICE [38], focuses on

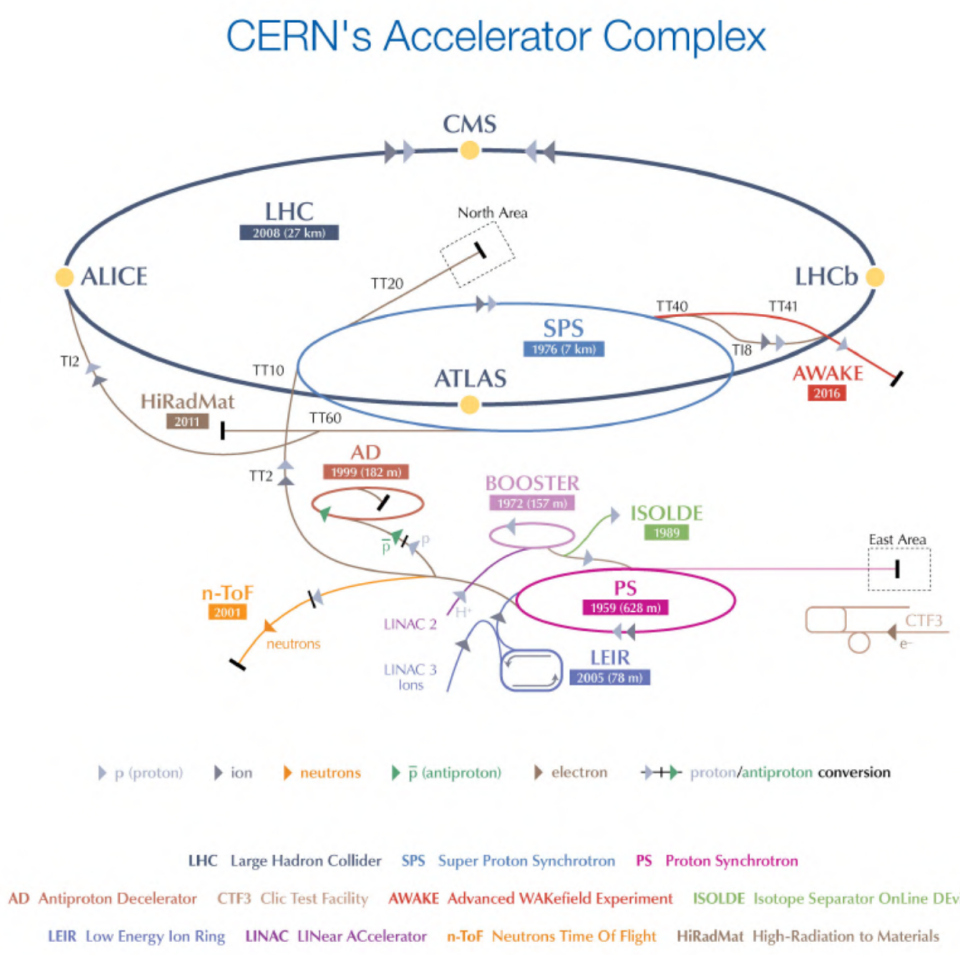


Figure 2.1: Overview of CERN's accelerator complex showing the proton acceleration chain through LINAC 2, Booster, PS, and SPS before injection into the LHC ring, where four major experiments are positioned at beam intersection points [34].

recreating the conditions of the early universe, studying the super-hot, dense state of matter that existed just after the Big Bang. Every collision inside the LHC is like opening a new page in the book of the universe. Each discovery brings us closer to answering some of the deepest questions in science. What is dark matter? Are there hidden dimensions? What lies beyond the Standard Model of physics? The LHC is not just a machine; it is a time machine, a detective, and a storyteller, all working together to reveal the secrets of the cosmos. And as the current run continues,

scientists around the world are watching closely, knowing that the next big discovery could be just around the corner.

2.2 ATLAS Detector

ATLAS (A Toroidal LHC ApparatuS), As showing in Figure 2.2[39], with its cylindrical structure 44 meters long and 25 meters in diameter, ATLAS covers almost the entire solid angle (4π radians) around the central interaction point and weighs around 7,000 tons, giving it the largest detector of its type ever built.

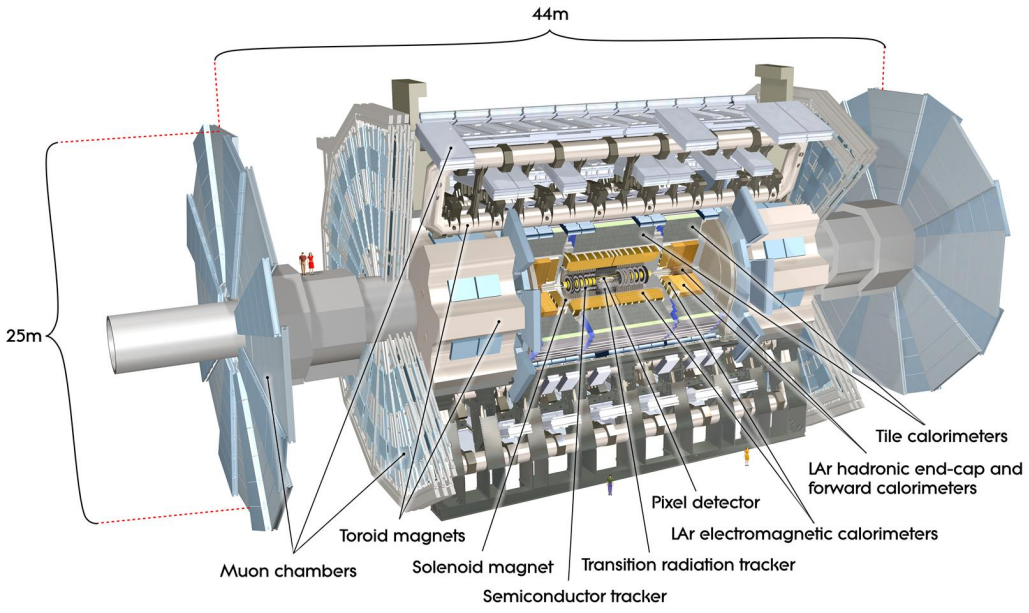


Figure 2.2: Cut-away view of the ATLAS detector [40].

2.2.1 ATLAS Coordinate System

The ATLAS detector employs a conventional coordinate system, with origin defined at the nominal Interaction Point (IP) at the center of the detector, as shown in Figure 2.3[40]. The coordinate system is essential for describing the precise trajectories and properties of particles produced in collisions.
In the Cartesian coordinates, the z axis is aligned with the beam pipe, indicating

the direction of the colliding proton beams. While the x-axis is oriented from the IP to the center of the LHC ring, the y-axis is vertically upwards, completing the orthogonal coordinate system.
Transverse plan: In the perpendicular plane of the beam axis, cylindrical coordinates (r, ϕ) are employed, where r is the radial distance from the z-axis and ϕ is the azimuthal angle around the z-axis, which is measured in radians. The transverse momentum (p_T) of the particles, which is a key quantity in collision analysis, lies in this plane. Pseudo-rapidity: Rather than the polar angle θ, pseudorapidity η is commonly used, defined as:

$$\eta = -\ln[\tan(\theta/2)] \tag{2.1}$$

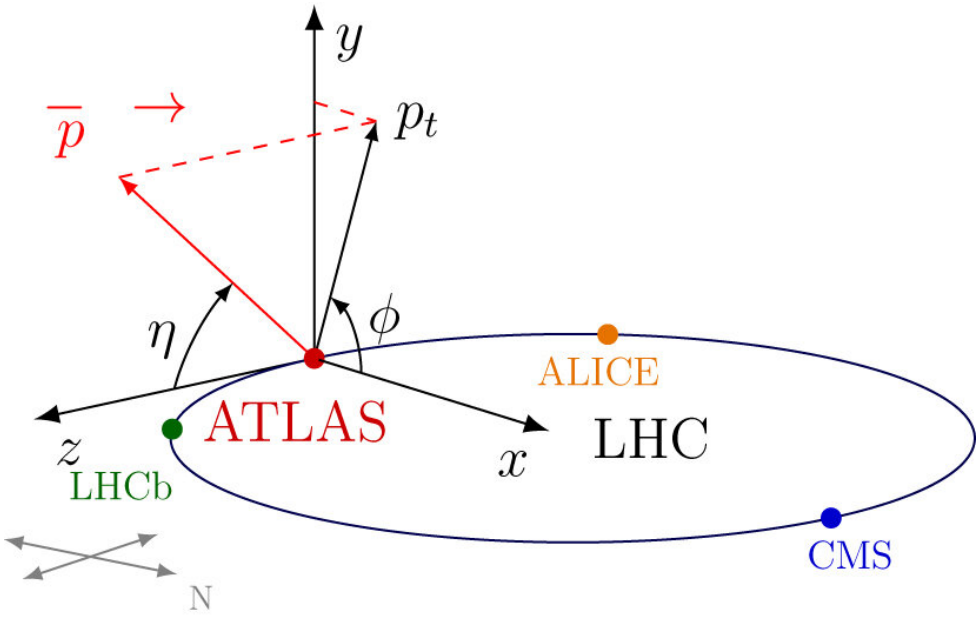


Figure 2.3: The ATLAS Coordinate System, showing the x, y, and z axes, as well as the angles ϕ and η, and the location of other LHC experiments[40].

It is a good approximation to rapidity, which is the Lorentz transformation of the z component of momentum.
Detector arrangement: The ATLAS detector is subdivided into a barrel region, in which the detector layers are positioned on cylindrical surfaces surrounding the beam axis, and two endcap regions, in which the detector layers are positioned in planes perpendicular to the beam pipe. This configuration provides almost complete solid angle coverage around the interaction point, enabling full detection of the particles produced in the collisions.

2.2.2 Inner Detector

The inner detector (ID) is the innermost system of the ATLAS detector, providing precise tracking of charged particles as shown in Figure 2.4. An axial magnetic field of 2 T provided by a superconducting solenoid. The ID is designed to reconstruct the paths of charged particles with a high degree of precision, enabling the exact determination of their momentum, charge and origin.

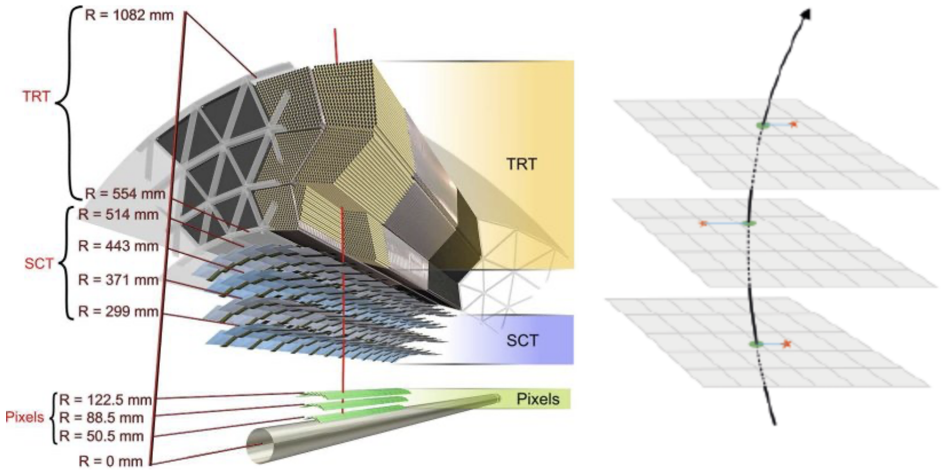


Figure 2.4: Structure of the ATLAS ID and particle track reconstruction [41].

Layout and Technology:
As shown in Figure 2.4, the ID consists of three main subsystems, arranged in a cylindrical geometry around the beam axis.

1. **Pixel Detector**: The pixel detector, positioned closest to the beam pipe, forms the innermost component of the Inner Detector (ID). Its proximity to the beam pipe enhances vertex reconstruction precision. The detector comprises two end-caps, each containing three disks, and a barrel section with four layers. The barrel itself consists of three distinct layers—B-layer, L1, L2, and L3—each measuring 80cm in length and placed at distances of 5.05cm, 8.85cm, and 12.25cm from the beam pipe's center, respectively. It covers a pseudorapidity range of $|\eta| < 2.5$. The pixel detector is built from silicon sensor modules that detect charged particles by ionizing the active material. Its primary sensing

elements are pixelated structures measuring 50μm $\times$ 400μm, providing a spatial resolution of 10μm in the x–y plane and 115μm in the z-direction. Ahead of the Run 2 data-taking period, the Insertable B-Layer (IBL) [42], was added between the beam pipe and the original system. This enhancement improved tracking efficiency for short-lived b-quark decays while also offering additional radiation protection for the existing layers. The IBL features smaller pixels, measuring 50μm $\times$ 200μm, with a hit accuracy of 8μm in the x–y plane and 40μm in the z-direction.

2. **Semi-Conductor Tracker**:The Semiconductor Tracker (SCT) serves as the central component of the Inner Detector, bridging the pixel detector and the outer transition radiation tracker. It features a layered structure, consisting of four barrel layers and two endcaps, each containing nine discs. Positioned at radial distances between $299mm$ and $560mm$ from the beamline, the SCT plays a crucial role in reconstructing particle trajectories with high precision.
   The SCT consists of 4,088 silicon detector modules, integrating a total of 6.3 million microstrips. These modules utilize single-sided p-on-n silicon microstrip technology, with 2,112 modules embedded within the barrel and 988 in each endcap. Uniquely designed as double-sided detectors, they enable precise spatial tracking by providing eight position measurements for every passing particle.
   Covering a pseudorapidity range of $|\eta| < 2.5$, the SCT significantly enhances tracking capabilities, ensuring accurate momentum and vertex reconstruction within the detector system.

3. **Radiation Tracker**: The Transition Radiation Tracker (TRT) [42] is the outermost part of the ID, extending up to $|\eta| < 2$. Unlike conventional tracking systems arranged in layers, the TRT consists of tightly packed straw tubes, each just $4mm$ in diameter. Inside each tube, a gold-plated tungsten wire is suspended within a xenon-based gas mixture, with small amounts of CO_2 and O_2 aiding the ionization process.
   Charged particles passing through the detector leave a trail of ionized gas, generating signals that allow for precise tracking. While individual straws have limited position resolution, the detector compensates with an exceptionally high number of hits along each particle's path. The barrel section contains over 50,000 tubes extending radially from the beamline, while the endcaps feature more than 120,000 tubes, positioned perpendicular to the beam pipe.
   Beyond simple tracking, the TRT excels at particle identification.

Polypropylene fibers interwoven among the straws produce transition radiation when high-energy charged particles cross material boundaries. This effect enhances the detector's ability to distinguish electrons and positrons from heavier particles like pions, making it an essential component of the tracking system.

Tracking Performance:
The tracking performance of the ID is crucial for many physics analyses at the LHC. The design enables highly efficient and accurate reconstruction of charged particle tracks over a wide range of pseudorapidity ($|\eta| < 2.5$) and transverse momentum (p_T). High granularity and precision of the detector elements permit the resolution of closely spaced traces in the high-multiplicity environment of proton-proton collisions. The accuracy achieved for track parameters is determined by several factors, including the intrinsic resolution of the sensitive devices, magnetic field knowledge, material distribution in and in front of the ID, and geometry of detector elements, i.e. their location and orientation. The ID collected data with over 99% efficiency during the LHC's data-taking.

2.2.3 Calorimeters

The calorimeter system in ATLAS is designed to measure particle energy by capturing and analyzing their interactions with detector materials. This system employs sampling calorimeters, which consist of alternating layers of dense absorber materials and active detection components. The absorber layers, composed of high-density materials, initiate particle interactions, producing cascades of secondary particles while also absorbing a portion of their energy. The active layers then record the energy released in these interactions.
Because some of the initial energy is lost within the absorber, the measured values represent only a fraction of the particle's true energy. Calibration is therefore essential to accurately reconstruct the total energy of the interaction. The calorimeter system effectively measures both charged and neutral particles, with the exception of muons and neutrinos, which pass through with minimal interaction .
The ATLAS calorimeter system is made up of two main parts: the electromagnetic calorimeter (ECAL) and the hadronic calorimeter (HCAL) as illustrated in Figure2.5.

1. **Electromagnetic Calorimeter (ECAL)**: The ECAL precisely measures the energy of electromagnetically interacting particles, in particular electrons, positrons and photons. It is a sampling calorimeter, alternating layers of an absorbing material (lead) with an active medium (liquid argon).

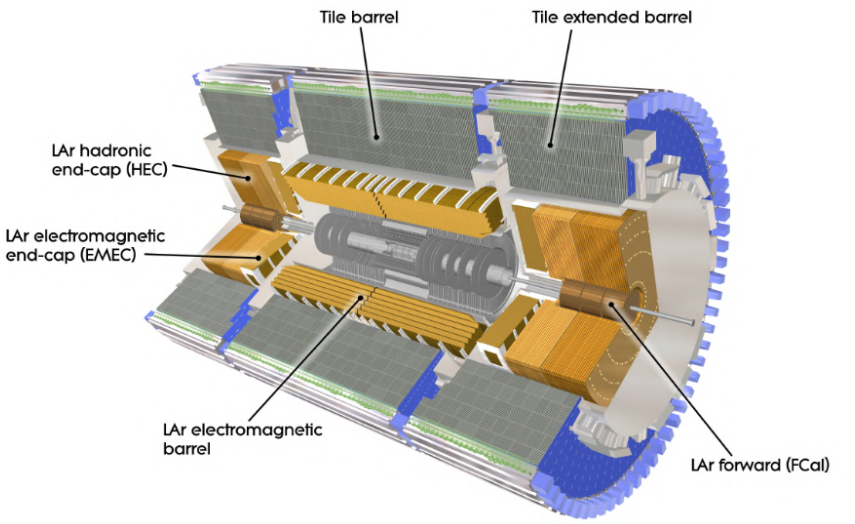


Figure 2.5: Cutaway view of the ATLAS calorimeter system [43].

- **Technology:** ECAL employs a liquid argon and lead (LAr) sampling technique. Lead plates act as absorbers, enabling incoming high-energy photons and electrons trigger electromagnetic showers through bremsstrahlung and pair production within the lead absorbers. The gaps of liquid argon between the lead plates serve as the active medium. As the charged shower particles pass through the liquid argon, they ionize the argon atoms. The ionization charge is then collected by electrodes, providing a signal proportional to the energy deposited.
- **Structure:** The ECAL is split into a barrel section (EMB) which covers the pseudorapidity region $|\eta| < 1.475$, and two end sections (EMEC) covering $1.375 < |\eta| < 3.21$. In the $|\eta| < 2.5$ region, it is separated into three layers. The first, also known as the strip layer, is has a very small cell size in ($\Delta\eta \times \Delta\phi = 0.003 \times 0.1$) to enable event-by-event discrimination between single and overlapping photon showers, such as produced by pi^0 decay. The second layer collects most of the energy deposited in the calorimeter by EM showers, having a thickness of around 17 radiation lengths and a granularity of $\Delta\eta \times \Delta\phi = 0.025 \times 0.0251$. The third layer, with a granularity of $\Delta\eta \times \Delta\phi = 0.05 \times 0.025$, serves to correct leakage beyond the EM1 calorimeter. A thin presampler detector, located in front of the main ECAL, corrects for upstream energy loss in the detector

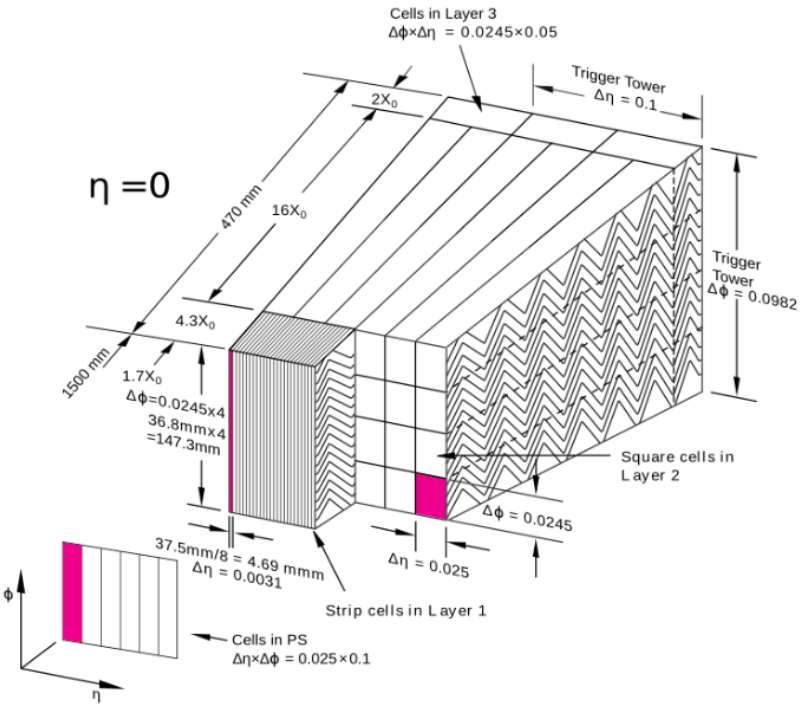


Figure 2.6: Sketch of a barrel module in the electromagnetic calorimeter at $\eta = 0$. The granularities of the cells in three different layers in η and ϕ are also shown [44].

material, Figure2.6[44].

- **Performance:** ECal is carefully structured to ensure precise energy measurements. It consists of a barrel and endcaps, each divided into three layers, with an additional thin presampler positioned close to the inner detector. This presampler plays a key role in correcting for the energy particles lose while traveling from the interaction point to the ECal.
  The first layer, designed with fine granularity in , enables high-precision photon position measurements. This feature is crucial for identifying high-energy neutral pion decays, specifically $\pi^0 \rightarrow \gamma\gamma$. Most of the particle shower's energy is captured in the second layer, while the third layer records the remaining tail of the shower.
  To ensure electrons and photons are fully absorbed, the ECal is designed with sufficient depth to stop them completely. Additionally, a cryostat surrounds the ECal, maintaining the low temperatures required for the

liquid argon medium to function optimally.

2. **Hadronic Calorimeter (HCAL)**: hadronic calorimeters (HCal) [44] are specialized in detecting and measuring the energy of hadrons, with a key emphasis on capturing the energy and spatial distribution of hadronic jets. The Hcal is comprised of three components: the tile calorimeter, the hadronic endcap calorimeter (HEC), and the forward calorimeter (FCal). In contrast to the electromagnetic calorimeter (ECal), the HCal operates with lower granularity and resolution. This is due to its necessity for greater material depth to fully absorb the energy of hadronic showers. As a result, the HCal is larger and thicker than its electromagnetic counterpart. Its primary role is to quantify the energy of jets, which are composed of particles created during the hadronization of quarks and gluons.

- **Technology:** The HCAL uses various technologies in its different sections. The tile calorimeter covers the central region, using steel as the absorber and scintillating tiles as active medium. In the forward regions are the hadronic endcap (HEC) and forward (FCAL) calorimeters, employing liquid argon technology similar to that used by ECAL, but with denser absorber materials (copper or tungsten).

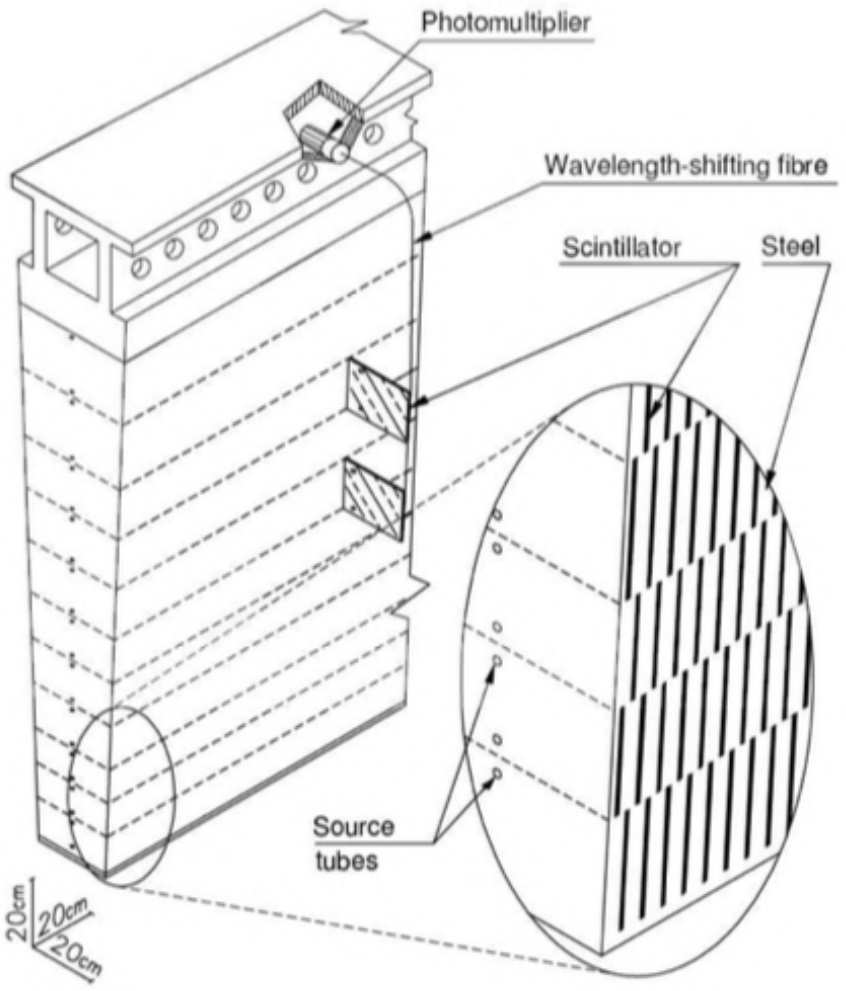


Figure 2.7: Sketch of a barrel module in the tile Calorimeter, showing the major components of the optical read-out, including the tiles, the fibers and the PMTs [45].

- **Structure:**
  - **Tile Calorimeter:** The most important part of the HCAL, covering the central region. It is built up of absorbing steel plates interwoven with scintillating tiles. As particles pass through the tiles, they produce scintillation light, which is collected by variable-wavelength fibers and read by photomultiplier tubes (PMTs).
  - **End-Cap Hadronic Calorimeter (HEC):** Located in the end-cap areas, CHE works with liquid argon as the active medium and copper as the absorber. It provides excellent performance in high-radiation environments.
  - **Forward Calorimeter (FCal):** The FCal is positioned at very small angle to the beam and is designed to measure particles produced in the forward direction. Liquid argon is used as the active medium and tungsten as the absorber, giving it high density and resistance to radiation [44].
- **Performance:** Although the energy resolution of the HCAL is lower than the ECAL, the HCAL is sufficient to measure the total energy of the jets (collimated hadron jets) and to measure the missing transverse energy (MET), an important signature for new physics.

ATLAS detector selects events using a multi-stage triggering system. The calorimetric system, coupled with the precision of the internal detector and muon identification by the muon spectrometer, allows ATLAS to measure precisely known Standard Model processes and to search for new physics phenomena.

2.2.4 Muon Spectrometer

The Muon Spectrometer (MS) is positioned at the outermost layer of the ATLAS detector, designed to provide precise tracking of muons in the region $|\eta| < 2.7$, independent of the Inner Detector (ID). As illustrated in Figure2.8, the MS incorporates magnets and sub-detectors arranged to optimize its functionality. It also plays a crucial role in triggering the recording of events for muons within the $|\eta| < 2.4$ range. The MS includes a toroidal superconducting magnet system that creates a magnetic field to bend the muons' trajectories. It features two types of chambers: high-precision Type I chambers, like Monitored Drift Tubes (MDTs) in the barrel and Cathode Strip Chambers (CSCs) in the forward region, which provide detailed momentum measurements, and fast Type II chambers, such as Resistive Plate Chambers (RPCs) in the barrel and Thin Gap Chambers (TGCs) in the end-cap, which

are responsible for triggering based on muon tracks [44]. In the barrel, eight superconducting coils produce a 4 T magnetic field to curve muons in the $|\eta| < 1.4$ region, while the end-caps use two smaller toroidal magnets to generate a 4 T field for the region $1.6 < |\eta| < 2.7$. Both magnet systems are utilized in the transition region to ensure the accurate bending of muon trajectories.

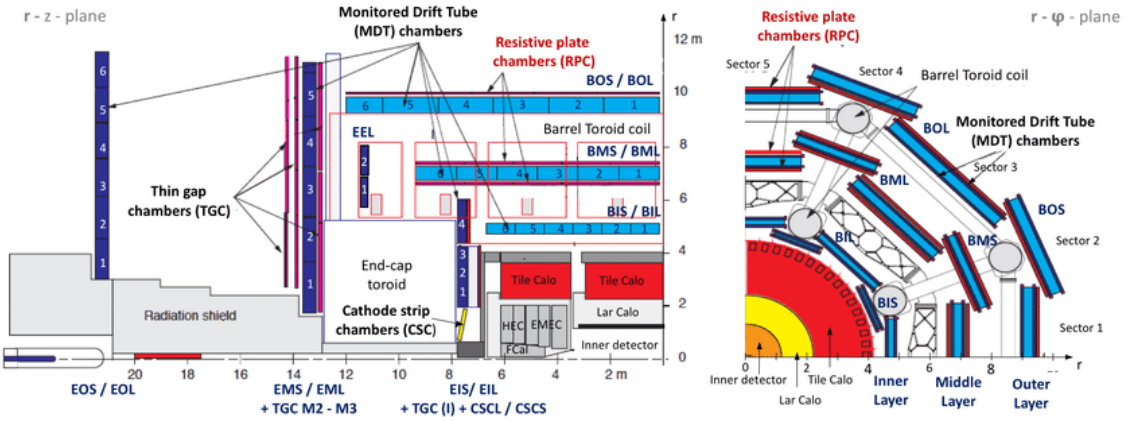


Figure 2.8: The general layout of the ATLAS Muon Spectrometer [46].

To achieve precise measurements, the muon spectrometer uses various detection technologies:

- **Precision Tracking Chambers:** The precision tracking chambers in the Muon Spectrometer (MS) include Monitored Drift Tubes (MDTs) and Cathode Strip Chambers (CSCs). MDTs cover the region $|\eta| < 2.7$, except for the high radiation zone ($2.0 < |\eta| < 2.7$), where CSCs are used instead. MDTs are composed of pressurized drift tubes, roughly 3 cm in diameter, filled with a gas mixture of 93% Argon and 7% Carbon dioxide, selected for its stability over time. These tubes are organized into layers, which are then grouped into chambers, arranged along the ϕ direction for both the barrel and end-cap regions. While the tubes in the barrel chambers are of uniform length, in the end-cap chambers, the tube lengths vary with the radius. In the forward region ($2.0 < |\eta| < 2.7$), MDTs are replaced by CSCs, which are multiwire proportional chambers with wires oriented radially. CSCs offer exceptional spatial and temporal resolution, double-track capability, and are highly resistant to neutron interference. The cathodes are segmented with one set of strips perpendicular to the wires and another set parallel, providing the necessary trans-

verse coordinate. The CSCs deliver a resolution of 60 μm per plane and 5 mm in the transverse direction.

- **Trigger Chamber:** The trigger chambers are essential for providing quick insights into muon tracks as they move through the detector, allowing the Level 1 (L1) trigger system to evaluate their quantity and estimate their energy range. In the barrel region ($|\eta|1.05$), this is achieved using three concentric layers of Resistive Plate Chambers (RPCs), strategically placed around the beam axis. Each RPC consists of two parallel resistive plates, separated by just 2 mm, and filled with a gas mixture of 94.7% tetrafluoroethane, 5% isobutane, and 0.3% sulfur hexafluoride. This setup provides rapid detection of muons as they pass through. Further out in the forward region ($1.05 < |\eta| < 2.4$), the trigger system relies on Thin Gap Chambers (TGCs). These chambers are multiwire proportional devices, characterized by a small gap between the wire and the cathode. TGCs are designed to offer high precision, with spatial resolution ranging from 2-6 mm in the radial direction and 3-7 mm in the azimuthal direction, ensuring reliable tracking in this more complex area of the detector.

2.2.5 Trigger and Data Acquisition System

At the LHC, protons are collided in bunches every 25 nanoseconds, producing a collision rate of 40 MHz. This immense data flow would be impossible to store on tape, which is why ATLAS employs a sophisticated multi-layered Trigger and Data Acquisition system (TDAQ) [47]. The purpose of this system is to determine which events are of particular interest and should be selected for permanent storage and further analysis. The ATLAS trigger system operates in two stages: the Level 1 (L1) hardware trigger and the High-Level Trigger (HLT). The L1 trigger, based on hardware, processes data from the Calorimeters and Muon Spectrometers to reduce the data rate to 100 kHz, with each decision being made in less than 2.5 microseconds. Once an event passes this initial filter, it is temporarily stored in buffers. If the event meets specific criteria, it moves on to the second stage, the High-Level Trigger. The HLT, a software-based system, further refines the selection process, leveraging around 40,000 CPU cores to analyze collision events and data from various sub-detectors. This process reduces the event rate from 100,000 per second to around 1,000 per second. The events that make it through this second filter are then permanently stored for in-depth analysis.

2.3 ATLAS Experiment Phase II Upgrade:

The High-Luminosity Large Hadron Collider (HL-LHC) [27] is a major upgrade of the LHC, set to begin operations in 2030. It is designed to achieve an integrated luminosity of up to 4000 fb^{-1} at a center-of-mass energy of $\sqrt{s} = 14$ TeV. With a peak instantaneous luminosity reaching $\mathcal{L} = 7.5 \times 10^{34}$ cm^{-2}s^{-1}, the HL-LHC will generate approximately 200 inelastic proton-proton collisions per beam crossing (pile-up), a significant increase from the 60 pile-up events recorded during Run 2 of the LHC. The HL-LHC upgrade will significantly extend the capabilities of the ATLAS experiment, allowing for a more comprehensive exploration of fundamental physics. This includes achieving greater precision in Standard Model measurements and refining the study of Higgs boson properties, particularly the observation of Higgs self-couplings. Moreover, the enhanced detector performance and increased data collection will push the search for beyond Standard Model (BSM) phenomena to higher mass scales, further expanding the experiment's discovery potential. Figure 1 illustrates the HL-LHC phase timeline, aligned with the baseline LHC program.



Figure 2.9: The core LHC program and the upcoming HL-LHC operation

The ATLAS detector, particularly its inner tracking system, was originally designed for a decade of operation under a steady instantaneous luminosity of $\mathcal{L} = 7.5 \times 10^{34}$ cm^{-2}s^{-1}, with a maximum integrated luminosity of 1000 fb^{-1}. However, the HL-LHC will push these limits significantly, exposing the detector to extreme

radiation levels. To maintain performance and withstand these harsher conditions, extensive upgrades to ATLAS sub-systems will be essential.
The Phase-II upgrade introduces several key enhancements. First, the all-silicon Inner Tracker (ITk) [48] will replace the existing inner tracker, extending coverage across rapidity and providing improved performance. The trigger and data acquisition systems for both the calorimeters [49] and the muon [50] detectors will also be redesigned, paving the way for a free-running readout system. A major addition to the system is the High Granularity Timing Detector (HGTD) [51], which will be installed in the forward region. This new subsystem will help associate tracks with their vertices more accurately, using timing information to reduce the effects of pile-up and refine the reconstructed tracks.

2.3.1 The Inner Tracker:

At the HL-LHC, the ATLAS Inner Detector (ID) will undergo a major upgrade, replacing the existing system with an all-silicon Inner Tracker (ITk). The ITk will consist of two primary subsystems: a Pixel Detector at its core, enveloped by a Strip Detector. Figure 2.10 illustrates the ITk's layout in the (r-z) plane, highlighting the new design.
This upgrade brings a dramatic increase in coverage, extending the pseudo-rapidity range to $|\eta| = 4$, a significant improvement over the current ID, which only reaches $|\eta| = 2.5$. This extension will enable the track reconstruction of objects in the forward region for the first time, offering new opportunities for analyses involving forward electrons in final states. Additionally, it will enhance studies of vector boson scattering, increasing the sensitivity of experiments by expanding the reach into the forward region.

2.3.2 The High-Granularity Timing Detector (HGTD):

The HL-LHC presents a significant challenge due to the rapid increase in simultaneous interactions, with up to 200 pile-up events occurring near the primary vertex. This issue is exemplified by the pile-up vertex density distribution under two scenarios: $<\mu> = 200$, anticipated for HL-LHC operations, and $<\mu> = 38$, representing conditions from Run 2. With event densities reaching 4 vertices/mm, identifying primary vertices becomes increasingly complex for the ATLAS detector. The ITk is designed to maintain or surpass the track reconstruction and vertex association performance of the Run 2 ID while extending pseudo-rapidity coverage. However, in the forward region (high $|\eta|$ values), the resolution of the longitudinal impact parameter (σ_{z0}), a crucial factor in vertex separation, deteriorates for low–p_{T} particles. This challenge stems from the increased distance between the initial detector layer

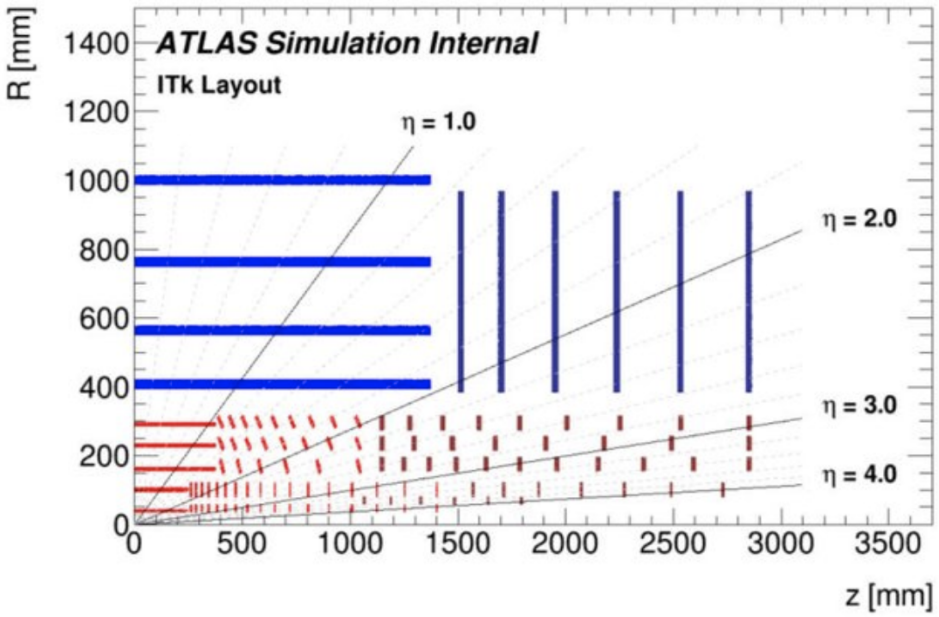


Figure 2.10: Schematic layout of the ITk for HL-LHC phase of ATLAS [52].

and the collision point, as well as the additional material the tracks must traverse. A direct consequence of this resolution decline is a greater probability of pile-up tracks being incorrectly associated with the hard-scatter vertex. To effectively distinguish vertices, σ_{z0} must be finer than the inverse of the average pile-up density, approximately 600 m. While this criterion is met in the central region, it becomes increasingly difficult to achieve in the forward region, where resolution values can reach 3 mm for low–p_{T} particles at $|\eta| \approx 4$.

To mitigate the effects of pile-up in the forward region, a novel method incorporates the time of arrival of tracks alongside spatial measurements. This improvement will be implemented through the High Granularity Timing Detector (HGTD), a newly designed detector located in the forward region ($2.4 < |\eta| < 4.0$). Employing Low Gain Avalanche Detectors (LGADs) [53], the HGTD will provide high-precision time measurements, starting with a resolution of 30 ps per track and gradually degrading to 50 ps over its operational lifetime.

Beyond tracking capabilities, the HGTD will function as a luminometer, aiding in luminosity measurements. Positioned between the barrel and end-cap calorimeters, at an approximate distance of ± 3.5 meters from the nominal interaction point, the HGTD will replace the Minimum Bias Trigger System (MBTS). Figures 2.11 and 2.12

illustrate the placement of the HGTD vessels within the ATLAS detector, while a detailed examination of the HGTD is provided in Chapter 4.

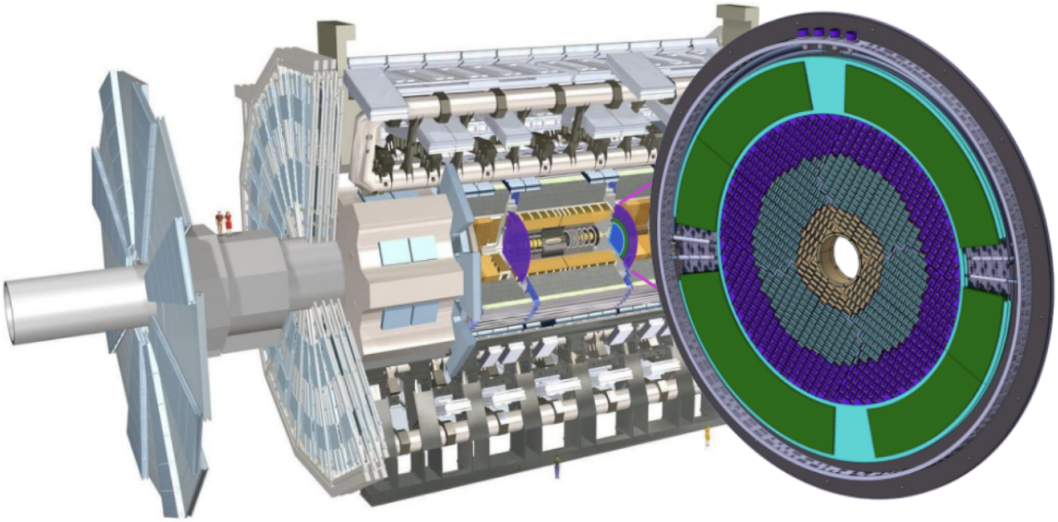


Figure 2.11: Layout and sensor performance of the HGTD [54].

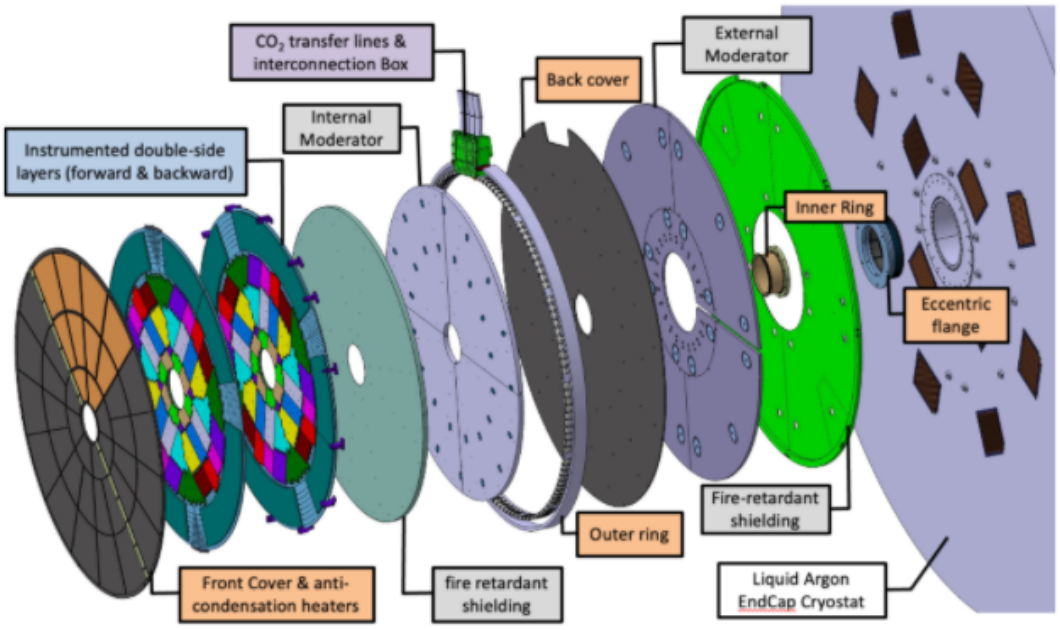


Figure 2.12: Layout and sensor performance of the HGTD [54].

3

Physics Object Reconstruction

The foundations laid in the previous discussions - exploring both the theoretical and the experimental set-up - provide the basis for the essential challenge of identifying and characterizing the particles produced in high-energy collisions. The Large Hadron Collider, with its intense proton-proton collisions at a center-of-mass energy of 13 TeV, generates a vast and complex data set that requires meticulous analysis to produce significant physical insights. At the core of this analysis is the physical object reconstruction process, converting raw detector signals into recognizable physical entities, from charged particle tracks, vertices, leptons, jets and missing transverse momentum. The methodologies and algorithms used in this reconstruction are crucial to unlock the complex interactions within these collisions, enabling precise measurements and opening the door for the discovery of new phenomena. In the following section, we look at the reconstruction methods used to reconstruct physical objects, examining their applications, challenges and future prospects.

3.1 Physics Objects Reconstruction and Identification

In the ATLAS experiment, a sophisticated set of algorithms is used to transform the raw signals collected by the detector into significant physical quantities. These algorithms integrate and process the detector's individual signals from various subsystems to reconstruct physical objects such as electrons, muons, photons, jets and so on. By identifying the type and kinematics of these objects, physicists can extract valuable information for their analyses.
Reconstruction processes start with the identification of traces in the ID or MS. In the case of muons, for instance, results obtained in the ID and the MS are combined to obtain an estimation of the particle's momentum. These tracks are then matched with groups of energy deposits in the calorimeters to obtain a complete picture of the object's properties. This step is key in determining crucial kinematic variables such as p_T,η and ϕ.
Such a systematic approach guarantees that each signal from the detector is interpreted precisely and associated with a specific physical object, forming the foundation for all further analyses in ATLAS.

3.2 Tracks and Vertices

Track and vertex reconstruction is a fundamental part of the ATLAS experiment's analysis pipeline. It is a major factor in understanding the complex interactions taking place during high-energy collisions at the LHC. ATLAS's internal detector, comprising layers of pixels, stripes and TRT (Transition Radiation Tracker), provides precise measurements of charged particle trajectories. This process starts with forming spatial points from the pixel and stripe detectors' clusters, and from the TRT's drift circles, which are then transformed into 3D spatial points. The seeds formed from sets within the spatial points are used to initiate candidate tracks, subsequently refined using a Kalman filter [55] to add additional results from the silicon detectors. The inside-out tracking algorithm is one of the main methods used in this process. It involves several steps, starting with seed creation from sets in space, which are then expanded into full trajectory candidates using the Kalman filter. This algorithm adds iteratively results from silicon detectors to refine the trajectory parameters, ensuring precise particle moment and charge determination. Recently, optimizations for the third LHC cycle have focused on improving the efficiency and rapidity of this procedure under increased pile-up conditions. Once all candidate tracks have been reconstructed, a vertex reconstruction procedure identifies interaction points through clustering tracks with compatible z-positions along

the beamline. This procedure is followed by vertex adjustment to establish vertex positions and uncertainties. Recent optimizations for LHC run 3 focused on enhancing efficiency and rapidity of those processes in higher pile-up conditions. To improve the efficiency of track reconstruction and reduce design costs, the ACTS framework was implemented. In addition, machine learning techniques, such as convolutional neural networks (CNNs), are investigated in order to enhance vertex tracking efficiency. For example, a vertex searcher based on convolutional neural networks has been developed to estimate the z-position probability distribution, thereby increasing vertex search efficiency. Vertex position resolution enhances with the increasing track count in the vertex, highlighting the importance of precise vertex reconstruction for identifying specific decay modes. Such improvements prove crucial to maintaining high reconstruction efficiency and precision against increasing luminosity and pile-up conditions. The ability to reconstruct tracks and vertices precisely has a direct impact on the performance of subsequent analyses. As the LHC continues to operate at higher luminosities, additional optimizations will be required to ensure that the ATLAS detector remains capable of providing precise measurements of complex interactions.

3.3 Leptons

Leptons, including electrons, muons and tau leptons, are fundamental particles of the Standard Model. Their characteristic signatures, and sensitivity to new physics phenomena, make them a key element in many analyses. ATLAS is equipped with advanced systems for the precise identification and measurement of leptons, indispensable for both Standard Model measurements and the investigation of new physics beyond the Standard Model.

3.3.1 Electrons Reconstruction

As depicted in Figure 3.1, electron reconstruction in the ATLAS detector is a sophisticated process that exploits their unique characteristics. The process begins when an electron from the point of interaction passes through the internal detector. The system works on the principle of tracking charged particles, and consists of several sub-detectors, including the insertable B-layer (IBL), pixel detectors, semiconductor tracker (SCT) and transition radiation tracker (TRT) [56]. The pixel detectors and the SCT provide precise measurements of the electron's trajectory, enabling accurate determination of the momentum. As the electron travels through the TRT(comprising 72 layers), it emits transition radiation photons due to the change in refractive index between different materials. Photons are then detected, giving additional information to distinguish electrons from heavier charged particles such as

hadrons. After crossing the internal detector, the electron enters the electromagnetic calorimeter (EMCal). where the energy deposited by electrons and photons through electromagnetic showers is measured.
Electrons deposit almost all their energy in the EMCal, and the shape and energy of these electromagnetic showers are key variables used for electron identification. A good track (Sect 3.2) match with a well-formed electromagnetic shower in the EMCal is a primary signature of an electron candidate.

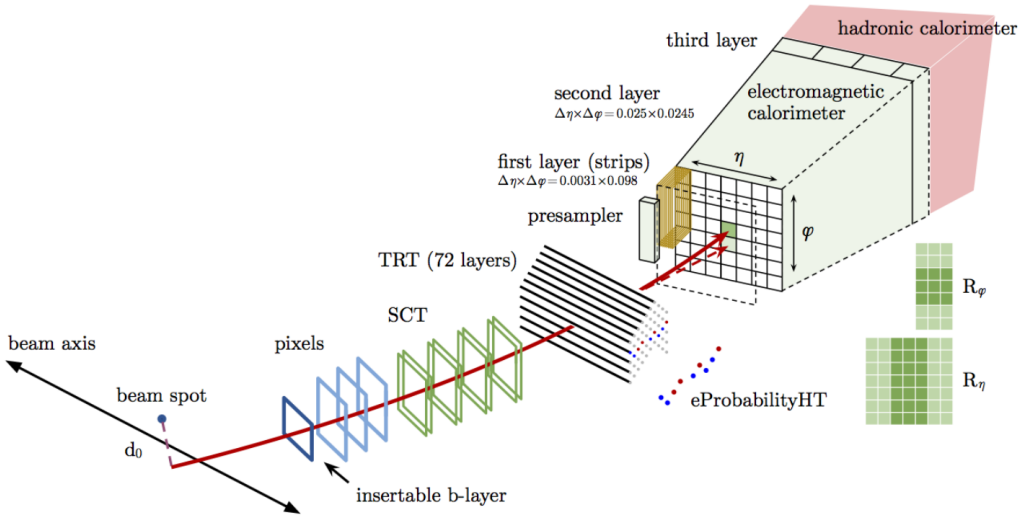


Figure 3.1: Schematic view of the electron path through the detector [57].

3.3.2 Electrons Identification

Electron identification (eID) in ATLAS is fundamental to selecting true electrons from misidentified particles, such as jets or photons that are converted into electron-positron pairs. Identification is based on a combination of discriminant variables associated with the shape of electromagnetic shower in the calorimeter and track quality corresponding to the shower.
ATLAS experiment uses multiple levels of eID criteria, generally classified as "Loose", "Medium" and "Tight", with each designed to optimize signal efficiency and background rejection. Figure 3.2 illustrates the performance of these different electronic identification criteria. More precisely:

- **Loose cuts**: consist of simple cuts on variables associated with the shower shape and the match between the reconstructed trajectory and the calorimeter

cluster

- **Medium cuts**: It also involves cuts in variables related to shower shape, although it uses additional information provided by the first layer of the electromagnetic calorimeter. It also employs track quality cuts resembling standard reconstruction cuts, in order to balance efficiency and purity.

- **Tight cuts**: Prioritize purity over efficiency, applying strict criteria for track matching, and reducing the energy/momentum ratio. In addition, it requires a vertex layer hit on the track and a high ratio between high-threshold and low-threshold hits in the TRT.

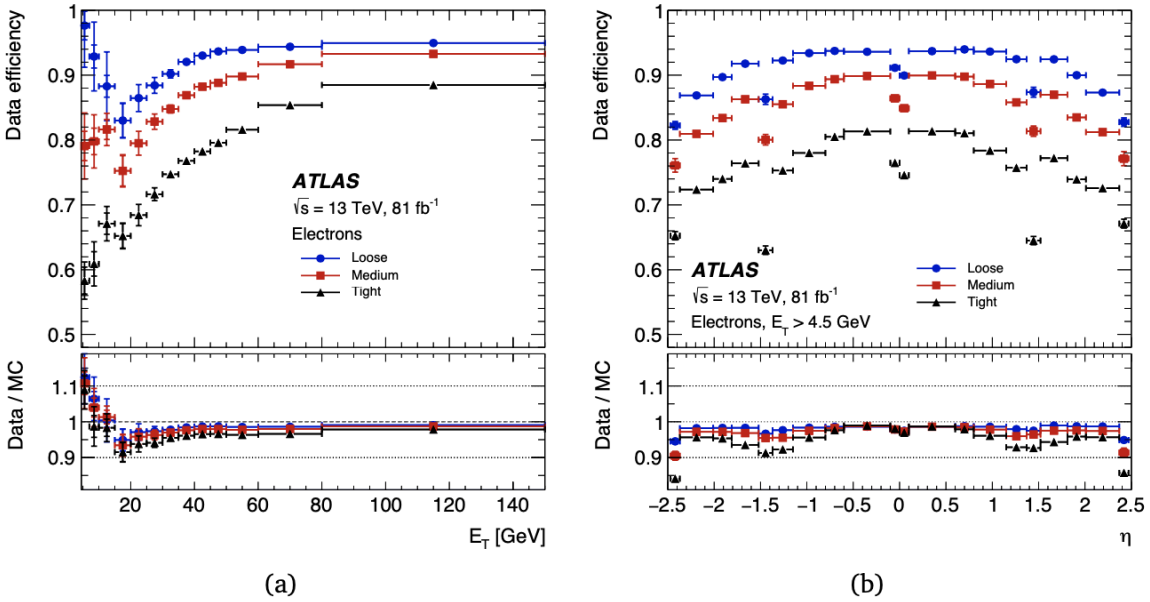


Figure 3.2: The electron identification efficiency in $Z \to e^+e^-$ events as function of E_T (a) and as function of η (b) for the three Working Points, (WPs): Loose, Medium, and Tight [58].

These different levels of eID rigor enable analyses to be optimized according to specific needs. Unlike these cutting-based methods, ATLAS also uses a likelihood-based identification method, providing a multivariate technique (MVA) developed and implemented in the ATLAS software. This approach simultaneously evaluates several properties of candidate electrons when making selection decisions. Figure 3.3,

illustrates a discriminant distribution that is transformed for prompt electrons from Z boson decay and for background, demonstrating the discriminating power of this technique.

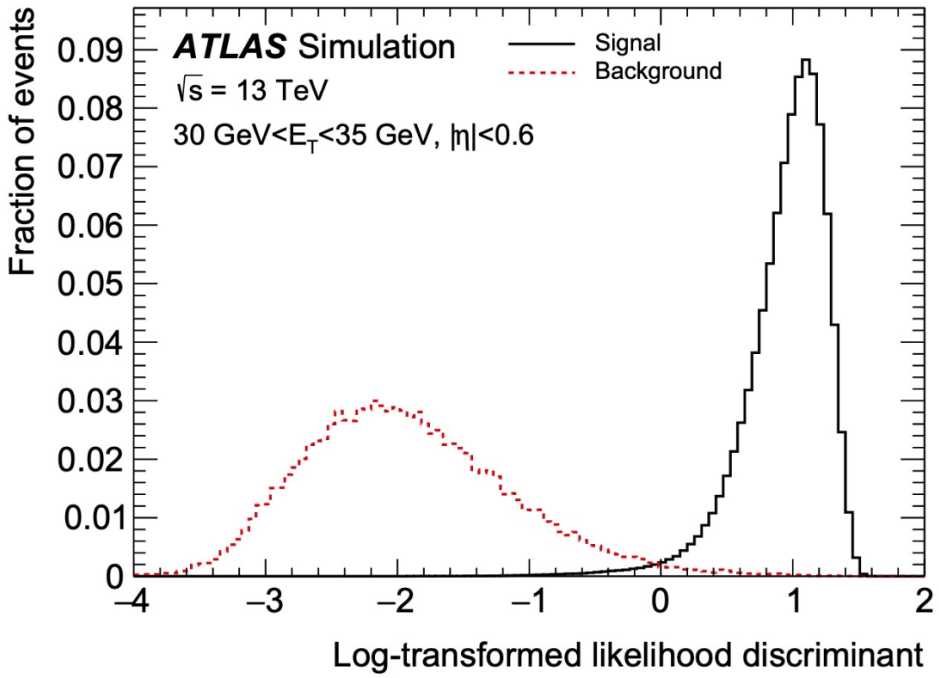


Figure 3.3: The transformed LH-based identification discriminant dL for reconstructed electron candidates with good quality tracks with $30GeV < E_T < 35GeV$ and $|\eta| < 0.6$, where the signal is for prompt electrons in a $Z \to ee$ process [58].

The LH discriminant dcdc is based on the probability that a reconstructed electron comes from the signal (electrons) or the background (misidentified particles). It uses PDFs of the signal (LSLS) and background (LBLB) which are obtained from the data and treated as uncorrelated. The LH discriminant dL is calculated as:

$$d_{\mathcal{L}} = \frac{\mathcal{L}_S}{\mathcal{L}_S + \mathcal{L}_B}, \text{ with: } \mathcal{L}_{S(B)}(\vec{x}) = \prod_{i=1}^{n} \mathcal{P}_{S(B),i}(x_i). \tag{3.1}$$

As the dcdc discriminant has a clear peak close to unity (zero) for the signal, which makes the selection of operating points more difficult, as this would require extremely precise binning, an inverse sigmoid function is used to convert the discriminant distribution:

$$d'_{\mathcal{L}} = -\tau^{-1} \ln(d_{\mathcal{L}}^{-1} - 1), \tag{3.2}$$

where the parameter takes the value 15 [59]. Electron-likelihood identification imposes other requirements than the selection of the likelihood discriminant, with significant discriminant power. This MVA-based approach enables ATLAS to achieve high-performance electron identification over a wide range of kinematic and detector conditions.

3.3.3 Muons Reconstruction

Muon reconstruction starts with track segments reconstructed independently in the muon spectrometer (MS), the outermost component of ATLAS. These track are then mapped back to the tracks reconstructed in the internal detector (ID). Muons can also be reconstructed using only MS or ID information, depending on their kinematic properties and specific analysis requirements. Four types of muons can be selected depending on which detector information is used:

- **Combined muons (CB)**: reconstructed by combining track segments from both the inner detector (ID) and the muon spectrometer (MS). CB muons provide the most precise measure of momentum, since they exploit information from both systems.

- **Segment-tagged muons (ST)**:Muons are identified using reconstructed track segments in the EM that correlate with identification tracks. This method is useful for detecting muons where EM coverage is limited or incomplete.

- **Calorimeter-tagged muons (CT)**:Muons are reconstructed using calorimeter energy deposits corresponding to a minimum ionizing particle. CT are generally used for low momentum muons which don't leave sufficient tracks in the MS.

- **Extrapolated (Standalone) muons (ME)**:These are reconstructed purely using MS information with no correspondence to ID tracks. ME muons are especially useful for high pseudorapidity regions with reduced ID coverage.

Combining these strategies guarantees full coverage of all pseudorapidity regions and momentum ranges, making ATLAS very efficient at muon reconstruction.

3.3.4 Muons Identification

After reconstruction, muons are identified based on the quality of their tracks, their coherence with the origin of the primary vertex and their isolation from other particles in the event. As with electron identification, ATLAS uses Loose, Medium and Tight selection criteria to balance signal efficiency and background rejection:

- **Loose**:This selection aims to maximize efficiency while applying minimum requirements for track quality and isolation. Loose muons include all reconstructed muon types (CB, ST, CT and ME), guaranteeing wide coverage while allowing a higher background contamination.

- **Medium**: The Medium selection combines efficiency and purity, with much stricter track requirements than the Loose selection. It mainly uses CB and ST muons, and imposes less restricting isolation criteria to reject background jets.

- **Tight**: The Tight selection favors purity over efficiency by applying tight track quality, impact parameter, and isolation requirements. It mainly uses CB muons with additional requirements such as a reduced normalized χ^2 on the combined track fit (< 8), stricter match between momentum ID and MS measurements, and more rigorous isolation criteria.

- **High$-\mathbf{p_T}$**: Only CB muons satisfying the medium identification criteria and passed all three precision layers are included. This selection enhances the muon momentum resolution for muons with $p_T > 200$GeV.

Figure 3.5 performance evaluation reveals key characteristics: prompt muons show high efficiencies ($> 95\%$) for all selections within $\eta| < 2.5$, and Tight selections significantly reduce hadron misidentification (below 0.5%).

3.4 Jets

Quarks are constrained by QCD to exist in color-singlet combinations, which limits their free propagation. These quarks are often produced in pp collisions at the LHC, and their confinement results a shower of secondary quarks and gluons. This shower is then followed by hadronization, leading to the creation of color-neutral hadrons, mainly pions, with some contributions from kaons and light baryons.

High-momentum showers are subjected to relative stimulation, forming tightly-clustered jets. They then deposit their energy in the calorimeters, leaving tracks in the ID. Reconstruction algorithms combine the information collected by these detectors to reconstruct the energy and trajectory of the particle produced at the center. The following subsections describe the jet reconstruction algorithms and the different types of jet used in ATLAS analyses.

3.4.1 Jet Reconstruction Algorithms

The reconstruction of jets in ATLAS is performed using clustering algorithms that combine energy deposits from calorimeters and jet tracks. Most widely used is the

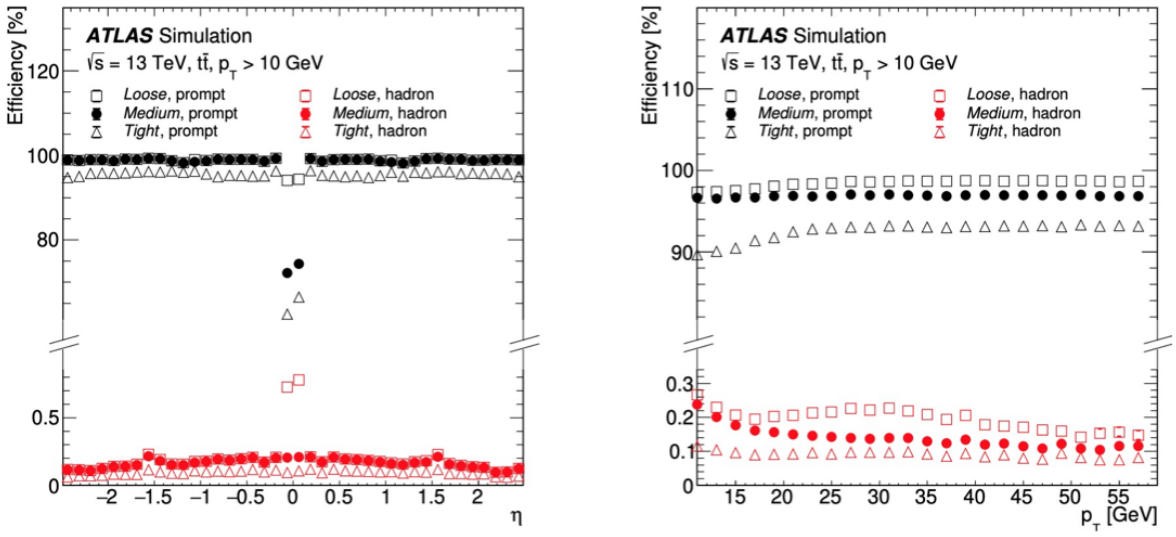


Figure 3.4: Muon-identification efficiency, as a function of η (left) and p_{T} (right), for three different selections (`Loose`, `Medium`, and `Tight`) WPs requirements in simulated $t\bar{t}$ events, shown separately for prompt muons and muons from light hadron decays [60].

anti-k_t algorithm [61], employs a sequential recombination algorithm which regroups jets according to their relative distance (d_{ij}) in η–ϕ space. For each jet candidate i, a distance (d_{iB}) is calculated from the beam. Both d_{ij} and d_{iB} are defined as follows:

$$d_{ij} = \min\left(\frac{1}{p_{T,i}^2}, \frac{1}{p_{T,j}^2}\right)\frac{(\eta_i - \eta_j)^2 + (\phi_i - \phi_j)^2}{R^2}, \quad d_{iB} = p_{T,i}^{-2} \tag{3.3}$$

Here:

- $p_{T,i}$ and $p_{T,j}$ represent the transverse momenta of particles i and j.
- η_i and η_j are their pseudo–rapidities.
- ϕ_i and ϕ_j are their azimuthal angles.
- R is the jet radius parameter that defines the size of the jet cone in the detector.

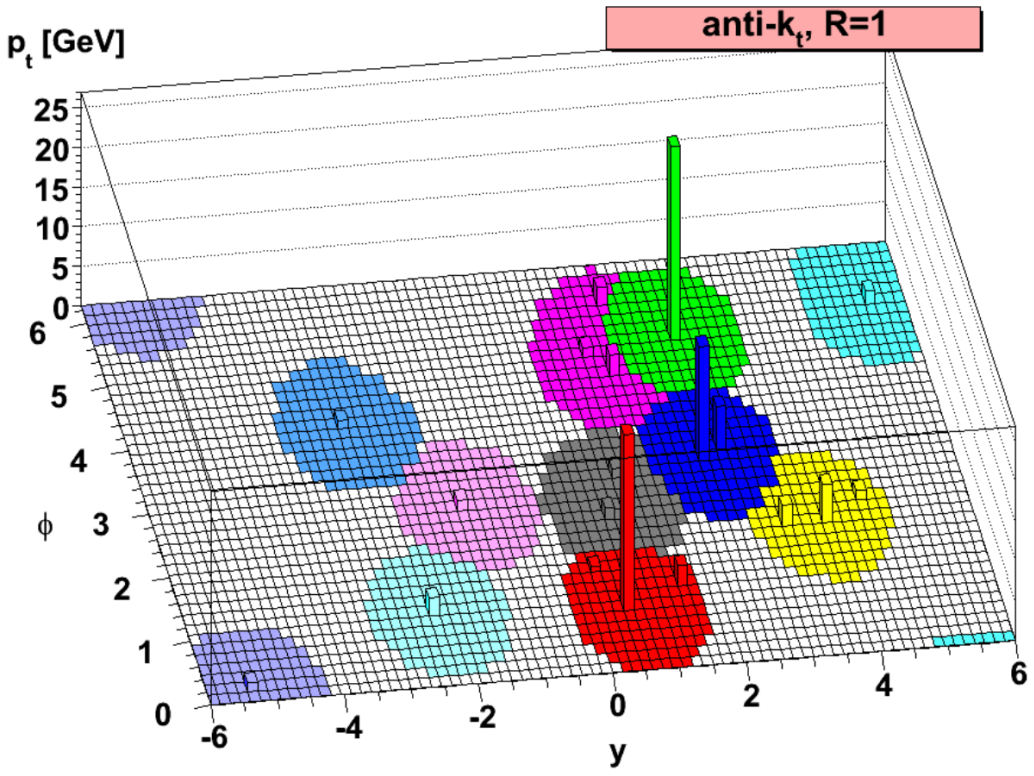


Figure 3.5: Illustration of the anti-k_t algorithm [62].

3.4.2 Small-R jets

Small-R jets are reconstructed using the anti-k_t algorithm with radius R=0.4, the most common choice for jets in ATLAS [63]. This small radius enables precise measurements of jet kinematics (p_T, η, ...), ideal for resolving close jets in high-multiplicity environments. The narrow cone minimizes soft radiation contamination, but makes them sensitive to pile-up effects in the high-luminosity conditions of the LHC. In order to eliminate piled-up jets, ATLAS applies the Jet Vertex Tagger (JVT) [64], a multivariate discriminant combining the Jet Vertex Fraction (JVF) - the fraction of the jet's pT track associated with the primary vertex - and the track's impact parameter compatibility. For jets with pT¡120 GeVpT¡120 GeV, the average JVT working point rejects 90% of pile-up jets while maintaining ¿90% efficiency for hard-scattering jets.
In addition to JVT, further enhancement is required to eliminate false jets from

non-collision backgrounds such as beam-induced background (BIB), cosmic rays and calorimeter noise [65]. To remove these poor-quality jets, ATLAS employs a set of jet-cleaning cuts based on sensitive variables. The cuts include the energy fraction deposited in the ECAL versus the HCAL, the maximum energy fraction released in each calorimeter layer, the charged fraction and the signal shape in the LAr calorimeter. By combining these criteria, ATLAS ensures that only high-quality jets are selected for analysis, enhancing the purity of the jet sample and reducing background contamination.

3.4.3 Large-R jets

Large-R jets, typically reconstructed with a radius parameter of R=1.0 using the anti-k_t algorithm, are designed to capture the collimated decay products of boosted heavy particles such as W/Z bosons or top quarks. These jets are crucial for identifying and studying the substructure of high-momentum objects, where the decay products are merged into a single large jet. The use of large-R jets is essential in searches for new physics involving boosted objects, as they allow for the reconstruction of the mass and other substructure observables of the parent particle. However, large-R jets are more susceptible to pile-up effects due to their larger size, which can degrade jet mass resolution and other substructure quantities.
The use of large-R jets is vital in the search for new physics involving boosted objects, as they enable the mass and other observables of the parent particle's substructure to be reconstructed. However, they are more sensitive to pile-up due to their larger size, potentially reducing the resolution of jet mass and other substructure quantities. Techniques such as trimming [66], pruning and mass-drop filtering are used to reduce these effects by eliminating soft and large-angle radiation. The ATLAS detector's response to large R-jets is calibrated on-site with reference objects such as photons or Z-bosons, ensuring precise measurements of jet energy and mass.
Recent progress has included machine learning techniques, such as transformer networks, to enhance the calibration of large R jets, improving the estimation of transverse momentum and jet mass.

3.4.4 Track-Jets

Track jets are reconstructed by using only the ID, applying jet grouping algorithms such as the anti-k_t algorithm for charged particles coming from the hard scattering vertex. This provides better angular resolution and more sensitivity to charged particles, making it especially useful for b-tagging and studying jet properties in environments where calorimeter resolution is limited. Additional longitudinal impact parameter constraints ($|z_0 \sin(\theta)| < 3\ mm$) on the primary vertex reduce pile-up

contamination and enhance the selection of tracks from the hard scattering vertex. These jets are particularly useful for the identification of the flavor large-R jets in high-density environments, using FR or VR algorithms. This involves matching track jets to the large-R jet via the Ghost Association (GA) [67] procedure, creating replicas of the jet's constituents with the same η and ϕ but with insignificant energy. This makes it possible to determine whether the grand-R jet contains subjets from b-hadron decays, a process known as b-tagging.

3.5 Missing Transverse Momentum

Missing transverse momentum (E_T^{miss}) is a key observable in high-energy physics experiments such as ATLAS, where it provides evidence of invisible particles such as neutrinos, or hypothetical particles beyond the Standard Model as dark matter. The concept of E_T^{miss}) arises from the conservation of momentum, where any imbalance in the transverse plane indicates the presence of undetected particles.
Measuring E_T^{miss} requires calculating the negative vector sum of all visible transverse moments in the event. The missing transverse momentum, E_T^{miss}, consists of contributions from electrons, muons, photons, jets, plus a "soft term" that accounts for unassociated tracks and energy deposition. The soft term is crucial for mitigating pile-up effects and ensuring the measurement precision of $E_T^{textmiss}$.

Mathematically, E_T^{miss} is calculated as follows:

$$E_{x(y)}^{\text{miss}} = E_{x(y)}^{\text{miss},\mu} + E_{x(y)}^{\text{miss},e} + E_{x(y)}^{\text{miss},\gamma} + E_{x(y)}^{\text{miss},\tau} + E_{x(y)}^{\text{miss,jets}} + E_{x(y)}^{\text{miss,soft}} \tag{3.4}$$

Each term is the negative vector sum of the transverse moments and energy deposits associated with specific particle categories. The soft term, $E_{(x,y)}^{\text{miss,soft}}$, unidentified hard object signals, calculated as follows :

$$E_{x(y)}^{\text{miss,soft}} = -\left(\sum_{i\in\{\text{soft objects}\}} p_{x(y),i}\right) \tag{3.5}$$

These components yield the magnitude and azimuthal angle:

$$E_T^{\text{miss}} = |\vec{E}_T^{\text{miss}}| = \sqrt{(E_x^{\text{miss}})^2 + (E_y^{\text{miss}})^2} \tag{3.6}$$

$$\phi^{\text{miss}} = \tan^{-1}\left(\frac{E_y^{\text{miss}}}{E_x^{\text{miss}}}\right) \tag{3.7}$$

In order to mitigate the impact of pile-up on the soft term, ATLAS uses a track soft term (TST). This technique is based on tracks associated exclusively with the hard

scattering vertex (HS), effectively filtering the contributions of pile-up interactions. However, it's important to note that TST has a limitation: neutral particles are not taken into account. More sophisticated techniques, such as particle flow algorithms, are used to address this limitation.

3.5.1 Reconstruction of the Missing Transverse Momentum

E_T^{miss} reconstruction includes contributions from two main sources: the calibrated signals from physical objects and the soft event signals from charged particle tracks not associated with hard objects. All the physics objects need to satisfy specific selection criteria in order to achieve high reconstruction quality.
Electrons are reconstructed using ECAL shower characteristics with matching ID tracks [68]. They need to be identified in the $|\eta| < 2.47$ region (excluding the $1.37 < |\eta| < 1.52$ transition region), be calibrated to the electromagnetic scale, and pass the medium and loose isolation criteria [69] with $p_T > 10\ GeV$.
Photons are identified by the electromagnetic shower patterns in the calorimeters and selected using the Tight criteria [70]. Contributing photons need to have a $p_T > 25\ GeV$ and η between $|\eta| < 1.37$ or $1.52 < |\eta| < 2.37$ [68].
Hadronic-decay τ leptons with $p_T > 20$ GeV and $|\eta| < 1.37$ or $1.52 < |\eta| < 2.47$ are considered if they meet the medium quality selection [71]. not meeting these criteria can still contribute to E_T^{miss}if they meet the jet selection criteria.
Muon candidates are reconstructed using MS and ID tracks for ($|\eta| < 2.5$), with wide coverage ($(2.5 < |\eta| < 2.7)$) by using only MS track segments. The average muons with $p_T > 10\ GeV$ in $|\eta| < 2.5$ contribute to the calculation of E_T^{miss} [72].
Jets are reconstructed using the anti-k_T algorithm with $R = 0.4$, by incorporating EM, jet energy scale, and stacking corrections. The soft term $E_T^{\text{miss,soft}}$ is derived from tracks with $p_T > 400\ MeV$ and $|\eta| < 2,5)$ that satisfy the quality criteria, with vertices formed using at least two traces with $|d_0| < 1.5\ mm$ and $|z_0 sin|\theta| < 1.5\ mm$.
The scale and resolution of E_T^{miss} are calibrated using $Z \to \mu^+\mu^-$, where muons (as minimal ionizing particles) are the ideal control sample, with no missing momentum. For calibration purposes, the leading and sub-leading muons must have energies of $p_T > 25\ GeV$ and $p_T > 20\ GeV$ respectively, satisfy average quality criteria within a range of $\eta < 2.5$ [72], and meet isolation requirements.

3.5.2 E_T^{miss} Performance

E_T^{miss} performance is evaluated rigorously by using $Z \to \ell\ell$ events, which provide a clean signature with a high cross section and no genuine E_T^{miss}. This involves

projecting the $\vec{E}_T^{\text{miss}}$ vector onto the reconstructed flight direction of the Z boson to evaluate detector resolution and systematic biases.
The mean value of this projection, noted $\langle E_T^{miss} \cdot A_Z \rangle$, serves as a metric for the E_T^{miss} scale, particularly its sensitivity to the balance between leptons and hadronic recoil. In events with no real missing energy, this value should theoretically be zero. Any deviations indicate a potential calibration error in the detector response or in the reconstruction algorithms.
The ETmissETmiss amplitude distribution in $Z + jet$ events demonstrates excellent agreement between data and simulation, typically deviating by 10-20% across the entire energy spectrum, as shown in Figure 3.6. This confirms the reliability of the ETmissETmiss reconstruction methodology implemented in the ATLAS experiment for physics analyses.

3.6 Overlap Removal

The reconstruction algorithms outlined in the previous sections function independently of each other for the most part. This may lead to the same physical object being reconstructed by several algorithms, resulting an ambiguities that need to be addressed before proceeding with the physical analysis. For example, electron candidates often leave energy deposits in calorimeters that are also reconstructed as jets, while muons can be found in or near jets from heavy-flavor semi-leptonic decays. To solve such ambiguities, a so-called overlap removal procedure is used to ensure that each detector signature is linked to a single reconstructed physical object. The overlap removal in ATLAS follows a hierarchical approach based on the resolution and identification efficiency of the various object types. Standard procedure involves applying a sequence of geometrical requirements based on the angular distance $\Delta R = \sqrt{(\Delta\eta)^2 + (\Delta\phi)^2}$ between objects, with varying thresholds according to the object types concerned. Typically, the sequence for eliminating overlap in ATLAS analyses is as follows:

- **Electron-Electron Overlap**: When two electrons share the same track, the one with the lowest p_T is eliminated.
- **Electron-Muon Overlap**: Electrons sharing a track with muons are removed, as this is probably due to photon radiation from the muon.
- **Electron-Jet Overlap**: Jets within $\Delta R < 0.2$ from an electron are removed, as it is probably electron energy deposits reconstructed as jets. Subsequently, electrons within $\Delta R < 0.4$ from any remaining jet are removed to eliminate heavy-flavored semi-leptonic decays.

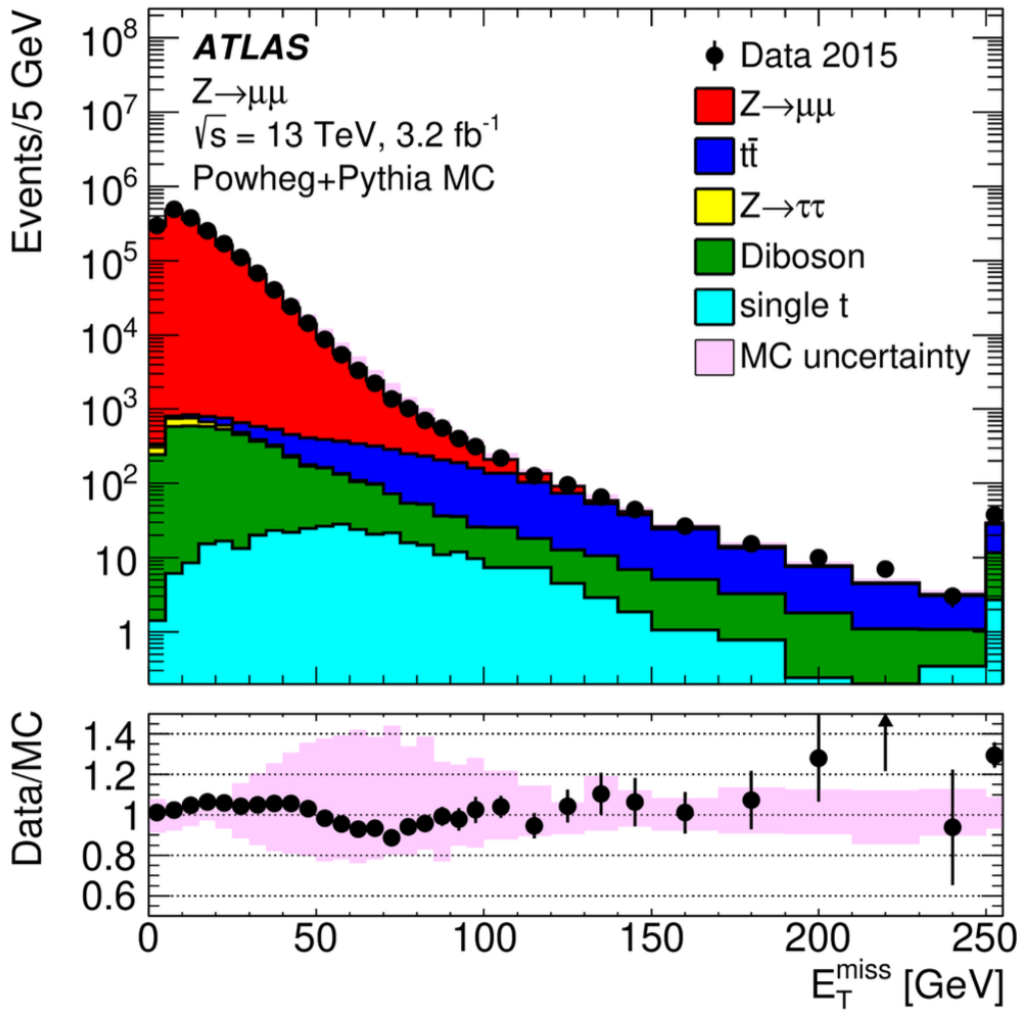


Figure 3.6: E_T^{miss} distribution comparison in $Z + jet$ events where no genuine E_T^{miss} is expected due to neutrino non-reconstruction [72].

- **Muon-Jet Overlap**: Muons with $p_T < 50$ GeV that are within $\Delta R < 0.4$ of a jet are removed if the jet has more than two associated tracks, signaling that the muon probably originates from a heavy-flavor decay within the jet. For muons with $p_T > 50$ GeV, a variable-radius criterion is often applied: $\Delta R < 0.04 + 10\ \text{GeV}/p_T(\mu)$.

- **Tau-Electron/Muon Overlap**: Tau candidates situated within

$\Delta\ R\ <\ 0.2$ from electrons or muons are removed to avoid leptons misidentification.

4

Jet Energy Scale and Resolution in the High Granularity Timing Detector

Within the challenging environment of the High-Luminosity Large Hadron Collider (HL-LHC). The physics motivation for the HGTD stems from the need to mitigate the effects of increased pileup, which degrades jet reconstruction performance, particularly in the forward region. The chapter outlines the HGTD layout, its core technology based on Low Gain Avalanche Detectors (LGADs), and the associated readout electronics. LGAD sensor performance, characterized through test beam studies involving devices from various vendors, is presented. Subsequently, the chapter investigates the HGTD's efficacy in suppressing pileup jets, enhancing jet energy response and resolution, and improving transverse momentum corrections. The analysis culminates in a comprehensive overview of the achieved results, demonstrating the HGTD's critical contribution to maintaining accurate jet reconstruction capabilities under HL-LHC conditions.

4.1 Physics Motivation

The HL-LHC is scheduled to begin in 2027 and will deliver an integrated luminosity of up to 4000 fb^{-1} over approximately 10 years. The instant luminosity is expected to reach up to 7.5×10^{34} cm^{-2}s^{-1}, compared to the present value of 2×10^{34} cm^{-2}s^{-1}. An associated upgrade of the ATLAS detector is required before the beginning of this new phase to deal with the high-radiation environment and the large increase in the number of collisions per bunch crossing.
In the new HL-LHC conditions, pileup will be one of the biggest challenges. For the nominal operating scheme, the interaction region will have a Gaussian spread of 45 mm along beam axis 1 and a pileup of 200 simultaneous pp interactions on average ($\langle\mu\rangle = 200$), corresponding to an average interaction density of 1.8 collisions/mm, as shown in Figure 4.1(a), compared to the 0.24 collisions/mm of Run 2.

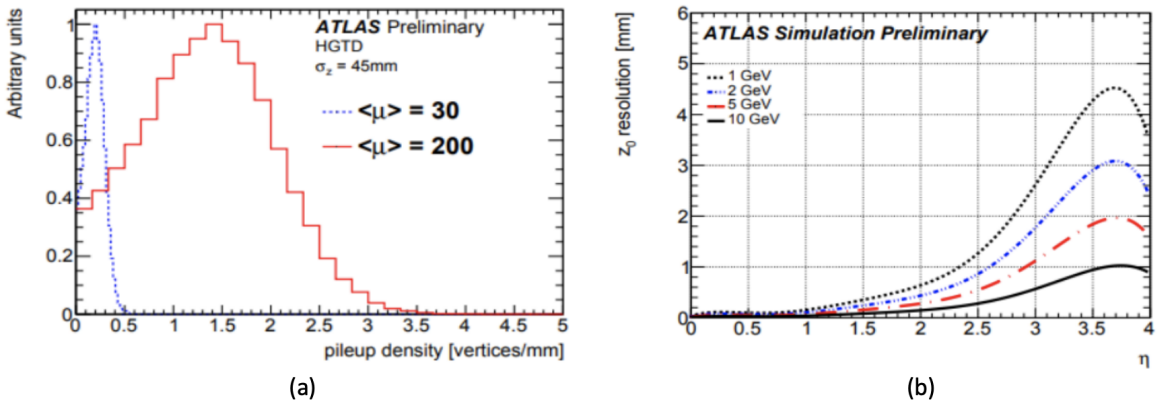


Figure 4.1: (a): Current and HL-LHC local pileup vertex density. (b): The resolution of the longitudinal track impact parameter, Z_0, as a function of η for different p_T values [73].

Under these conditions, a major challenge is to reject the charged particles generated by the pile-up. The resolution of the longitudinal trajectory impact parameter (Z_0) must be better than the average distance between interaction points (0.6 mm for HL-LHC). The Z_0 resolution is well below this limit in the central region, but becomes very large in the forward region, reaching up to 5 mm for particles with low p_T as seen in Figure 4.1(b). As a result, tracks can not be associated to the correct vertices in an unambiguous way, leading to reduced performance in terms of heavy flavour tagging, lepton isolation and the identification of jets originating from pileup

interactions.

4.2 High Granularity Timing Detector

A powerful new way to address the challenging pileup conditions of HL-LHC is by imploying the time spread of the different interactions during a single beam crossing. Figure 4.2 illustrates the time spread with an RMS of 180 *ps*. The position and time of the interaction points during a single cluster crossing are shown. Dotted lines represent the positions of the reconstructed vertices in the ITk . Since the time and position of the interaction are uncorrelated, if it is possible to measure the time of the traces from a vertex with enough accuracy, it's miles feasible to determine whether they originate from different interactions or a single interaction.

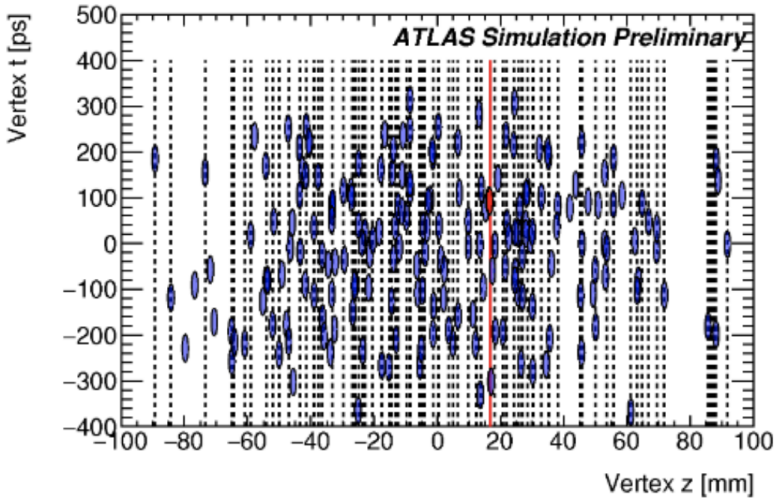


Figure 4.2: Position and time of the interaction points during a single bunch crossing $< \mu >= 200$ [6].

In Figure 4.2 the red point represent the signal interaction, at the same position there are also other pileup interactions, but the timing information separates these interactions.
In this context, the High Granularity Time Detector (HGTD) is introduced, to augment the new all-silicon Iner Tracker in the forward region. Offering a time resolution of 30 ps in the forward region, this detector will be able to reject stacks from $|\eta| = 2.4$ up to $|\eta| = 4$. More generally, this detector will improve the performance of the ATLAS detector in the forward region to a level similar to that of the central region

and will provide a powerful tool for luminosity measurements.

4.3 Detector Description

The HGTD is a state-of-the-art sub-detector scheduled for installation as part of the ATLAS Phase II upgrade, coinciding with the start of operation of the HL-LHC in 2029. Designed to address the challenges posed by the HL-LHC's significantly higher luminosity and increased collision rates, the HGTD will provide precise temporal measurements to mitigate pile-up effects.

4.3.1 Detector Design

The HGTD consists of two circular disks placed in between the ID and the end cap of the calorimeter at $z = \pm 3.5$ m with an active area at
$120mm < R < 640mm$, corresponding to $2.4 < |\eta| < 4$ as shown in Figure 4.3. The space allocated to the HGTD for ATLAS HL-LHC upgrade is quite limited, which defines some of the HGTD geometrical parameters, its thickness should not exceed 125 mm including 50 mm of moderator to protect the ITk and the HGTD from back-scattered neutrons. In order to ensure a timing resolution of 30 ps per track over all the HL-LHC, two layers of active sensors will be built with an additional effective layer at low radius. This additional effective layer will be achieved by increasing the overlap of the modules for $R < 320mm$ from 20% to 80%.

The active zone has a total of 8032 modules, each module comprising two sensors glued to two ASICs (application-specific integrated circuits). Each module holds an array of 30 × 15 pads with a total area of 4×2 cm24×2cm2. The dimensions of each pad are 1.3×1.3 mm21.3×1.3mm2 , identical for all HGTD modules. Each module, as shown in Figure 4.4, is bonded to a small flexible cable PCB, known as a flex module, connecting the ASIC signals and high voltage by wire bonding. The flex module is connected to a long flex cable via a mini-connector for the high voltage and a separate connector for signal transmission to the PEBs. The read out arrays are composed of modules with flexible cables that lead them to the detector's peripheral electronics. These rows are arranged linearly from lower to upper radii. The arrangement of the first and second layers is illustrated by rectangles.The arrangement of the first and second layers is shown as rectangles in figure 4.5. In particular, Figure 4.5(a) illustrates the first layer geometry, while Figure 4.5(b) shows the second one. Both the first and second layers mirror each other. In order to reduce dead zones and optimize coverage, each layer is rotated in opposite directions by 15 to 20 degrees. The baseline angle of 20 degrees rotation between disks is illustrated in Figure 4.5(c).

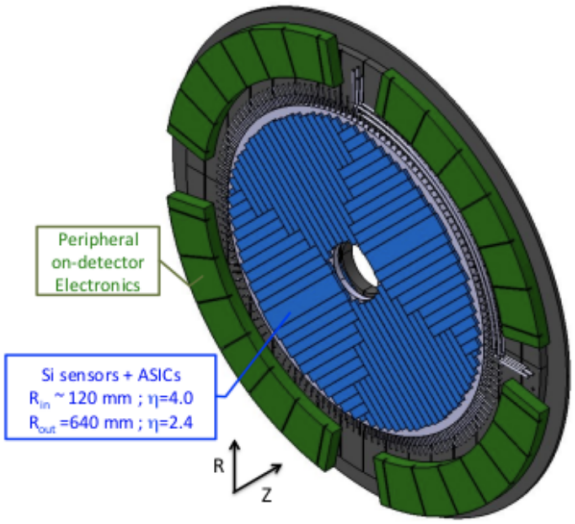


Figure 4.3: Illustration of the HGTD.The blue represent the active region and the green the off detector electronic [74].

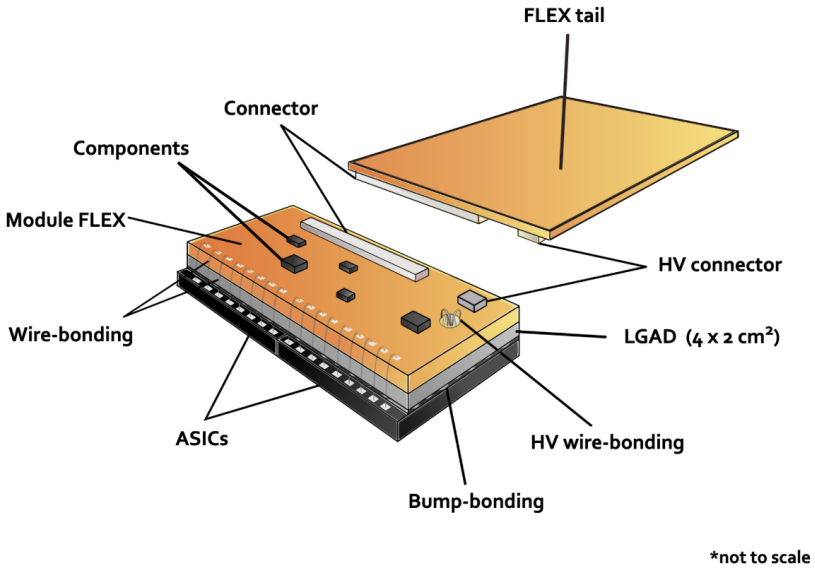
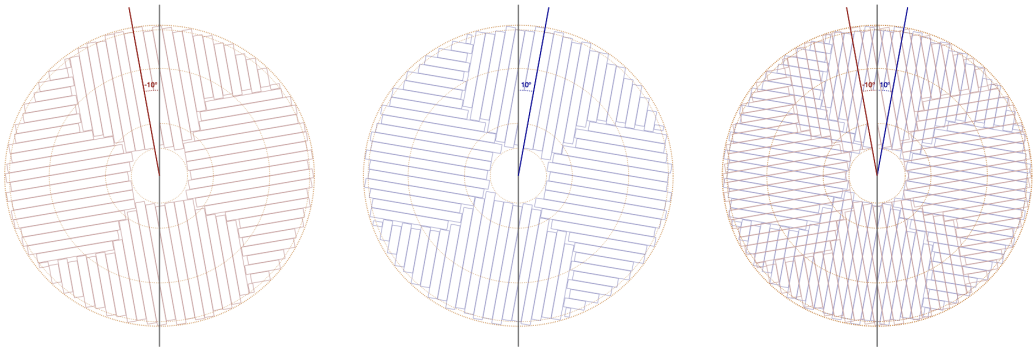


Figure 4.4: The HGTD hybrid module with its associated flexible reading cable tail [74].

In order to ensure that the HGTD provides the required time resolution indepen-



(a) First layer (b) Second layer (c) Overlay

Figure 4.5: The orientation of the readout rows for the first and second layer encountered by a particle, separately and with the overlay of both. Each layer is rotated in alternating directions by 20° . In the figures the staves of the three rings are separated by the circular lines [74].

dently of pseudo-rapidity, the modules with sensors and on-detector electronics are positioned on both sides of a cooling disk. Figure 4.6 shows the overlapping arrangement of the modules on either side of the disk, with the full simulation to optimize the overlap between the modules in three rings to achieve the desired temporal resolution. The overlap is 20%for $r > 470\ mm$, 54% for $230\ mm < r < 470\ mm$ and 70% for $r < 230\ mm$.

4.3.2 LGAD sensors

Low-Gain Avalanche Detector technology is the keystone of the HGTD in the ATLAS Phase II upgrade. LGAD sensors are dedicated silicon detectors, developed to offer precise time resolution, high granularity and high radiation resistance, ideal for the challenging environment of the HL-LHC. These sensors allow the HGTD to reach a time resolution of 30 ps to 50 ps per track, which is crucial for vertices that are close in space but distant in time, enhancing pile-up attenuation and reconstruction performance. LGAD sensors are made up of planar n-on-p silicon detectors,as shown in Figure 4.7a, with an extra, p-type, highly doped layer, called the gain layer. This layer improves the internal electric field, allowing impact ionization and signal amplification by minimum ionizing particles (MIPs). When an external bias voltage is applied, the polarity of the p-n junction is reversed, creating a large depletion region in the sensor mass.

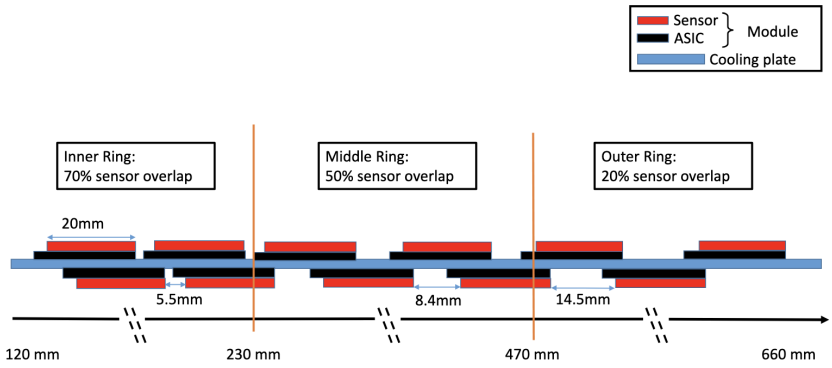


Figure 4.6: The schematic drawing shows the overlap between the modules on the front and back of the cooling disk. There is a sensor overlap of 20% for $r > 470mm$, 54% for $230mm < r < 470mm$ and 70 % for $r < 230mm$ [74].

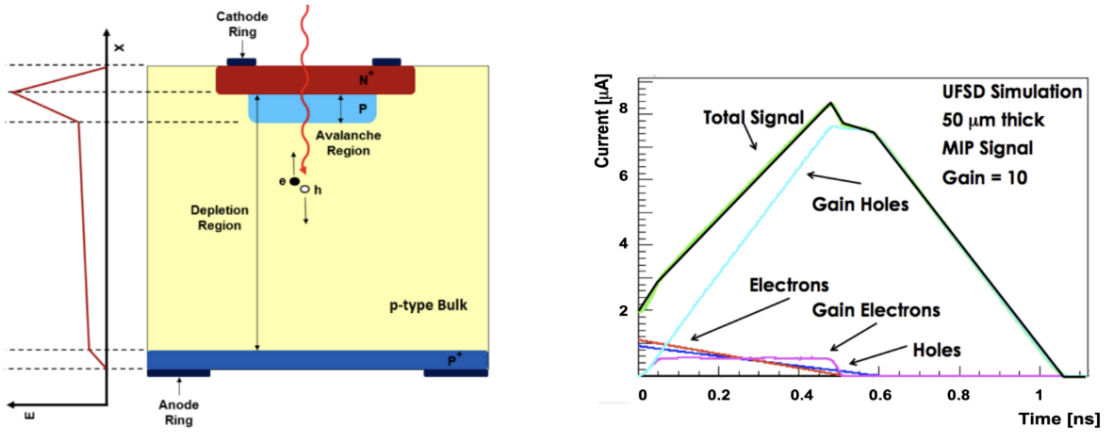
When a charged particle crosses the LGAD sensor, it generates electron-hole pairs by ionization. Influenced by the electric field applied :

- Electrons shift towards the n++ cathode..
- Holes migrate to the anode p++.

When electrons are close to the n+ junction, they encounter the amplified electric field created by the gain layer. This field initiates a process known as impact ionization, whereby the new electrons create additional electron-hole pairs. Once created, the holes drift towards the p+ junction, increasing the number of electric charge carriers. This cascade effect is known as the avalanche phenomenon, and leads to a significant amplification of the initial signal.
This current is a combination of the contributions of the primary and avalanche-induced electron-hole pairs. This behaviour is illustrated as a function of time in figure 5.5b :

- Total currents induced by primary and avalanche carriers.
- the individual components contributing to the overall signal.

Such a design guarantees that LGAD sensors offer high timing resolution while maintaining robust performance in the high radiation conditions typical of HL-LHC operation. Several factors contribute significantly to the time resolution of LGAD



(a) (b)

Figure 4.7: (a) A diagram showing the cross-sectional view of an LGAD [74]. (b) A simulated current signal for an LGAD sensor measuring 50 m in thickness. [75].

sensors. These include time walk, resulting from signal amplitude variations, jitter, due to electronic noise in the sensor and readout electronics, and Landau fluctuations, arising from the non-uniformity of the charge deposition across the particle path through the sensor. In addition, resolution is affected by the size of the time-to-digital converter (TDC) and the accuracy of the electronic clock employed in the system. The total time resolution (σ^2) is expressed as the sum squared of these individual components:

$$\sigma^2 = \sigma^2_{TimeWalk} + \sigma^2_{Landau} + \sigma^2_{Jitter} + \sigma^2_{TDC} + \sigma^2_{Clock} \tag{4.1}$$

This equation illustrates how each factor contributes to the resulting timing measurement. LGAD sensors designed for HGTD should collect a minimal charge of 4 fC and reach a time resolution of at least 35 ps per shot early in the operation, degrading to 70 ps at the end of the detector's lifetime. Several manufacturers, including CNM (Spain), HPK (Japan), FBK (Italy), NDL (China) and IME (China), have been involved in the *RD* of these sensors, testing different doping levels, active thicknesses, wafer sizes and inter-wafer spacings. Further research and development of HGTD sensors is continuing in order to optimize their performance and resistance to radiation.

4.3.3 Front-end Electronics

Front-end electronics design is fundamental to obtaining optimum time performance from LGAD sensors. The electronics influence the overall time resolution. The main contribution of electronics to time resolution comes from jitter and time march. where the Jitter is directly linked to the design of the front-end analog electronics, which consists of a voltage preamplifier plus a fast discriminator. This contribution can be expressed as follows:

$$\sigma^2_{\text{elec}} = \sigma^2_{\text{jitter}} + \sigma^2_{\text{TimeWalk}} + \sigma^2_{\text{TDC}}, \tag{4.2}$$

where σ_{jitter} refers to the time-to-digital converter (TDC) contribution, resulting from the time digitization error created by TDC circuit samples.
The FE configuration consists of a sensor, then an amplifier which amplifies the measured signal from the sensor. Amplified signal from the oscillator is processed into an analog time measurement by a discriminator circuit. Lastly, the signal is digitized using two TDCs and then stored in a local memory at channel level.
ALTIROC's ASIC, based on 130 nm TSMC CMOS technology, can handle up to 4 MGy of TID radiation. Similar to pixel detectors, the ALTIROC's architecture is characterized by a much reduced number of channels and a single-pixel front-end for optimal time measurement. The matrix comprises 15x15 channels, for a total of 225 channels, which are arranged in columns for reading, using common digital electronics at the bottom. The single-channel readout unit, shown in figure 5.8, is the core element of the ALTIROC ASIC architecture, replicated 225 times in the matrix. Each read out channel is in charge of preamplification, discrimination and digitization of the results, as well as local storage (buffer memory) of the digitized data until a L0/L1 trigger signal is received.
The preamplifier is designed using a cascaded common source configuration, made up of two transistors: an input transistor (M1) and a follower transistor (M2). This ensures high bandwidth and low-noise amplification of the sensor signal, essential for maintaining synchronization accuracy. Following the pre-amplification stage, a fast discriminator processes the amplified signal and determines the pulse timing by applying a fixed threshold. This threshold-based approach ensures accurate time-of-arrival (TOA) identification for each shot.
Two Time-to-Digital Converters (TDCs) manage the digitization process. One TDC digitizes the TOA on 7 bits, corresponding to the position of the rising edge of the discriminator output. This is done within a range of 2.5 ns, with a quantization step of 20 ps, ensuring minimal impact on time resolution. The second TDC digitizes

the discriminator output width on 9 bits, capturing the width of the discriminator output.

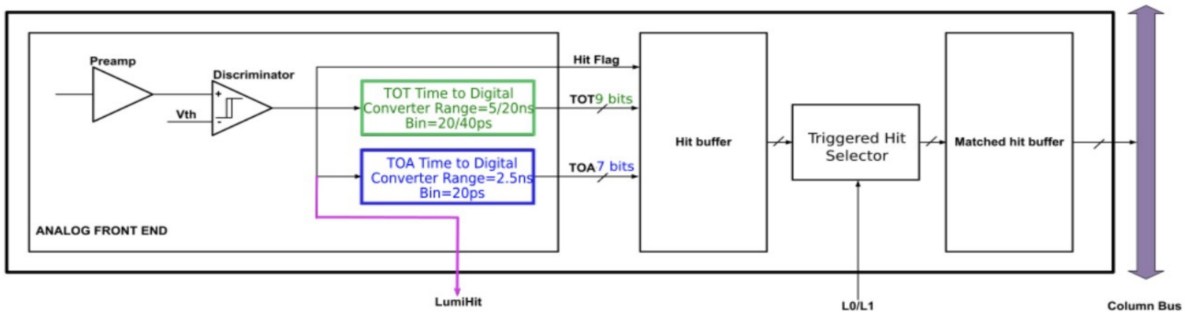


Figure 4.8: Schematic of a single pixel readout [76].

The analog front-end electronics of each channel play a major role in achieving low jitter. The sensor signal is first amplified by a voltage preamplifier which, considering the approximately 1 ns duration of the LGAD signal, needs a bandwidth of around 1 GHz. After the preamplifier, a fast discriminator is used. The discriminator's output edge, representing the time of arrival (TOA), triggers a time-to-digital converter (TDC) operating on a Vernier delay line configuration, with the clock providing the stop signal. This start-stop mechanism minimizes power consumption in the absence of hits. The quantization step size is 20 ps, which has minimal impact on overall time resolution. TOA measurements are limited to a 2.5 ns window centered on the cluster. The precision time measurement capability of the HGTD can be used to enhance considerably the reconstruction of different physics objects. This can be accomplished by rejecting out-of-time pileup that could contaminate objects thus reducing their reconstruction efficiency. This is particularly relevant given that pileup jets can reduce the accuracy of Standard Model measurements and the sensitivity to the discovery of new physics.

4.4 Physics Prospects

4.4.1 Suppression of pileup jets

Pileup is very crucial for the reconstruction and identification of objects at the HL-LHC. In the case of jets, pileup can affect the reconstruction in a different ways. as shown in Figure 4.9, one is that particles from a pileup interaction can infect a jet from hard scatter and change its reconstructed energy. modify its reconstructed energy. Pure pileup jets from an interaction other than hard scatter can also be

created, due to a QCD process during the pileup interaction, more likely at high p_T, or because of a random combination of particles from different interactions, more likely at low p_T.

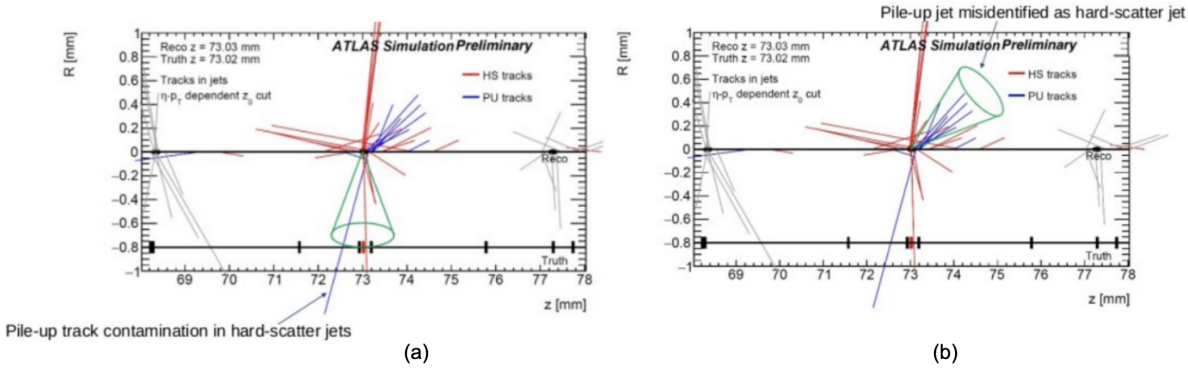


Figure 4.9: All tracks associated with primary vertices illustrating the PU contamination [6].

A key element for the rejection of pileup jets is the association of the jets tracks with the primary vertices. A simple but powerful discriminant is the R_{pT} jet variable, defined as the scalar sum of the p_T of all tracks that are inside the jet cone and originate from the hard-scatter vertex PV_0, divided by the fully calibrated jet p_T, i.e.,

$$R_{pT} = \frac{\sum p_T^{trk}(PV_0)}{p_T^{jet}} \tag{4.3}$$

This variable should be large for the hard scatter jets and low for pileup ones. Unfortunately in high pileup environment and especially in the forward region it is possible to have pileup vertices that appear to be merged with the hard scatter vertex. In that case the discriminating power of this variable is greatly reduced. Detailed simulations of jet events are being used to evaluate the performance of the HGTD in suppressing pile-up jets. These simulations integrate realistic detector models and consider the pile-up conditions expected at the HL-LHC. The results of the simulations provide valuable indications on the optimization of jet reconstruction algorithms and on the overall effectiveness of HGTD in reducing the impact of pile-up on jet physics analyses. Enhanced suppression of pile-up jets results directly in cleaner event topologies, reduced systematic uncertainties and increased sensitivity to a wide range of physical processes.

4.4.2 Jet Energy Response and Resolution

Beyond the suppression of pile-up jets, HGTD also focuses on improving the energy response and resolution of jets, which are essential parameters for accurate jet reconstruction and calibration.

4.4.3 Jet Energy Response

The jet energy response is defined as the ratio of calorimeter jet ($p_{T_{reco}}$) to the truth-jet ($p_{T_{truth}}$) energies. The mean of the estimated JER is determined using the Gaussian fit of the the distribution $p_{T_{reco}}/p_{T_{truth}}$, where $p_{T_{reco}}$ stand for the transverse momentum of the reconstructed calorimeter jet and $p_{T_{truth}}$ is the transverse momentum of the jet reconstructed from all the generated stable particles (excluding neutrinos), this jet energy response is represented in Figure 4.10a, as a functioon of $\eta|$ and in in Figure 4.10b, as a function of p_T .

In an ideal scenario, the jet energy response should approach unity, indicating that

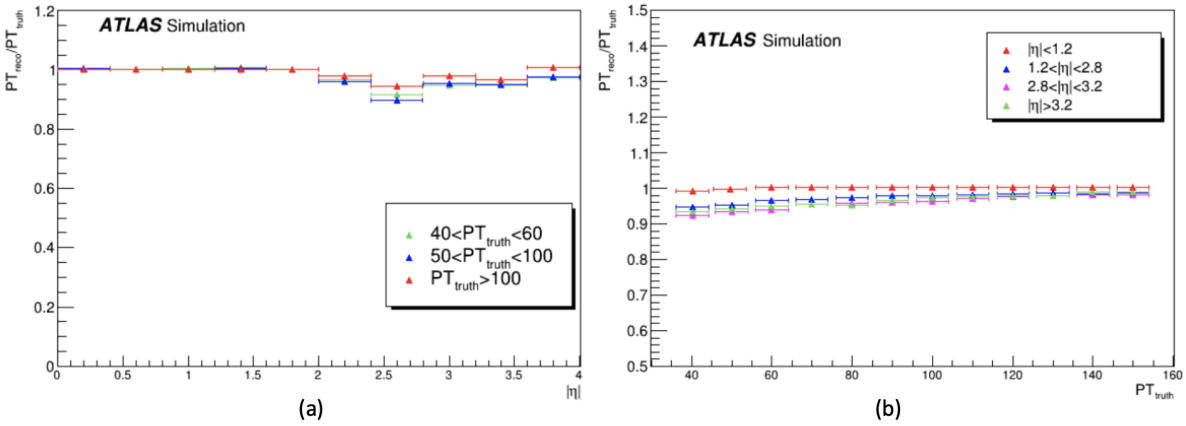


Figure 4.10: (a) show JER as a function of η and as a function of $p_{T_{truth}}$ is illustrated in (b), for raw calorimeter jets [6].

the measured jet energy accurately reflects the actual jet energy. However, different factors can affect the jet energy response, including calorimeter non-uniformities, energy losses in the detector material, pile-up contamination and detector resolution effects. HGTD specifically aims to mitigate pile-up contamination, as it can significantly distort the measured jet energy.

HGTD's precise temporal information mitigates the impact of pile-up on jet energy measurements, resulting in a more accurate and consistent jet energy response. By

assigning precise time stamps to the trajectories of charged particles, HGTD identifies and eliminates pile-up trajectories that contribute to the measured jet energy.

4.4.4 Jet Energy Resolution

Jet energy resolution is the precision measurement of jet energy by the detector. It is defined as the standard deviation of the jet energy response distribution. A high jet energy resolution, corresponding to a low standard deviation, indicates that jet energies can be measured with high accuracy. Conversely, low jet energy resolution implies greater uncertainty in jet energy measurements.
Basically, it is a measure of the detector's ability to resolve the difference in energy between two jets of similar total energy. The jet energy resolution is parameterized as follows:

$$\frac{\sigma(p_{T_{reco}}/p_{T_{truth}})}{\mu(p_{T_{reco}}/p_{T_{truth}})} \tag{4.4}$$

where σ and μ are evaluated from the Gaussian fit of the distribution $p_{T_{reco}}/p_{T_{truth}}$.

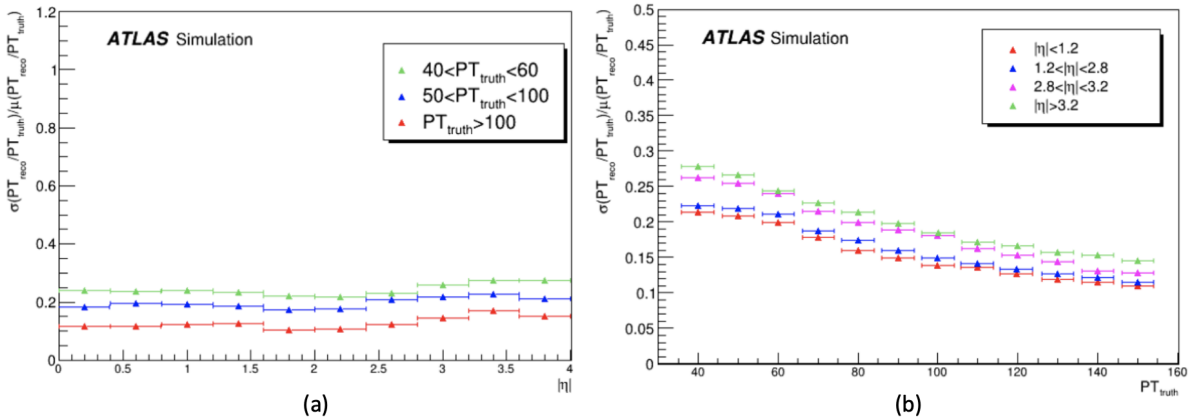


Figure 4.11: (a) show The transverse jet energy resolution as a function of η, and as a function of $p_{T_{truth}}$ is illustrated in (b), for raw calorimeter jets [6].

The comparison of the jet resolution for the various η and p_T bins is shown in Figure 4.11. A good resolution is seen in the central region of the detector, however it is reduced in the forward region for low p_T regime. This is due to the Pileup-Track contamination at the hard scatter jets.

4.4.5 Jet pT correction

The purpose of the Jet p_T correction is to remove the Pileup Track energy, from the hard scatter jet energy deposited in the detector and eventually reconstructed. The correction method consists in assigning tracks to primary vertices, a track is mapped to a vertex if its origin is geometrically compatible in the longitudinal trajectory impact parameter Z_{vtx} with the vertex position. This compatibility can be determined by the resolution on the track Z_0 impact parameter as follows:

$$\frac{Z_0 - Z_{vtx}}{\sigma} < 2 \tag{4.5}$$

The Jet p_T is improved by removing the E/P of this PU-track as follows:

$$p_{T_{Jet-corr}} = p_{T_{Jet}} - \sum E/P \cdot p_{T-PUTrack} \tag{4.6}$$

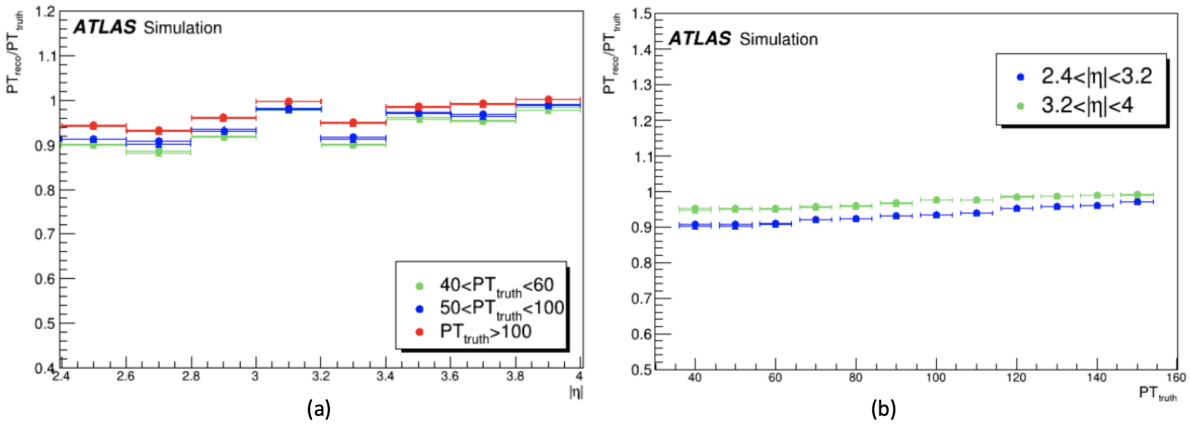


Figure 4.12: (a) show the JER as a function of η and as a function of $p_{T_{truth}}$ (b) before and after correction [6].

Figure 4.12 shows that the jet response remains unchanged, after applying the correction for different eta bins. The jet resolution has been improved by 3.5% and 1.78% for $40 < p_T < 60$ and $50 < p_T < 100$, respectively, as illustrated in Figure 4.13.

4.5 Results

The HGTD, with its impressive 30 *ps* timing resolution for minimum-ionizing particles, promises a significant leap in the ATLAS detector's capabilities within the

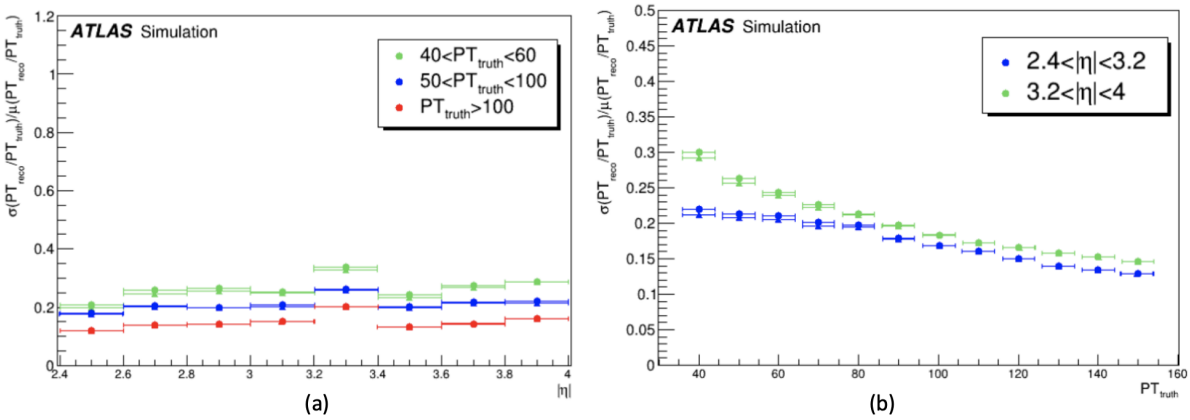


Figure 4.13: (a) show the transverse jet energy resolution as a function of η and as a function of $p_{T_{truth}}$ (b) before and after correction [6].

forward region ($2.4 < \eta < 4.0$). This precision provides a powerful means to combat the pervasive pileup challenge, allowing for the effective rejection of out-of-time contributions and subsequent improvements in the reconstruction of jets and other physics objects. By disentangling complex events, the HGTD paves the way for enhanced measurements of jet energy scale and resolution, crucial for various HL-LHC studies. As we transition towards even more sophisticated reconstruction techniques, it's important to consider how complementary detector upgrades, such as improvements to the Inner Tracker (ITk), will further enhance the overall performance of the ATLAS experiment in the high-pileup environment. The next chapter will detail how this tracker upgrade will improve track reconstruction.

5

Thermal Performance Study of the ATLAS ITk Strip Modules at BNL

With the performance of the High Granularity Time Detector (HGTD) having been considered in detail, we turn to the evaluation of the ATLAS Inner Tracker (ITk) strip modules. A thermal performance study carried out at BNL to guarantee the quality and reliability of these modules is detailed. Both methodology and results analysis are discussed, guaranteeing the effectiveness of these components in the ATLAS detector.

5.1 Introduction to ITk Strip Modules

The ATLAS ITk is the cornerstone of the HL-LHC upgrade. Designed to handle the increased collision rates and particle fluxes expected during this new phase of operation. Complementing the precise time measurements of the HGTD to mitigate pile-up effects, the ITk provides high-resolution spatial tracking throughout the detector volume thanks to its all silicon design. The ITk stripe detector, which features spans in the barrel region and petals in the cap, incorporates almost 18,000 radiation-resistant silicon modules. These modules undergo rigorous thermal performance studies at BNL, where they are thermally cycled repetitively between $-35°C$ and $+40°C$ to test their mechanical and electrical resistance under HL-LHC conditions. Key parameters include tracking rates, background radiation levels and signal-to-background ratios, ensuring operational stability in high-radiation environments with fluences of up to 1.2 times 10^{15} neq/cm^2. By maintaining precise resolution and minimizing channel loss, these studies ensure that the ITk strip detector can provide precise tracking data, crucial for pile-up mitigation and physics analysis during HL-LHC operation.

5.2 ITk Strip Detector: Staves, Petals, and Modules

ITk strip modules are an essential part of the tracking system, providing robust detection capabilities in the tracker barrel and end regions. These modules consist of silicon sensors combined with advanced readout electronics, assembled on thin mechanical supports to minimize hardware interactions. Their design emphasizes precision, radiation tolerance and efficient thermal management - key factors for reliable operation under HL-LHC conditions. Thermal performance is a critical factor for ITk strip modules, due to the high temperatures generated by dense electronic components during data acquisition at high intensities. Efficient cooling systems are needed to maintain sensor stability and avoid degradation over time.

5.2.1 ITk Strip Staves and Petals

The ITk strip detector's structural framework consists of staves in the barrel region and petals in the end cap regions. Staves are the linear structures that house the modules in the barrel region of the ITk strip detector. They are designed to ensure mechanical support and thermal control of the modules. Each stave contains 28 evenly distributed modules, 14 on each side, as shown in figure reffig:stave. mounted on a carbon fiber core. The carbon fiber core includes titanium cooling pipes embedded in a thermally conductive foam, enabling efficient heat transfer.

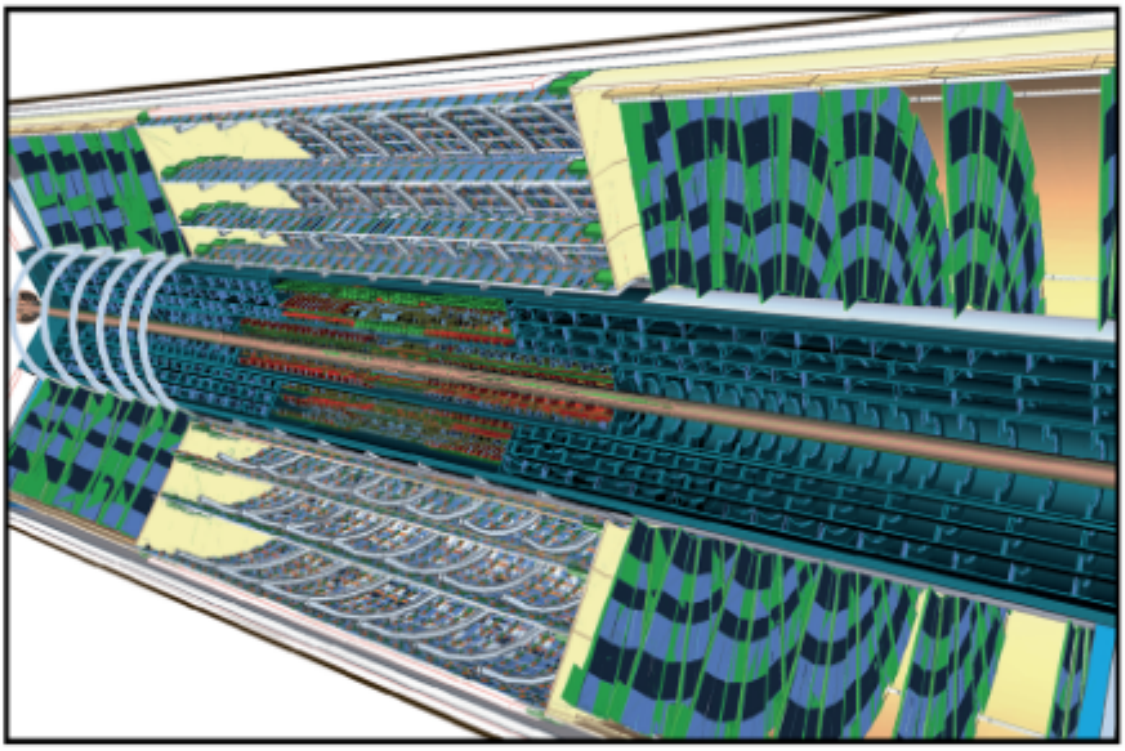


Figure 5.1: Layout of the ATLAS ITk detector.

This configuration is essential for maintaining the stability of the silicon sensors and readout electronics during operation.

In addition to thermal management, the staves also serve as conduits for the electrical and optical services crucial for the modules. These include data and power transmission, synchronization and data control. By integrating these services within the stave structure ensures that the modules receive the necessary resources for optimal performance. Staves are designed to conserve their structural integrity under a variety of environmental conditions, including temperature fluctuations and mechanical constraints. This ensures that modules remain securely fixed and aligned, which is essential for accurate particle tracking.
Petals, on the other hand, are the structure units found in the endcap areas of the ITk strip sensor. They are arranged in rings, designed to accommodate trapezoidal sensors that cover the disc-shaped endpieces. While the first three rings can be covered by a single sensor, the larger petals require two sensors due to their width.

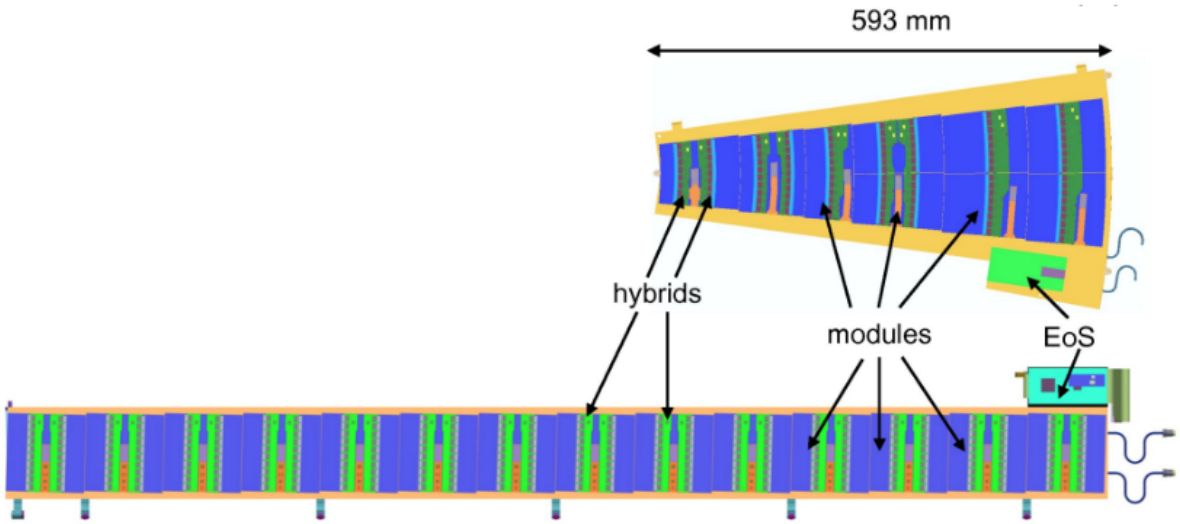


Figure 5.2: Sketch of barrel short strip stave.

This arrangement allows efficient coverage of the end-cap areas with minimal use of material. Like the staves, petals provide mechanical support for the modules, ensuring that they are securely mounted and aligned. An understanding of the design and functionality of the staves and petals provides an insight into how these components contribute to the ITk strip detector's ability to achieve high-resolution spatial tracking while maintaining thermal stability under the HL-LHC's demanding conditions.

5.2.2 ITk Strip Modules

ITk strip modules are the core functional units of the ITk strip detector, Figure refig:srip, designed to provide high-resolution spatial tracking in the barrel and endcap regions. Each module consists of one or two silicon sensors, up to four hybrids (containing readout ASICs) and a power board. Silicon sensors are characterized by n-type implantation strips on a p-type mass, with active thicknesses of around 300 m. Such a design guarantees radiation tolerance and reduces the material input to minimize multiple scattering effects, which is crucial for maintaining overall detector performance.

The individual module readout channels are AC-coupled to the n-type bands. The components of the ITk band detector include the sensor, one (for long bands, LS Figure 5.4a) or two (for short bands, SS Figure 5.4b), hybrid PCBs and a power supply board. The hybrid acts as a flexible PCB, accommodating the application-specific

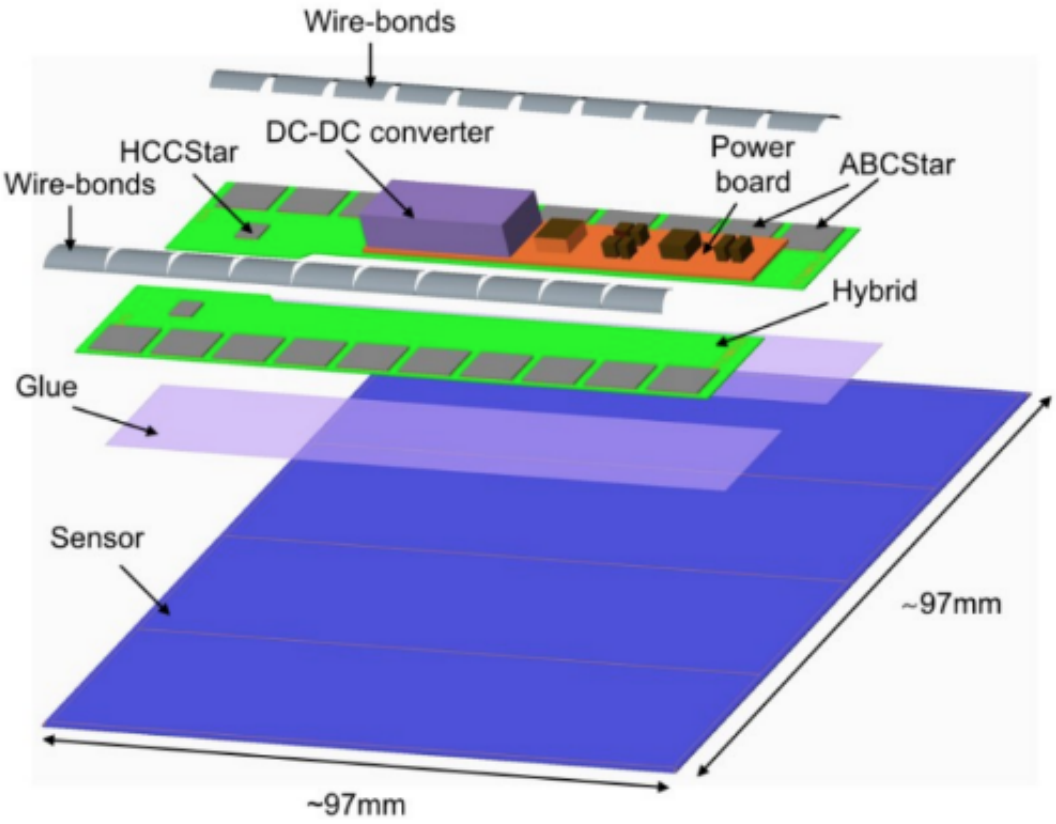
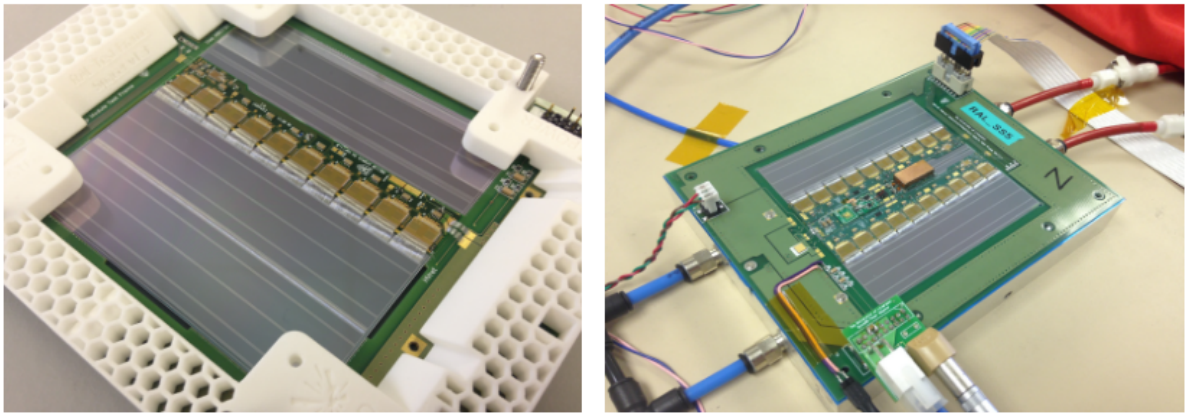


Figure 5.3: View of Short-Strip Module.

integrated circuits (ASICs) for reading, particularly the binary ATLAS (ABCStar) chips, attached to it [77]. ABCStar chips establish direct communication with an HCCStar. The interconnection of the individual channels in the ABCStar chips with the sensor strips is achieved by wire links. If a charged particle passes through the sensor, it generates a signal that is processed by the readout electronics. The process ensures precise particle tracking and essential to the ATLAS detector's capacity to perform precise reconstructions of particle trajectories.
The modules are glued to carbon fiber cores (in the barrel) or attached to petals (in the end caps), ensuring both mechanical stability and efficient thermal management. The readout electronics within the modules treat the signals from the silicon sensors, enabling precise particle tracking. The ITk strip system will comprise some 17,888 modules, underlining the complexity and scale of the detector. By integrating these

modules into the staves and petals, the ITk strip detector meets its objective of providing high-resolution spatial tracking over the entire detector volume.

Overall, the design and functionality of the ITk strip modules are critical to the



(a) (b)

Figure 5.4: Prototype modules of LS (a) and SS (b).

success of the ATLAS Inner Tracker detector. By combining sophisticated silicon sensors with advanced readout electronics, the modules guarantee that the detector can operate efficiently in the challenging conditions of the HL-LHC, providing accurate and reliable data for physics analyses.

The study examines how thermal cycling impacts the performance of electrical and cooling systems integrated within the staves, which are essential for support structures in the inner track and barrel region. It provides details of the experimental set-up used to monitor temperature and humidity in the cabinet, highlighting the importance of maintaining stave reliability in low-temperature conditions. Finally, it synthesizes the experimental results to give an overview of stave performance under such conditions.

5.3 Experimental Setup for Thermal Performance Study

Brookhaven National Laboratory (BNL) plays a leading role in the manufacture of the Strip detector, building half of the 392 staves required for operation. During the initial pre-production phase, meticulous assembly and testing procedures were implemented, in early 2022, one side of the Long Strip stave was built, while the

other was completed in May of the same year. To garanty the precision and reliability of these staves, a rigorous testing process was applied in a clean room dedicated at BNL. This clean room features a specialized coldbox designed to simulate the challenging conditions in which the staves will operate. In this coldbox, temperature and humidity levels are precisely controlled and meticulously monitored, as shown in Figure 5.5.
The testing set-up used in this study is strongly based on the cold box system. A cooling unit is incorporated to reduce the temperature of the stave under test effectively, mimicking the low-temperature environment of the detector. The pump improves global cooling efficiency, particulary for modules far from the stave, where uniform cooling can be more difficult. To monitor temperature variations within the system precisely, a TC08 data logger is used , this logger is connected to a thermocouple network placed at various locations to monitor temperatures on both the cooler pipes and at various points inside the coldbox. To monitor humidity levels, SHT85 sensors are installed inside the box. Ultimately, data from the various environmental sensors, including temperature and humidity readings, are collected and managed by a Raspberry Pi4 computer, contributing to the overall data collection and analysis process.

5.3.1 USB-TC08 Data Logger

The TC-08 USB, pictured in Figure 5.6a, is a high-tech data acquisition device designed to control up to eight thermocouples simultaneously via its eight input channels [78]. It is designed specifically to provide precise and efficient temperature monitoring over an extended range from -270°C to +1820°C, making it suitable for a variety of applications requiring precise thermal measurements. Exploiting the abilities of multiple thermocouple types, including B, E, J, K, N, R, S and T, users can select the most appropriate type for their specific temperature range requirements. Within the context of our study presented, Figure 5.6b illustrates the use of Type K thermocouples on account of their compatibility with the desired temperature range and their reliability in thermal test environments. Powered by a Broadcom BCM2711 quad-core Cortex-A72 processor clocked at 1.8 GHz, it is ideally suited to managing readings from environmental sensors and data loggers [79].
During thermal cycle testing, four thermocouples are employed to provide complete temperature monitoring throughout the process. Two are strategically placed on the cooler pipes to accurately measure surface temperatures. The remaining two are placed inside the cooler to measure internal temperature variations throughout the test. This arrangement enables detailed analysis of both external and internal thermal dynamics, guaranteeing effective monitoring.

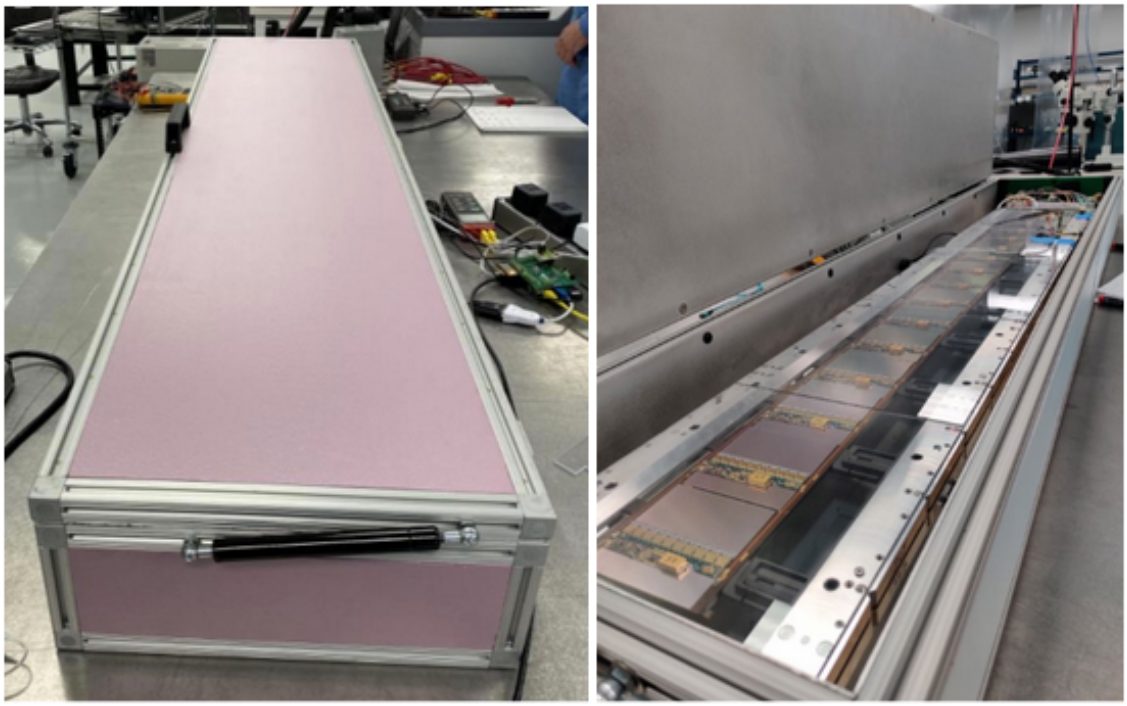


Figure 5.5: Coldbox (a) with a stave installed inside (b).

5.3.2 SHT85 sensor

The SHT85 sensor [80], shown in Figure 5.7, is a meticulously designed precision instrument for accurate humidity and temperature measurements in challenging environments and testing conditions. Its pin-type connector allows simple integration and replacement, making it a convenient option for a variety of applications. The sensor's high reliability and long-lasting stability make it a preferred choice for severe test scenarios where performance consistency is crucial.
While the SHT85 performs optimally in a temperature range from 20°C to 50°C, the measurements taken during the stave thermal cycle test depend solely on the data logger due to the expected lower temperatures. However, the SHT85's capabilities have been fully utilized for humidity measurements in the cold box. In this study, two SHT85 sensors are strategically positioned inside the cold box to measure humidity levels precisely, exploiting the sensitivity and precision of the sensor

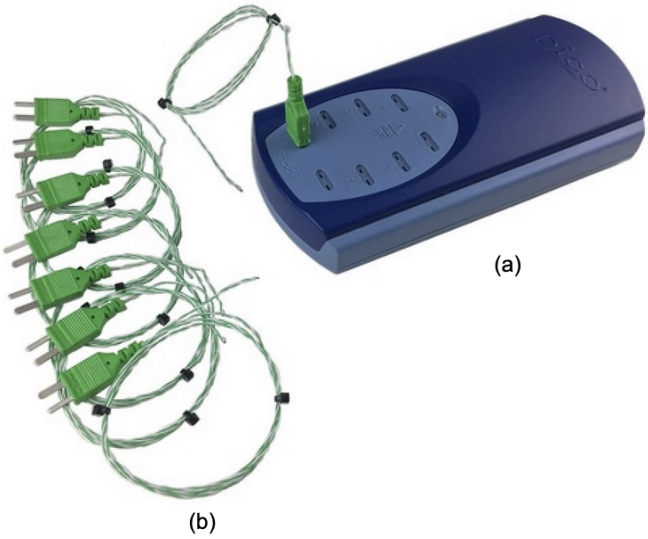


Figure 5.6: USB TC-08 data logger (a) with Type K thermocouple (b).

for accurate measurements throughout the test process. This configuration ensures that humidity levels are meticulously monitored and controlled, contributing to the overall success of thermal cycle testing. By focusing on humidity measurements, the SHT85 provides valuable data to complement the temperature readings of the data logger.

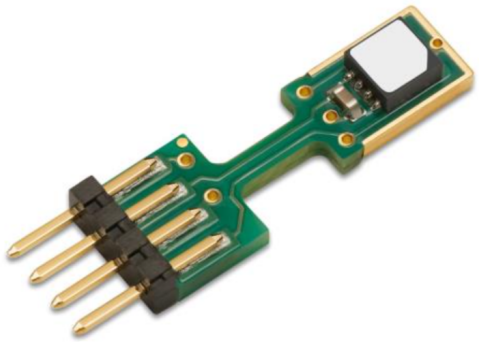


Figure 5.7: USB TC-08 data logger (a) with Type K thermocouple (b).

5.3.3 Raspberry Pi4:

In the experimental set-up, the Raspberry *Pi*4 [81], as shown in Figure5.8 and in the larger system diagram in Figure 5.9, performs a key role as an adaptable and low-cost single-board computer, with the ability to develop programming skills, to support hardware projects, enable advanced automation and stretch its functionality to industrial applications. Running under the Linux operating system, it has a range of unique functions centered on its GPIO (General Purpose Input/Output) pins enabling operators to monitor components for physical computing projects and explore the Internet of Things (IoT).. Powered by a Broadcom BCM2711 quad-core Cortex-A72 processor running at 1.8 GHz, it is perfectly suited to managing data from environmental sensors and data loggers.

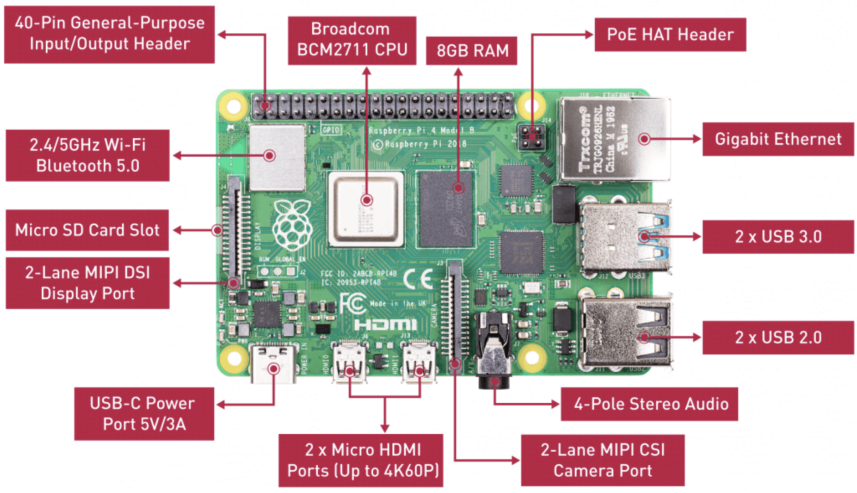


Figure 5.8: A peripheral interface overview of the Raspberry Pi4.

In the context of the study described, the Raspberry *Pi*4 serves as the central processing unit for both environmental sensors and data logger readouts. With its computing capabilities and GPIO pins, it proves essential for orchestrating the data collection and processing derived from environmental sensors. This demonstrates the Raspberry Pi's versatility in sensor technology and data acquisition.

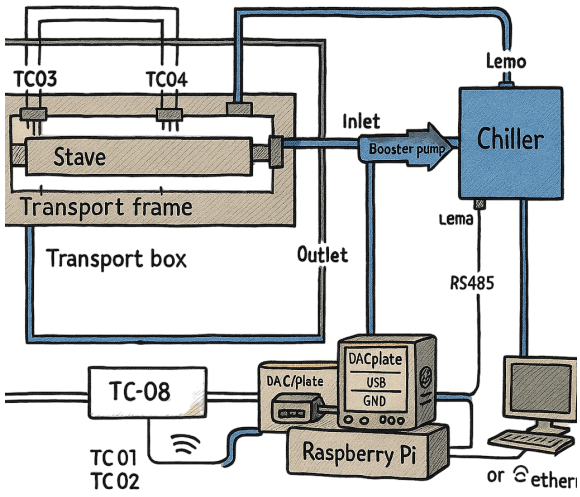


Figure 5.9: setup used for the thermal cycle testing at the BNL clean room.

5.4 Results and Analysis

ITk Strip modules undergo rigorous quality control (QC) during the intermediate phase between production of the module and assembly of the stave. Each module is exposed to ten thermal cycles, ranging from -35°C to 40°C, meticulously monitored by Hybrid NTC thermistors. Any modules failing the required standards are rigorously processed, fixed if possible, and re-tested to guarantee adherence to quality standards. During the thermal cycling process, a Python-based control and readout software system tracks stave temperature and humidity. This rigorous protocol of quality monitoring guarantees that only modules meeting performance criteria proceed to the next stages of stave assembly, ensuring the reliability and integrity of the overall final product.

A Python-based control and readout software system monitors temperature and humidity of the stave throughout the thermal cycling process. The collected data are stored and retrieved using the InfluxDB [82] database and displayed using Grafana [83] open-source software, as illustrated in Figure 5.10. This graph illustrates the results of the thermal cycling process, initiated from room temperature (RT) down to -45°C, as a function of time. It simultaneously captures humidity variations inside the stave box.

The thermal cycling tests confirm the robustness of the ITk stave under exami-

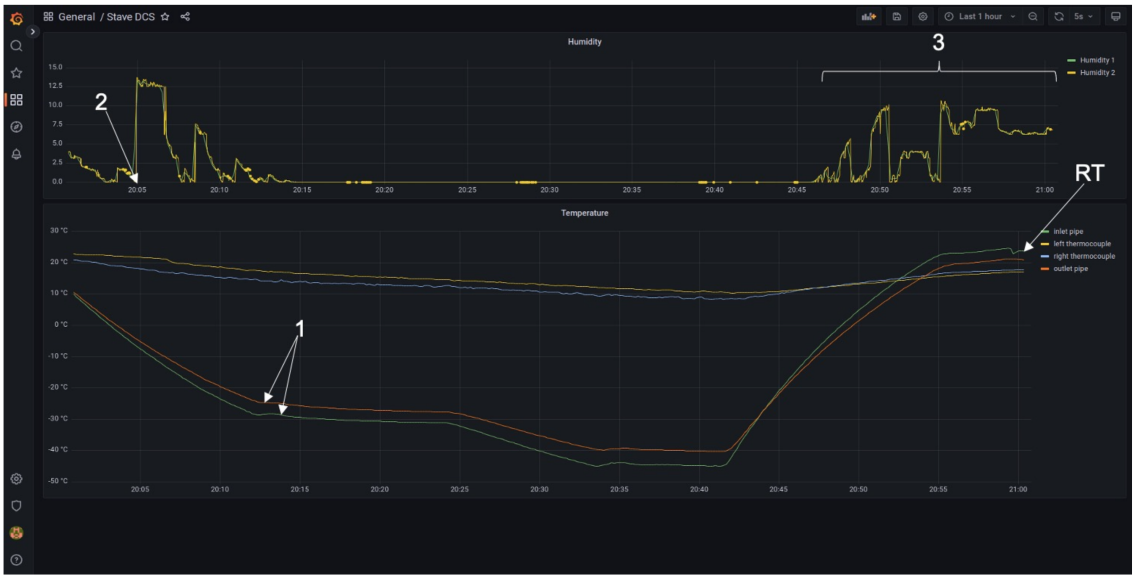


Figure 5.10: The humidity (top) and temperature (down) variations during the thermal cycle testing of the stave in the function of the measurement's time.

nation, demonstrating its capacity to cope with a temperature range from 21°C to -45°C without incurring notable damage or performance degradation. Figure 5.10 shows that the outlet pipe temperature is higher than the inlet pipe one, reflecting the thermal mass of the stave core. In addition, a rise in humidity inside the box is observed when dry air is disabled, pointing to a clear correlation between the lack of dry air and increased humidity levels. When the chiller is reset to room temperature, the air temperature rises, leading to further investigation of the humidity pattern. One possible reason is evaporation of trapped water. This detailed study of the thermal performance of ATLAS ITk strip modules at BNL is essential to guarantee the reliability and lifetime of detector components.
Building on this, further developments on this last two years have been implemented to enhance monitoring and visualization capabilities. Significant improvements have been implemented in the Grafana interface to provide more comprehensive real-time displays of critical parameters during the thermal cycle. As illustrated in Figures 5.11 and 5.12, these dashboards now feature visualizations for module high voltage (HV), low voltage (LV), AMAC currents, short-circuit behavior and chiller performance, in parallel with temperature and humidity readouts. These improvements enable operatives to monitor several aspects of stave performance simultaneously, thereby identifying and solving potential problems more rapidly. In addition, this installa-

tion continues to be actively used at BNL for quality control testing, with ongoing improvements guaranteeing its scalability for future experiments.



Figure 5.11: Real-Time Monitoring of Stave Thermal Cycling and Humidity Trends Using Grafana



Figure 5.12: Electrical Performance During Thermal Cycling: HV, LV, and AMAC Current Analysis.

6

Search for Dark Vector Bosons and New Scalars in $Z_d Z_d \to 4\ell$ Final State

This chapter reports on a novel search for dark vector bosons and additional scalar particles in the four-lepton final state, based on proton-proton collision data collected at a center-of-mass energy of 13 TeV. The analysis is performed using the full Run 2 dataset from the LHC, corresponding to an integrated luminosity of 138 fb^{-1}, recorded between 2015 and 2018. The chapter begins with a description of the overall analysis strategy, followed by detailed discussions of the event selection, background modelling, systematic uncertainties, and statistical interpretation. The search probes scalar masses up to 800 GeV and Z_d masses below 300 GeV, with sensitivity diminishing at higher mass ranges due to the broadening of the scalar and Z_d resonances. Events are studied in the $(m_{4\ell}, m_{Z_d})$ plane, where the reconstructed four-lepton invariant mass and the average dilepton mass of the Z_d candidates provide key discriminating variables. No significant excess over the Standard Model background prediction is observed. Consequently, upper limits at the 95% confidence level are set on the product of the production cross-section and branching ratio. These results place new constraints on the parameter space of the HAHM model and offer valuable input for broader interpretations involving four-lepton final states.

6.1 Analysis Strategy

The search for dark vector bosons (Z_d) and new scalars in the $Z_dZ_d \to 4\ell$ final state consists in identifying exotic decays of the Higgs boson (H) through a hypothetical dark sector as mentioned in 3. This analysis employs data from proton-proton (pp) collisions at the Large Hadron Collider (LHC) and focuses on events where the Higgs boson decays into four leptons via intermediate dark vector bosons with mass distinct from the 125 GeV Higgs boson (m_S [15,115[]130,800] GeV). The strategy employed is described below:

- The analysis assumes an extension of the Standard Model (SM) with a hidden or dark sector characterized by an additional U(1)dU(1)d gauge symmetry. This symmetry introduces a dark vector boson. This introduces a dark vector boson (Z_d) and potentially a dark Higgs boson.
- The Higgs boson decay channel $H \to Z_dZ_d \to 4\ell$ is studied, where Z_d decays into pairs of electrons or muons, producing three distinct final states: $4e$, $2e2\mu$, and 4μ.
- The branching ratio BR($H \to Z_dZ_d$) is constrained by experimental observations and theoretical coupling parameters such as kinetic mixing (ϵ) and Higgs gate coupling (κ).

6.2 Object and Event selection

The object and event selection is crucial for isolating events consistent with the decay $S \to Z_dZ_d \to 4\ell$, where S is a new scalar and Z_dZ_d is a dark vector boson. Event selection requires several steps, the first is the basic quality preselection. Second is the identification of leptons and the formation and ranking of $'quadruplets'$ of four leptons. The final one is the event selection.

6.2.1 Event preselection

Events are preselected with basic event requirements:

- GRL: event must pass Good Run Lists.
- Cleaning: event must not have LArError, TileError, SCTError, or CoreError
- Trigger: event must fire at least one of the triggers listed in Table 6.1.
- Primary vertex: event must have at least one primary vertex reconstructed with two or more associated tracks with $p_T = 400\ MeV$.

- Number of leptons: at least four leptons.

6.2.2 Baseline lepton selection

Electrons and muons have to satisfy specific basic selection criteria before quadruplets can be established. Electrons are considered to be in the limit of $|\eta| < 2.47$, possess $p_T > 7$ GeV, with a longitudinal impact parameter $\mid z_0 \sin\theta \mid < 0.5$ mm. In addition, they must satisfy a Loose likelihood identification test and an object quality test. For muons, the $|\eta| < 2.5$ region will be taken into account. Muons are required to have a $p_T > 5$ GeV (> 15 GeV if tagged), the impact parameter $|z_0 \sin\theta| < 0.5$ mm and $d_0 < 1$ mm. They must also pass a loose identification cut.

6.2.3 Selection and ranking of quadruplets

After base lepton selection, quadruplets are formed with events containing at least four leptons. Each quadruplet should be composed of lepton pairs of the same flavor and opposite sign (SFOS). The leptons in each quadruplet are ranked according to their transverse momentum (p_T), with the leading, sub-leading and third-leading leptons required to have $p_T > 20$ GeV, $p_T > 15$ GeV and $p_T > 10$ GeV respectively. In order to guarantee that the selected leptons are responsible for triggering the event, at least one lepton in the quadruplet must correspond to a triggered trigger; for multi-lepton triggers, all triggering leptons must correspond to leptons in the quadruplet. For quadruplets containing muons, no more than one can be a calo-tagged or stand-alone muon. To minimize overlap and misidentification, overlap removal algorithms are applied, particularly for electrons that either share tracks or clusters with muons or other electrons, or fail to meet the identification criteria. In addition, in order to guarantee good lepton separation, the minimum distance in the pseudorapid-azimuthal angle (ΔR) between leptons of the same flavor must be greater than 0.10, and 0.20 for leptons of different flavors. If more than one quadruplet meets all these requirements at the same event, the quadruplet with the lowest mass difference between its two SFOS pairs ($\Delta m_{ell\ell} = |m_{ab} - m_{cd}|$) is chosen as the best candidate.

6.2.4 Event selection

Once the quadruplet has been selected, rigorous criteria are then applied to the leptons in the quadruplet for further signal refinement. These requirements are intended to guarantee that the selected leptons are rapid, well-identified and originate from the primary vertex interaction.

ℓ	Trigger name	2015	2016	2017	2018
e	HLT_e24_lhmedium_L1EM20VH	*Ok*			
	HLT_e24_lhmedium_iloose_L1EM18VH				
	HLT_e24_lhtight_nod0_ivarloose		*Ok*		
	HLT_e26_lhtight_nod0				*Ok*
	HLT_e26_lhtight_nod0_ivarloose		*Ok*	*Ok*	*Ok*
	HLT_e60_lhmedium	*Ok*	*Ok*		
	HLT_e60_lhmedium_nod0		*Ok*	*Ok*	*Ok*
	HLT_e60_medium				
ee	HLT_2e12_lhloose_L12EM10VH	*Ok*			
	HLT_2e15_lhvloose_nod0_L12EM13VH		*Ok*		
	HLT_2e17_lhvloose_nod0		*Ok*		
	HLT_2e17_lhvloose_nod0_L12EM15VHI			*Ok*	*Ok*
	HLT_2e24_lhvloose_nod0			*Ok*	*Ok*
μ	HLT_mu20_iloose_L1MU15	*Ok*			
	HLT_mu26_ivarmedium		*Ok*	*Ok*	*Ok*
	HLT_mu50	*Ok*	*Ok*	*Ok*	*Ok*
	HLT_mu60_0eta105_msonly	*Ok*	*Ok*	*Ok*	*Ok*
$\mu\mu$	HLT_mu18_mu8noL1	*Ok*			
	HLT_mu22_mu8noL1		*Ok*	*Ok*	*Ok*
	HLT_2mu10	*Ok*	*Ok*		
	HLT_2mu14		*Ok*	*Ok*	*Ok*
$e\mu$	HLT_e17_lhloose_mu14	*Ok*			
	HLT_e17_lhloose_nod0_mu14		*Ok*	*Ok*	*Ok*
	HLT_e24_lhmedium_nod0_L1EM20VHI_mu8noL1		*Ok*		
	HLT_e26_lhmedium_nod0_mu8noL1			*Ok*	*Ok*
	HLT_e7_lhmedium_mu24	*Ok*			
	HLT_e7_lhmedium_nod0_mu24		*Ok*	*Ok*	*Ok*
$e\mu\mu$	HLT_e12_lhloose_2mu10	*Ok*			
	HLT_e12_lhloose_nod0_2mu10		*Ok*	*Ok*	*Ok*
$ee\mu$	HLT_2e12_lhloose_mu10	*Ok*			
	HLT_2e12_lhloose_nod0_mu10		*Ok*	*Ok*	*Ok*
eee	HLT_e17_lhloose_2e9_lhloose	*Ok*			
	HLT_e17_lhloose_nod0_2e9_lhloose_nod0		*Ok*		
	HLT_e17_lhloose_nod0_2e10_lhloose_nod0_L1EM15VH_3EM8VH		*Ok*		
	HLT_e24_lhvloose_nod0_2e12_lhvloose_nod0_L1EM20VH_3EM10VH			*Ok*	*Ok*
$\mu\mu\mu$	HLT_mu18_2mu4noL1	*Ok*			
	HLT_mu20_2mu4noL1		*Ok*	*Ok*	*Ok*
	HLT_3mu4			*Ok*	
	HLT_3mu6	*Ok*	*Ok*	*Ok*	*Ok*
	HLT_3mu6_msonly	*Ok*	*Ok*	*Ok*	*Ok*

Table 6.1: Triggers used in the 2015-2018 analysis. Triggers are only used when they are unprescaled (a separate GRL is maintained for each trigger that records which lumiblocks the trigger was unprescaled for). Prescaled triggers are not included because of their low thresholds (the events that pass only prescaled triggers would not pass our lepton p_T cuts).

Requirements on Leptons in the Event Selection

a. **Lepton Quality and Identification:**
Events are selected according to the following requirements for leptons:

- All the quadruplet leptons must pass isolation cuts: FCLoose for electrons [84] and FCLoose_FixedRad for muons [85], each with close-by corrections.
- All the quadruplet electrons must pass the Loose likelihood identification.
- The significance of the transverse impact parameter calculated relative to the beam line d_0^{BL}Sig. must be < 3 for muons and < 5 for electrons (standalone muons are exempt because they do not have an ID track).

b. **Isolation:**
The leptons produced in association with quantum chromodynamic (QCD) processes frequently show tracks and energy deposits coming from nearby particles. In order to separate the prompt leptons arising from electroweak interactions and those originating from these processes, insulation conditions are applied. In this analysis, the FCLoose work point is used to isolate electrons, while the $FCLoose_FixedRad$ work point is used to isolate muons. This involves specific cuts to the tracker and calorimeter isolation variables, designed to efficiently identify isolated leptons. The isolation variables have been corrected to include contributions from other leptons in the quadruplet.
The calorimeter isolation variable, E_T^{cone20}, represents the sum of the topological cluster energies within a cone of $\Delta R = 0.2$ surrounding the lepton [86]. The tracer isolation variables, p_T^{coneXX} and $p_{T,TVA}^{coneXX}$, denote the sum of the track transverse moments within a cone of radius ΔR centered around the lepton. The tracks included in the sum must pass Loose track quality cuts, be included in the lepton vertex fit, and have $p_T > 1$ GeV. The cone radius in p_T^{coneXX} is given by $XX/100$, meanwhile the cone radius for $p_{T,TVA}^{coneXX}$ is varying and given by $DeltaR = \min(10\mathrm{GeV}/p_T, XX/100)$. FCLoose uses XX = 20, while FCLoose_FixedRad uses XX = 20 or 30, depending on the muon's transverse momentum.
Isolation cuts for FCLoose are $E_T^{cone20}/p_T < 0.2$ and $p_{T,TVA}^{cone20}/p_T < 0.15$, while for FCLoose_FixedRad they are $E_T^{cone20}/p_T < 0.3$ and
$\max(p_{T,VAT}^{cone30}/p_T, p_{T,VAT}^{cone20}/p_T) < 0.15$.
In order to take into consideration the energy contributions of other leptons, the isolation variables are corrected. This correction takes into account only

the other three leptons in the quadruplet. For E_T^{cone20}, we subtract E_T from the topoclusters located within $0.1 < \Delta R < 0.2$ of the lepton. For $p_{T,TVA}^{coneXX}$, we subtract p_T from the detector's inner track from any of the other three leptons in the variable-size isolation cone of the track. These corrections are made for each quadrupole lepton, before the isolation conditions are applied.

6.2.5 Kinematic requirements in event selection

Kinematic requirements play a major part in the refinement of event selection to enhance signal sensitivity while eliminating background contributions. In this analysis, the four-lepton invariant mass ($m_{4\ell}$) is the primary kinematic variable used to define signal regions matching the different mass assumptions of the new scalar particle. Two distinct signal regions are established: Signal Region 1 (SR1), targeting low-mass scalars with $m_{4\ell} < 15GeV$, and Signal Region 2 (SR2), focusing on higher-mass scalars with $m_{4\ell} > 130\ GeV$. All events outside these windows are ignored to minimize contamination by Standard Model processes.

a. **Medium Signal Region (SR) Cut:**
A requirement on the compatibility of the dilepton invariant masses is enforced through the condition:

$$m_{cd} > 0.85m_{ab} - 0.1125f(m_{ab})m_{ab}, \tag{6.1}$$

where $f(m_{ab})$ is a modulation function having constants derived from signal optimization. It is an extended version of the old "wedge" cut-off $m_{cd}/m_{ab} > 0.85$ and it is a requirement for dilepton invariant mass compatibility.

b. **Quarkonia Veto:**
Events are rejected if any of the dilepton invariant masses (m_{ab}, m_{cd}, m_{ad}, m_{cb}) fall within the following ranges to veto quarkonia:

- $(m_{J/\psi} - 0.25\ \text{GeV}) < m_{ab,cd,ad,cb} < (m_{J/\psi} + 0.25\ \text{GeV})$
- $(m_{\Upsilon(2S)} - 0.30\ \text{GeV}) < m_{ab,cd,ad,cb} < (m_{\Upsilon(2S)} + 0.30\ \text{GeV})$
- $(m_{\Upsilon(1S)} - 0.70\ \text{GeV}) < m_{ab,cd,ad,cb} < (m_{\Upsilon(1S)} + 0.70\ \text{GeV})$
- $(m_{\Upsilon(3S)} - 0.75\ \text{GeV}) < m_{ab,cd,ad,cb} < (m_{\Upsilon(3S)} + 0.75\ \text{GeV})$

c. **Z Boson Veto:**
To reduce background from Standard Model Z boson decays, a Z boson veto is applied [87]:

- In SR1, events with $m_{ab} \notin [50, 106]$ GeV are rejected.

- In SR2, events with m_{ab} and $m_{cd} \notin [83.2, 99.2]$ GeV, and m_{ad} and $m_{cb} \notin [87.2, 95.2]$ GeV are rejected. The Z boson veto cut is defined by the optimization procedure discussed in Appendix D.

d. **Additional Kinematic Cut:**
An additional cut on the $E'_{ab}/m_{4\ell}$ variable is used for both SR1 and SR2. This kinematic variable is defined as the energy component of the lepton pair's four-momentum in the centre-of-momentum frame (CMF). The distribution of this variable is shown in Figure 6.1.

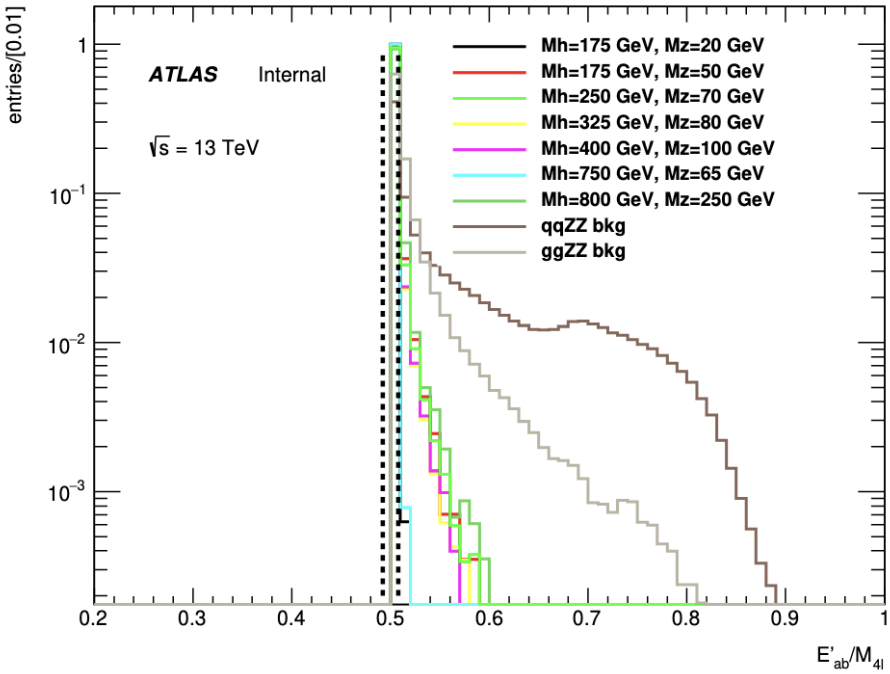


Figure 6.1: $E'_{ab}/m_{4\ell}$ distributions for additional scalar signal hypotheses and the two leading SM background processes. The dotted lines delimit the cut applied using this variable.

These kinematic selections, summarized in Table 6.2, provide a collective optimization of the signal efficiency/background rejection balance, resulting in a sensitive search for new physics in the final $Z_d Z_d 4\ell$ state. Figure 6.1 illustrates the distribution of the variable $E'_{ab}/m_{4\ell}$, allowing a better understanding of its role in the separation between signal and background detection [87].

	cuts	SR1	SR2
Baseline Electrons	p_T	> 7 GeV	same
	η	$\|\eta\| < 2.47$	same
	ID	Silicon and Pixel Hits requirements of LooseLH working point	same
	OQ	Not from a bad cluster	same
	$z_0 \sin\theta$	< 0.5 mm	same
Baseline Muons	p_T	> 6 GeV (15 GeV if calo-tagged)	same
	η	$\|\eta\| < 2.7$	same
	ID	Loose	same
	$z_0 \sin\theta$	< 0.5 mm	same
	$\|d_0\|$	< 1 mm if muon is not StandAlone	same
Quadruplet formation	Quadruplet	At least one quadruplet formed from two SFOS dilepton pairs.	same
Quadruplet Selection	Overlap removal	No overlap-removed e or μ	same
	p_T	$p_T^1 > 20$ GeV, $p_T^2 > 15$ GeV, $p_T^3 > 10$ GeV	same
	Trigger matched	Leptons in quadruplet responsible for firing at least one trigger	same
	ΔR	> 0.1 between same-flavor leptons, > 0.2 between different-flavor	same
	Muon Quality	Number of StandAlone or CaloTagged$\mu <$ 2	same
Quadruplet Ranking	Minimal Δm	Select quadruplet with smallest $\Delta m = \|m_{ab} - m_{cd}\|$	same
Event Selection	Electron ID	All e in quadruplet pass LooseLH working point	same
	Isolation	All leptons in quadruplet pass Fixed-CutLoose working point	same
	Impact Parameter	$\|d_0^{BL}Sig.\| < 5(3)$ for $e(\mu)$ in quadruplet	same
	Quarkonia Veto	$(m_{J/\psi} - 0.25\text{ GeV}) < m_{ab}, m_{cd}, m_{ad}, m_{cb} < (m_{\psi(2S)} + 0.30\text{ GeV})$ or, $(m_{\Upsilon(1S)} - 0.70\text{ GeV}) < m_{ab}, m_{cd}, m_{ad}, m_{cb} < (m_{\Upsilon(3S)} + 0.75\text{ GeV})$	same
	LowMass Veto	$(m_{ab}, m_{cd}, m_{ad}, m_{cb}) > 5$ GeV	same
	ZVeto	$m_{ab} \notin [50, 106]$ GeV	m_{ab} and $m_{cd} \notin [83.2, 99.2]$ GeV, m_{ad} and $m_{cb} \notin [87.2, 95.2]$ GeV
	LooseSR	$(m_{ab}, m_{cd}, m_{ad}, m_{cb}) > 10$ GeV	same
	H veto	$m_{4\ell} < 115$ GeV	$m_{4\ell} > 130$ GeV
	MediumSR	new SR	same
	TightSR	$\|E'_{ab}/M_{4\ell} - 0.5\| < 0.008$	same

Table 6.2: Summary of the event selection of SR1 and SR2 for the AS search.

6.3 Background simulation

Accurate modeling of background processes is crucial for the search of dark vector bosons and new scalars in the ZdZd→4 final state. The dominant backgrounds come from Standard Model processes that produce four-lepton final states or imitate them by misidentification.

6.3.1 Irreducible Backgrounds

The primary irreducible background is the Standard Model production of four-lepton final states via $ZZ^{(*)}$ processes. These include:

- **Non-resonant $ZZ^* \to 4\ell$:** This is the main background for the additional scalar (AS) channel, which accounts for over 90% of the overall prediction. Production of ZZ^* initiated by quarks and antiquarks ($q\bar{q}$), and by gluons and loop-induced gluons (gg) are taken into account. Table 6.3 shows the simulated yields after selections.

- **Higgs Boson Decays ($H \to ZZ^* \to 4\ell$):**Higgs boson production by gluon-gluon fusion (ggF), vector-boson fusion (VBF), and associated production with a vector boson (VH) or top quarks ($t\bar{t}H$), contribute as a subdominant background. This contribution is eliminated by requiring that $m_{4\ell} > 130$ GeV in SR1 or $m_{4\ell} < 115$ GeV in SR2.

- **Triboson Production VVV:**Processes such as ZZZ, WZZ, and WWZ, where four or more leptons originate from the hard scatter, are included. Although these processes have smaller cross sections, they contribute to the background due to their similar final-state topology.

6.3.2 Reducible Backgrounds

Reducible backgrounds arise from processes that produce fewer than four prompt leptons but can mimic the signal through jets misidentified as leptons. The main sources of reducible backgrounds include:

- **Z+jets:** Events where jets are misidentified as electrons or muons contribute significantly to the reducible background. These fake leptons often originate from heavy-flavor decays (e.g., b or c quarks) or hadrons misreconstructed as leptons. The Z+jets background is challenging to simulate accurately and is typically estimated using data-driven methods such as the "matrix method" or "fake-factor" techniques, which measure the probability of jets faking leptons in control regions enriched with jets.

- **Top-quark processes ($t\bar{t}$ and single top):** Top pair production and single top events produce real leptons from W boson decays, but additional jets or non-prompt leptons can be misidentified as prompt leptons, contributing to the four-lepton candidate sample. These backgrounds are modeled using Monte Carlo simulations normalized to theoretical cross sections, with corrections applied to account for differences in lepton identification efficiencies between data and simulation.

- WZ **production:** Although WZ events produce three prompt leptons, misidentification of jets or non-prompt leptons as an additional lepton can lead to four-lepton final states. This background is also modeled with MC simulation and constrained using control regions.

To suppress reducible backgrounds, analyses impose stringent lepton identification and isolation criteria, as well as requirements on the transverse impact parameter significance (d_0/σ_{d_0}), exploiting the fact that leptons from heavy-flavor decays tend to originate from displaced vertices and are less isolated than prompt leptons from electroweak processes.
The simulation of reducible backgrounds follows the methodology established in previous ATLAS analyses, with updated software and extended datasets. Pile-up effects are included in the simulation, and corrections are applied to match lepton reconstruction, identification, and isolation efficiencies observed in data. Data-driven techniques remain essential to accurately estimate the contribution of fake leptons, ensuring robust background predictions in the signal regions.

6.4 Signal simulation

Event samples were generated for the $S \to Z_d Z_d \to 4\ell$ process, where S is the dark Higgs boson and Z_d is the dark vector boson. The generation was performed in the gluon-gluon fusion (ggF) production mode via the hidden abelian Higgs model (HAHM). Event generator MadGraph5_aMC@NLO v2.2.3 has been employed to generate main-order (LO) events with NNPDF23 parton distribution functions (PDFs). In addition, the parton shower, hadronization and underlying event modeling were interfaced with Pythia8 v8.170 using A14 tuning.
Samples were generated respecting the requirements below:

- Considering different S and Z_d masses, the region of $m_S < 115$ GeV was used for SR1, and $m_S > 130$ GeV for SR2.

- The model parameters $\kappa \gg \epsilon$ were adjusted to allow only the $S \to Z_d Z_d \to 4\ell$ decay.

- The dark Higgs width was varied according to the S mass, as reported in the reference. This is shown in Figure 6.2, which illustrates the width of both SM and dark Higgs bosons [88].
- For normalization, we use the Higgs boson production cross section SM $\sigma_{SM}(ggF)$.
- The branching ratio $\mathcal{B}(H \to Z_d Z_d \to 4\ell) = 1$ was assumed.

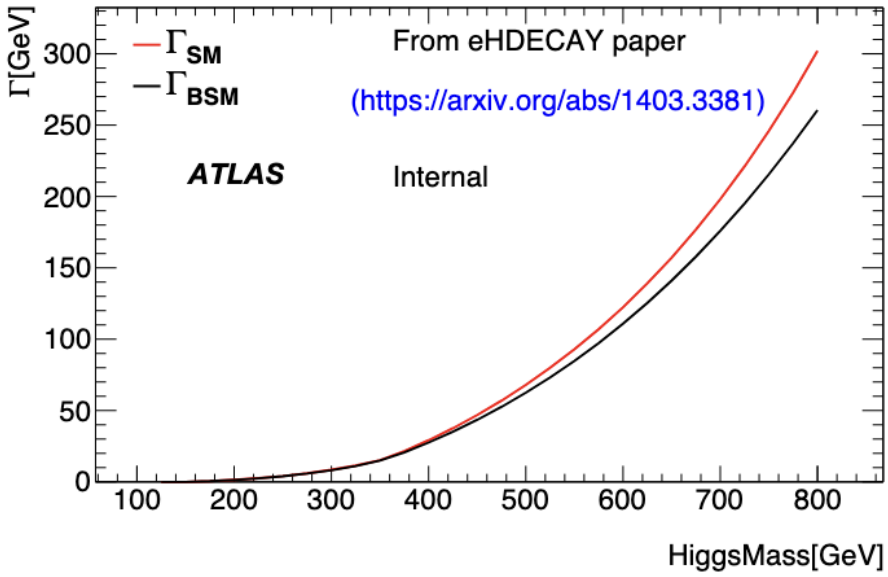


Figure 6.2: Width of the SM Higgs boson compared to that of a BSM dark Higgs boson as a function of mass.

The simulated event yields and selection efficiencies for representative mass points (e.g., $(20, 50)$ and $(50, 400)$ GeV) are documented in Tables 6.4 and 6.5.
This framework ensures a consistent and theoretically grounded simulation of the dark Higgs signal, enabling robust sensitivity studies for the 4ℓ final state.

6.5 Background estimation

Background estimation in this analysis employs two principal methods to account for irreducible and reducible background contributions. Irreducible backgrounds, such as ZZ^*4l, will be estimated using Monte Carlo simulations. Reducible backgrounds, which involve events mimicking the signal signature due to misidentification or un-driven leptons, are estimated with a data-driven ABCD method.

Cleaning	96200
Primary Vertex	70400

Selection	4e		2e2μ		4μ		all	
	Yield	Eff(%)	Yield	Eff(%)	Yield	Eff(%)	Yield	Eff(%)
SFOS	4770	100	8900	100	3250	100	16900	100
Not Overlaps	4770	99.9	8890	99.9	3250	100	16900	99.9
Kinematics	4290	89.9	7690	86.4	2710	83.4	14700	86.8
Trigger Matched	4250	89.1	7660	86.1	2710	83.5	14600	86.5
DeltaR	4040	84.7	7170	80.5	2720	83.6	13900	82.3
μ Quality	4040	84.7	7170	80.5	2710	83.5	13900	82.3
Isolation	1510	31.7	3570	40.1	2260	69.5	7340	43.4
Electron ID	934	19.6	2790	31.3	2260	69.5	5980	35.3
Impact Parameter	917	19.2	2690	30.3	2150	66.0	5760	34.0
QVeto	866	18.1	2580	28.9	1960	60.4	5410	31.9
Low Mass Veto	837	17.5	2460	27.6	1830	56.5	5130	30.3

SR1								
Selection	Yield	Eff(%)	Yield	Eff(%)	Yield	Eff(%)	Yield	Eff(%)
Higgs Window	105	2.20	410	4.61	399	12.3	915	5.41
ZVeto	91.3	1.91	165	1.86	344	10.6	601	3.55
LooseSR	77.2	1.62	84.9	0.954	285	8.77	447	2.64
MediumSR	23.2	0.487	12.3	0.138	75.1	2.31	111	0.653
TightSR	8.50	0.178	5.97	0.0671	26.8	0.825	41.3	0.244

SR2								
Selection	Yield	Eff(%)	Yield	Eff(%)	Yield	Eff(%)	Yield	Eff(%)
Higgs Window	716	15.0	1990	22.4	1380	42.6	4090	24.2
ZVeto	62.4	1.31	140	1.57	115	3.55	318	1.88
LooseSR	60.7	1.27	122	1.37	110	3.38	293	1.73
MediumSR	22.8	0.478	34.3	0.385	41.2	1.27	98.3	0.581
TightSR	14.0	0.293	23.4	0.263	26.6	0.817	63.9	0.378

Table 6.3: Cut flow for the simulated $ZZ^* \to 4\ell$ background with all production modes combined, corresponding to the full 2015–2018 data set, expressed as the number of predicted events and the fraction of events with a same-flavour opposite-sign quadruplet. Yields from each simulation campaign are individually normalized to the corresponding integrated luminosities (2015–2016: 36.2 fb^{-1}; 2017: 44.3 fb^{-1}; 2018: 58.45 fb^{-1}) and then combined (2015–2018: 139 fb^{-1}). Per-channel, the quadruplet cutflow can increase because events can move from one channel to another during the quadruplet selection if a higher-ranked quadruplet fails a cut that a lower-ranked one can pass (however, the cutflow summed across all channels can only decrease).

Selection	$(m_{Z_d}, m_S) = (20, 50)$ GeV			all	$(m_{Z_d}, m_S) = (50, 400)$ GeV			all
	4e	2e2μ	4μ		4e	2e2μ	4μ	
All	190000.000	190000.000	190000.000	190000.000	185039.720	185039.720	185039.720	185039.720
Overlap Event	190000.000	190000.000	190000.000	190000.000	185039.720	185039.720	185039.720	185039.720
Cleaning	190000.000	190000.000	190000.000	190000.000	185039.720	185039.720	185039.720	185039.720
PrimaryVertex	190000.000	190000.000	190000.000	190000.000	185039.720	185039.720	185039.720	185039.720
SFOS	3450.756	8919.814	6301.347	18671.917	37294.128	70642.735	32465.668	140402.531
Not Overlaps	3449.735	8916.470	6301.347	18667.551	37232.133	70562.442	32541.291	140335.865
Kinematics	2798.726	6214.907	2718.068	11731.702	36799.821	70300.796	32605.984	139706.601
Trigger Matched	2748.993	6211.297	2718.068	11678.358	36766.631	70288.637	32602.499	139657.227
DeltaR	2718.490	5601.768	2610.867	10931.125	36173.122	69601.775	32752.044	138526.940
μ Quality	2718.490	5601.937	2609.195	10929.622	36175.090	69595.690	32674.194	138442.425
Isolation	976.008	2546.520	1979.456	5501.984	25172.903	55759.806	30091.744	111024.453
Electron ID	652.079	2030.268	1979.456	4661.803	20134.228	49717.790	30091.744	99943.762
Impact Parameter	647.585	1983.055	1904.331	4534.970	19970.952	49055.728	29496.056	98522.736
Impact Parameter Z	646.534	1976.309	1902.236	4525.079	19933.329	48979.232	29459.000	98371.561
Impact Parameter D	646.534	1976.309	1902.236	4525.079	19933.329	48979.232	29459.000	98371.561
QVeto	555.074	1976.309	1621.124	4152.507	19932.371	48973.712	29452.074	98358.157
Low Mass Veto	536.281	1976.309	1556.778	4069.367	19932.371	48973.712	29451.273	98357.355
Higgs Window	535.560	1975.347	1556.778	4067.685	19931.388	48973.688	29450.184	98355.255
ZVeto	534.473	1975.347	1556.778	4066.597	19109.494	48973.536	28171.032	96254.063
LooseSR	534.473	1974.253	1556.778	4065.504	19109.494	48970.452	28168.920	96248.866
MediumSR	531.960	1964.048	1552.974	4048.268	18823.040	47610.824	27089.683	93523.552
TightSR	337.143	1385.954	1351.171	3074.268	18812.181	47608.624	27029.912	93450.717

Table 6.4: Cut-flow for the simulated signals with $(m_{Z_d}, m_S) = (20, 50)$ and $(m_{Z_d}, m_S) = (50, 400)$. The represented yields from simulation are for the combined campaigns (2015-18).

Selection	$(m_{Z_d}, m_S) = (20, 50)$ GeV				$(m_{Z_d}, m_S) = (50, 400)$ GeV			
	eff_{4e}	$\text{eff}_{2e2\mu}$	$\text{eff}_{4\mu}$	all	eff_{4e}	$\text{eff}_{2e2\mu}$	$\text{eff}_{4\mu}$	all
SFOS	100	100	100	100	100	100	100	100
Not Overlaps	99.97	99.96	100	100	99.83	99.88	100	99.95
Kinematics	81.1	69.67	43.13	99.97	98.67	99.51	100	99.5
Trigger Matched	79.66	69.63	43.13	62.83	98.58	99.45	100	99.48
DeltaR	78.78	62.8	41.43	58.54	96.99	98.52	100	98.66
μ Quality	78.78	62.8	41.41	58.53	96.99	98.51	100	98.6
Isolation	28.28	28.54	31.41	29.47	67.5	78.93	92.68	79.07
Electron ID	18.89	22.76	31.41	24.97	54	70.38	92.68	71.18
Impact Parameter	18.76	22.23	30.22	24.29	53.55	69.44	90.85	70.17
Impact Parameter Z	18.73	22.15	30.19	24.23	53.45	69.33	90.74	70.06
Impact Parameter D	18.73	22.15	30.19	24.23	53.45	69.33	90.74	70.06
QVeto	16.08	22.15	25.73	22.24	53.45	69.32	90.71	70.05
Low Mass Veto	15.54	22.15	24.7	22.24	53.45	69.32	90.71	70.05
Higgs Window	15.52	22.14	24.7	21.78	53.44	69.32	90.71	70.05
ZVeto	15.49	22.14	24.7	21.78	51.24	69.32	86.77	68.55
LooseSR	15.49	22.13	24.7	21.77	51.24	69.32	86.76	68.55
MediumSR	15.41	22.01	24.64	21.68	50.47	67.39	83.44	66.61
TightSR	9.77	15.54	21.44	16.46	50.44	67.39	83.25	66.56

Table 6.5: Cut-flow efficiency in SR1 and SR2.

6.5.1 Estimation of irreducible backgrounds

The irreducible background $ZZ^* \to 4l$ is estimated via Monte Carlo simulations and validated using the VR3 validation region. It is designed to be orthogonal to the signal regions, this orthogonality is achieved by reversing the "Medium SR" cutoff ($m_{cd} < 0.85m_{ab} - 0.1125f(m_{ab})m_{ab}$) in the SR and reversing the Higgs window requirement (m_{4l} <115 GeV and m_{4l} >130 GeV) in the signal regions.
These cuts result in the dominance of the $ZZ^* \to 4l$ process in validation region 3. Figure 6.3 shows the distributions of $(m_{ee}) = 1/2(m_{ab} + m_{34})$ in validation region 3, channel by channel. Figure 6.4 illustrates the distribution of m_{4l} in validation region 3 for all channels combined in the 2015-8 and MC data. VR3 demonstrates good agreement in terms of yield and shape between the data and the MC simulation. All irreducible backgrounds are normalized to theoretical cross sections.

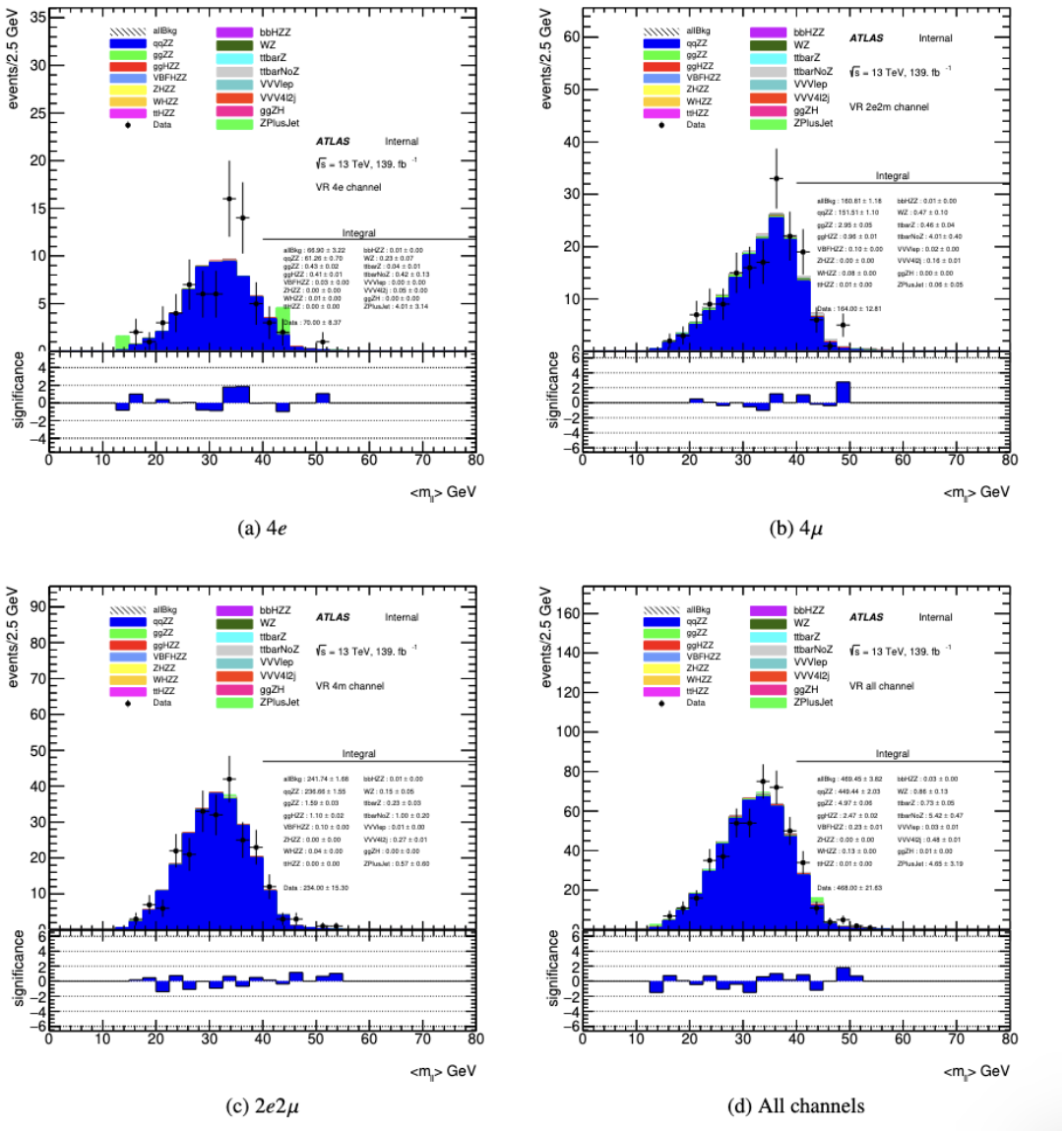
6.5.2 Estimation of reducible backgrounds

The estimation of reducible backgrounds in this analysis is performed using the ABCD method. This approach uses two uncorrelated variables - typically the isolation and impact parameter requirements - to define four distinct regions (A, B, C and D). The principal objective is to estimate backgrounds such as $Z +$ jets and $t\bar{t}$ that can mimic the signal signature due to misidentified leptons.

- For $t\bar{t}$, the two leptons with the largest p_T must pass both requirements.
- For $Z +$ jets, the two leptons in the pair with mass closest to the Z boson mass must pass both requirements.

The remaining two leptons are used to define the regions as follows:

- **Region A:** All leptons in the quadruplet pass both the isolation and impact parameter requirements.
- **Region B:** The two remaining leptons both pass the isolation requirement, but at least one fails the impact parameter requirement.
- **Region C:** The two remaining leptons both pass the impact parameter requirement, but at least one fails the isolation requirement.
- **Region D:** All other events.



(a) $4e$ (b) 4μ

(c) $2e2\mu$ (d) All channels

Figure 6.3: Distributions of $\langle m_{\ell\ell} \rangle = \frac{1}{2}(m_{ab} + m_{c,d})$ in validation region 3 in 2015–8 data and MC for the $4e$ channel (top left), the 4μ channel (top right), the $2e2\mu$ channel (bottom left), and all channels combined (bottom right). In this region, events are required to have $m_{4\ell}$ outside of the $115 < m_{4\ell} < 130\,\text{GeV}$ window and pass the inverted "medium SR" cut.

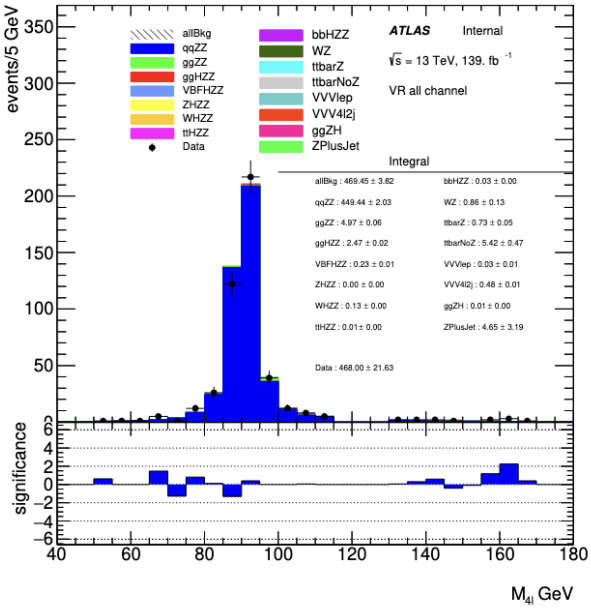


Figure 6.4: Width of the SM Higgs boson compared to that of a BSM dark Higgs boson as a function of mass.

A key assumption of the ABCD method is the statistical independence of the two background variables. It verified by computing the correlation coefficient r :

$$r = \frac{A \times D - B \times C}{\sqrt{(A+C) \times (B+D) \times (A+B) \times (C+D)}} \tag{6.2}$$

where A, B, C, and D represent the event counts in each respective region.
The calculated values of r for different channels and data-taking periods are provided in Table 6.6. These indicate that the isolation and d_{sig} variables are largely decorrelated for channels $4e$ and $2e2\mu$, as shown by r values close to zero. However, a significant correlation is observed in the 4μ channel, especially when considering the entire data set.

To maximize the available statistics, only the quarkonia veto is enforced at this stage, and the electron identification requirement is omitted. The procedure for estimating the reducible background proceeds as follows:

- All backgrounds are included except for X_{bkg}, the specific background under estimation (either $t\bar{t}$ or $Z + \text{jets}$).

	2015–16 data			2017 data			2018 data			Full data		
	$4e$	$2e2\mu$	4μ	$4e$	$2e2\mu$	4μ	$4e$	$2e2\mu$	4μ	$4e$	$2e2\mu$	4μ
r	0.01	0.02	0.59	0.02	0.02	0.59	0.02	0.02	0.59	0.002	0.002	0.38

Table 6.6: Correlation coefficient for the isolation and impact parameter requirements for the channels $4e$, $2e2\mu$, and 4μ, for the 2015–16, 2017 and 2018 data sets. All selections have been applied through the quarkonia vetoes.

- Determine the number of background events in each control region: B_{bkg}, C_{bkg}, and D_{bkg}.
- Record the observed data yields in the same regions: B_{data}, C_{data}, and D_{data}.
- For each control region, subtract the estimated background from the observed data: $(B_{\text{data}} - B_{\text{bkg}})$, $(C_{\text{data}} - C_{\text{bkg}})$, and $(D_{\text{data}} - D_{\text{bkg}})$.
- The expected yield of X_{bkg} in the signal region (A) is then given by:

$$X^{\text{A}}_{\text{bkg}} = \epsilon \times \frac{(B_{\text{data}} - B_{\text{bkg}}) \times (C_{\text{data}} - C_{\text{bkg}})}{D_{\text{data}} - D_{\text{bkg}}} \tag{6.3}$$

  where ϵ represents the efficiency of the remaining selection criteria.

A summary of the results for each step, as well as the estimated $t\bar{t}$ and $Z+\text{jets}$, can be found in Tables 6.8 6.7. These results confirm that, after applying all selections, the reducible backgrounds are found to be negligible.

6.6 Systematics uncertainties

The systematic uncertainties play an important role in high energy physics measurement. They are related to the experiment itself, the calibration and also the theory or model used by the experimenter.

6.6.1 Experimental systematic uncertainties

Experimental systematics mainly consist of the scaling factors used to correct the MC simulation with a reference to the data. The uncertainties considered for electrons and muons relate to the following quantities:

- Quantities related to the reconstruction and isolation of leptons;

Yields data	2015–16 data			2017 data		
	4e	2e2μ	4μ	4e	2e2μ	4μ
A	4144	5475	720	4728	6459	817
B	374	548	78	415	673	67
C	388373	449440	567	456758	532387	652
D	60527	65410	865	67790	76987	1054
Yields bkg without $t\bar{t}$						
	mc16a			mc16d		
A	3803.38	4805.01	535.02	4898.73	6236.65	627.53
B	284.44	331.91	46.27	389.85	650.24	60.14
C	331567	379154	322.17	389158	525338	908.49
D	30111.8	34514.1	598.31	44644.9	52338	908.39
(data) – (bkg without $t\bar{t}$)						
	(data) – (mc16a)			(data) – (mc16d)		
A	340.62	669.99	184.98	-170.73	222.35	189.47
B	89.56	216.09	31.73	25.15	22.76	6.86
C	56806	70286	244.83	67600	7069	466.57
D	30415.2	30895.9	266.69	23145.1	24649	145.61
AS (SR1)						
efficiency (ε)	$(9.29 \pm 3.52) \times 10^{-6}$	$(2.40 \pm 0.31) \times 10^{-6}$	0.03 ± 0.00	$(1.50 \pm 0.41) \times 10^{-5}$	$(3.10 \pm 0.31) \times 10^{-5}$	0.03 ± 0.00
$t\bar{t}$ estimates	0.00 ± 0.00	0.00 ± 0.00	0.16 ± 0.13	0.00 ± 0.00	0.00 ± 0.00	0.03 ± 0.01
Estimates including systematics	0.00 ± 0.01	0.00 ± 0.01	0.16 ± 0.13	0.00 ± 0.00	0.00 ± 0.00	0.03 ± 0.01
AS (SR2)						
efficiency (ε)	$(2.65 \pm 1.88) \times 10^{-6}$	$(1.56 \pm 0.24) \times 10^{-6}$	0.02 ± 0.00	$(6.96 \pm 2.84) \times 10^{-6}$	$(1.78 \pm 0.24) \times 10^{-5}$	0.03 ± 0.00
$t\bar{t}$ estimates	0.00 ± 0.00	0.00 ± 0.00	0.11 ± 0.07	0.00 ± 0.00	0.02 ± 0.03	0.03 ± 0.00
Estimates including systematics	0.00 ± 0.00	0.00 ± 0.00	0.11 ± 0.08	0.00 ± 0.00	0.02 ± 0.03	0.03 ± 0.00
HM						
efficiency (ε)	$(2.66 \pm 1.88) \times 10^{-6}$	$(1.15 \pm 0.21) \times 10^{-6}$	0.01 ± 0.00	$(1.16 \pm 1.16) \times 10^{-6}$	$(1.39 \pm 0.21) \times 10^{-6}$	0.01 ± 0.01
$t\bar{t}$ estimates	0.00 ± 0.00	0.00 ± 0.00	0.04 ± 0.06	0.00 ± 0.00	0.00 ± 0.00	0.00 ± 0.00
Estimates including systematics	0.00 ± 0.00	0.00 ± 0.00	0.04 ± 0.06	0.00 ± 0.00	0.00 ± 0.00	0.00 ± 0.02

Table 6.7: Estimation of the $t\bar{t}$ background in HM and AS search for the 2015–16 data (with mc16a MC) and the 2017 data (with mc16d MC), by channel.

Yields data	2015–16 data			2017 data		
	4e	2e2μ	4μ	4e	2e2μ	4μ
A	4144	5475	720	4728	6459	817
B	374	548	78	415	673	67
C	388373	449440	567	456758	532387	652
D	60527	65410	865	67790	76987	1054
Yields bkg without Z + jets						
	mc16a			mc16d		
A	492.50	1033.72	537.35	577.6	1128.12	479.8
B	51.92	102.675	19.14	61.63	107.31	22.95
C	2801.7	7069.6	100.43	14821.5	20743	350.4
D	1457.1	2026.2	366.94	16792.1	22763	551.03
(data) – (bkg without Z + jets)						
	(data) – (mc16a)			(data) – (mc16d)		
A	3651.5	4441.28	182.65	4150.4	5330.88	337.2
B	322.08	445.33	58.86	353.37	565.69	44.05
C	385571.3	442370.4	466.57	441936.5	511644	301.6
D	59069.9	63383.8	498.06	50997.9	54224	502.97
AS (SR1)						
efficiency (ε)	$(9.29 \pm 3.52) \times 10^{-4}$	$(2.41 \pm 0.30) \times 10^{-3}$	0.03 ± 0.00	$(1.51 \pm 0.42) \times 10^{-3}$	$(3.13 \pm 0.32) \times 10^{-3}$	0.03 ± 0.00
Z+jets estimates	0.08 ± 0.01	0.12 ± 0.02	0.63 ± 0.33	0.06 ± 0.02	0.10 ± 0.02	0.55 ± 0.31
Estimates including systematics	0.03 ± 0.01	0.12 ± 0.02	0.63 ± 0.37	0.06 ± 0.02	0.10 ± 0.02	0.55 ± 0.41
AS (SR2)						
efficiency (ε)	$(2.65 \pm 0.19) \times 10^{-4}$	$(1.58 \pm 0.24) \times 10^{-3}$	0.02 ± 0.00	$(6.98 \pm 2.84) \times 10^{-4}$	$(1.75 \pm 0.24) \times 10^{-3}$	0.03 ± 0.00
Z+jets estimates	0.01 ± 0.01	0.08 ± 0.02	0.44 ± 0.24	0.03 ± 0.01	0.08 ± 0.02	0.41 ± 0.20
Estimates including systematics	0.01 ± 0.01	0.08 ± 0.02	0.44 ± 0.25	0.03 ± 0.01	0.08 ± 0.02	0.41 ± 0.28
HM						
efficiency (ε)	$(2.66 \pm 1.88) \times 10^{-4}$	$(1.15 \pm 0.21) \times 10^{-3}$	0.04 ± 0.00	$(1.16 \pm 1.16) \times 10^{-4}$	$(1.19 \pm 0.21) \times 10^{-3}$	0.04 ± 0.01
Z+jets estimates	0.01 ± 0.01	0.06 ± 0.01	0.18 ± 0.11	0.00 ± 0.00	0.01 ± 0.00	0.07 ± 0.04
Estimates including systematics	0.01 ± 0.01	0.06 ± 0.01	0.18 ± 0.13	0.00 ± 0.00	0.01 ± 0.00	0.07 ± 0.08

Table 6.8: Estimation of the Z + jets background in HM and AS search for the 2015–16 data (with mc16a MC) and the 2017 data (with mc16d MC), by channel.

- The kinematic smearing parameter: it is used to simulate detector resolution for MC samples by pseudorandomly modifying the kinematics of the object according to assumed process.
- The calibration coefficients: they are transfer factors from detector raw hit value to energy in the case of electrons and momentum in the case of muons.
- The luminosity: the uncertainty of the integrated luminosity on the combined Run2 dataset (2015-8) is 1.7% as reported [88]. This uncertainty is applied on all the processes modeled with MC simulations.
- The pileup reweighting factor: this uncertainty covers the discrepancy seen between the predicted and the measured inelastic cross-section in the fiducial volume defined by $M_X > 13$ GeV, where M_X is the mass of the non-diffractive hadronic system. These discrepancies arise from mismodeling of the central activity by the Monte Carlo tune [89], so it can be incorporated into the analysis as an uncertainty on the signal strength $\langle\mu\rangle$ that a given MC event corresponds to.

For electrons, to enhance consistency with the data, the resolution, energy scale and identification/isolation/reconstruction efficiencies of electrons in the simulation are adjusted. The correction model provided by the egamma CP group's `AsgElectronEfficiencyCorrectionTool` [90] is used, where the keys are :

- `EL_EFF_ID_TOTAL`: Identification.
- `EL_EFF_ISO_TOTAL`: Isolation.
- `EL_EFF_RECO_TOTAL`: Reconstruction.

For resolution and energy scale corrections, kinematic smearing and calibration uncertainties are considered, where the calibration is a transfer factor from the detector's raw hit value to energy. The tool used is `EgammaCalibrationAndSmearingTool`, with the following keys:

- `EG_RESOLUTION_ALL`: Smearing.
- `EG_SCALE_ALL`: Calibration.

For muons, the resolution, momentum scale, and isolation/reconstruction/track-to-vertex association efficiencies of muons in simulation are similarly corrected. The tool used is `CP::MuonEfficiencyScaleFactors` [90], with the associated keys:

- `MUON_EFF_ISO_STAT`: Isolation efficiency broken up into statistical errors on the weights.
- `MUON_EFF_ISO_SYS`: Isolation efficiency broken up into systematic errors on the weights.
- `MUON_EFF_RECO_STAT`: Reconstruction efficiency broken up into statistical errors on the weights.
- `MUON_EFF_RECO_STAT_LOWPT`: Reconstruction efficiency which is extrapolated for muon with $p_T < 10$ GeV, broken up into statistical errors on the weights.
- `MUON_EFF_RECO_SYS`: Reconstruction efficiency broken up into systematic errors on the weights.
- `MUON_EFF_RECO_SYS_LOWPT`: Reconstruction efficiency which is extrapolated for muon with $p_T < 10$ GeV, broken up into systematic errors on the weights.
- `MUON_TTVA_ISO_STAT`: Track-to-vertex association efficiency broken up into statistical errors on the weights.
- `MUON_TTVA_ISO_SYS`: Track-to-vertex association efficiency broken up into systematic errors on the weights.

The calibration for muons is a transfer factor from detector's raw hit to momentum, and the tool `CP::MuonCalibrationAndSmearingTool` [90] is used with the keys:

- `MUON_ID`: Muon inner detector track p_T smearing.
- `MUON_MS`: Muon spectrometer track p_T smearing.
- `MUON_SCALE`: Muon calibration scale.

Table 6.11 presents the relative experimental uncertainties (%) in SR1 for the mass point $(m_H, m_A) = (35, 80)$ GeV and $(20, 175)$ GeV. The table shows the impact of each systematic uncertainty on the analysis.

6.6.2 Theoretical systematic uncertainties

Theoretical systematic uncertainties derive from the limits of our understanding regarding the underlying physical processes and their application in Monte Carlo generators. These uncertainties are especially significant in precision measurements and research where experimental uncertainties are closely controlled.
The main sources of theoretical uncertainties in this analysis include:

- **QCD scale variations**: Uncertainties from missing higher-order corrections in the perturbative QCD calculations are estimated by varying the renormalization (μ_R) and factorization (μ_F) scales up and down by a factor of two around the nominal value, while keeping their ratio within the range $0.5 \leq \mu_R/\mu_F \leq 2.0$. This produces seven independent scale variations that provide an estimate of the uncertainty from missing higher orders.

- **PDF uncertainties**: Uncertainties in the Parton Distribution Functions affect both signal and background predictions. These are evaluated following the PDF4LHC recommendations, using multiple PDF sets and taking the envelope of the resulting variations as a systematic uncertainty.

- **Parton shower and hadronization modeling**: Uncertainties related to parton showering, hadronization, and underlying event modeling are assessed by comparing predictions from different Monte Carlo generators. For key processes, we compare nominal samples with alternative samples generated using different generators or settings.

- **Signal modeling uncertainties**: For the signal processes, additional theoretical uncertainties include higher-order electroweak corrections, uncertainties on the heavy-flavor content in production mechanisms, and acceptance uncertainties due to scale variations.

These theoretical uncertainties are propagated through the analysis and their impact on the final results is quantified.

6.7 Results

Table 6.9 summarizes the observed and predicted event yields within the signal regions. In SR1 ($m_{4\ell} < 115$ GeV), a total of 36 events are recorded, compared to a background expectation of $32.6 \pm 0.5 \pm 3.3$. For SR2 ($m_{4\ell} > 130$ GeV), 55 events are observed, with an estimated background of $66.8 \pm 0.6 \pm 8.0$.

Process	Yield (± stat. ± syst.)	
	SR1	SR2
$ZZ^* \to 4\ell$	$30.9 \pm 0.5 \pm 3.2$	$62.0 \pm 0.5 \pm 7.9$
$H \to ZZ^* \to 4\ell$	$0.61 \pm 0.01 \pm 0.04$	$0.22 \pm 0.01 \pm 0.03$
WZ	$0.06 \pm 0.04 \pm 0.03$	$0.42 \pm 0.10 \pm 0.05$
VVV	$0.06 \pm 0.01 \pm 0.01$	$0.78 \pm 0.02 \pm 0.14$
$t\bar{t}$	$0.33 \pm < 0.01 \pm 0.31$	$0.78 \pm 0.01 \pm 0.46$
Z + jets	$0.70 \pm 0.01 \pm 0.72$	$2.53 \pm < 0.01 \pm 1.08$
Total	$32.6 \pm 0.5 \pm 3.3$	$66.8 \pm 0.6 \pm 8.0$
Data	36	55

Table 6.9: Expected event yields of the SM background processes and observed data in the two signal regions SR1 and SR2. The first uncertainty is the statistical component of the total uncertainty and the second the systematic component.

Signal Modeling and Interpolation Approach

The average dilepton mass distributions, $\langle m_\ell \rangle = \frac{1}{2}(m_a + m_{a'})$, for the two signal regions are shown in Figure 6.5. Figure 6.6 illustrates the distributions of the total invariant mass $m_{4\ell}$, which serves as a potential scalar resonance mass. Figure 6.7 shows selected events in the $(m_{4\ell}, \langle m_{ell\ell} \rangle)$ plane, while Figure 6.8 illustrates both the estimated background and a signal example within SR1.
To improve analysis at arbitrary points in parameter space (m_h, m_a), an advanced interpolation technique was implemented for the distribution $\langle m_\ell \rangle$. Signal shapes in SR1 were characterized by a three-parameter Gaussian function, giving good agreement with simulated distributions. For SR2, where pronounced asymmetry was observed, a more sophisticated two-sided Crystal Ball function comprising seven parameters was necessary to accurately model the signal shapes. In this modeling procedure, the h boson production cross section and the branching ratios were separated from the shape parameters, which were set to unity. To guarantee continuity across the parameter space, each individual fit parameter was interpolated separately using thin-plate spline methodology, with zero regularization to ensure accurate representation at all simulated mass points.

Statistical Framework and Limit Setting

Experimental constraints on $\sigma(pph) \times \mathcal{B}(hZa4\ell)$ were established through a rigorous statistical framework using a profile likelihood ratio test that integrates observed

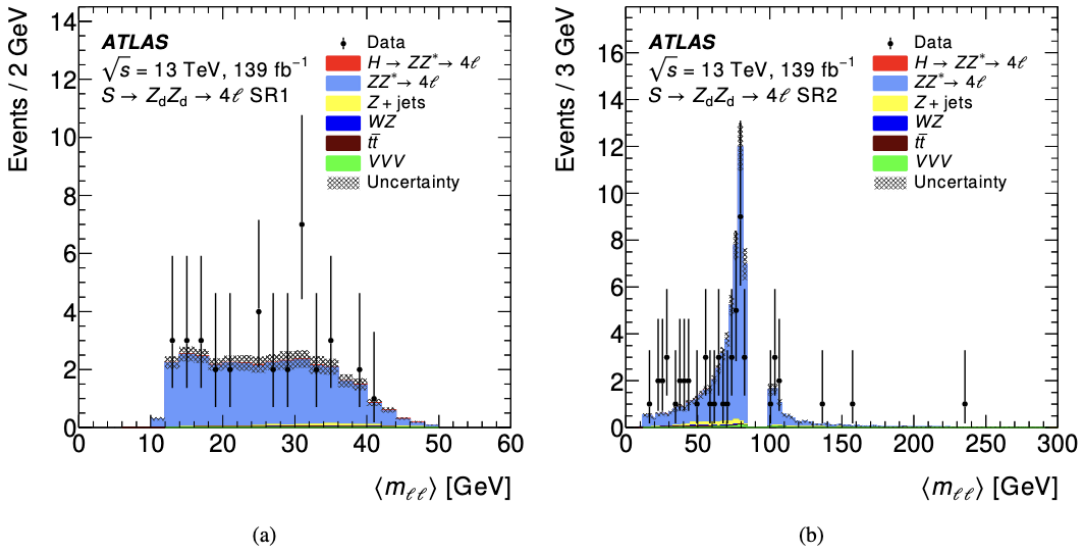


Figure 6.5: Distributions of the average dilepton mass $\langle m_{\ell\ell} \rangle = \frac{1}{2}(m_{ab} + m_{cd})$ for the two signal regions (a) SR1 and (b) SR2. The hatched bands show the uncertainty in the background prediction. The uncertainties on the data points are asymmetric Poisson errors (Eqs. (40.76a) and (40.76b)

event distributions, background predictions and signal models. These components were classified according to $\langle m_{ell\ell} \rangle$ and $m_{4\ell}$. To address resolution limitations, a strategic approach used coarse slicing in the $m_{4\ell}$ dimension while retaining finer granularity (1 GeV intervals) for the variable $\langle m_{\ell\ell} \rangle$. The analysis divided SR1 into eight segments of equal width covering $30 - 110\ GeV$, while SR2 was divided into fourteen uniform intervals covering the range $125 - 825\ GeV$.

When building the signal models, a targeted selection criteria was applied, according to which only simulated events with a pseudoscalar mass m_a within ± 0.5 GeV of the nominal value contributed to the model. The full statistical evaluation was performed via the RooStats framework with HistFactory components, using Monte Carlo pseudo-experiments to properly account for statistical fluctuations and systematic effects.

Results and Statistical Significance Assessment

The full results shown in Figure 6.9 encompass the expected and observed upper

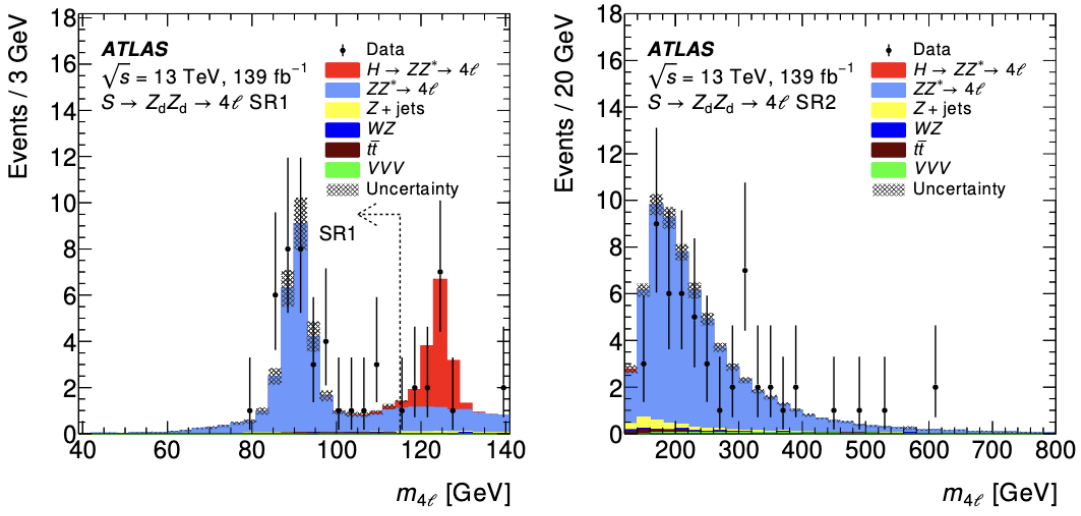


Figure 6.6: Distributions of the total invariant mass $m_{4\ell}$ for the two signal regions (a) SR1 and (b) SR2. In (a), the requirement $m_{4\ell} < 115$ GeV is not applied, but is shown by the arrow. The hatched bands show the uncertainty in the background prediction; however, in (b), background uncertainties are not shown for $m_{4\ell} > 115$ GeV. The uncertainties on the data points are asymmetric Poisson errors (Eqs. (40.76a) and (40.76b)

limits at the 95% confidence level of the effective production cross-section multiplied by the branching ratio, plotted against the coordinates (m_h, m_a). These graphs also show the correlation between observed and expected limits, with the SR2 figures clearly marking the regions excluded by the Z boson veto criterion.
Statistical analysis revealed localized excesses characterized by minimum p_0 values() at $(m_h, m_a) = (110\text{ GeV}, 30\text{ GeV})$ in SR1 and $(350\text{ GeV}, 75\text{ GeV})$ in SR2, corresponding to local statistical significances of 2.7 and 2.8 respectively. When properly adjusted for the look-elsewhere effect using specific Monte Carlo studies, the SR2 excess decreases considerably to an overall significance of just 0.5.
A further investigation of the SR1 discrepancy involved an improved methodology with a finer two-dimensional scan in the $(m_{4\ell}, \langle m_\ell \rangle)$ plane, using a binning scheme of 2 GeV $\times$ $1GeV$ within a window centered on the signal. This refined approach confirmed a local significance of 2.7, but at the slightly shifted mass point $(109\text{ GeV}, 31\text{ GeV})$. After correction this significance is reduced to 1.6.

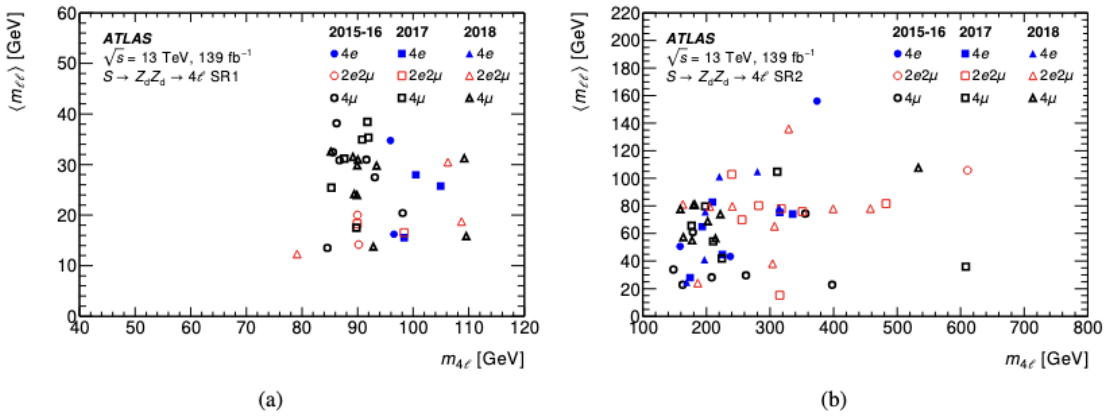


Figure 6.7: Events selected in signal regions (a) SR1 and (b) SR2, represented in the $(m_{4\ell}, \langle m_{\ell\ell}\rangle)$ plane. The points are differentiated by final state ($4e$, $2e2\mu$, and 4μ) and by data-taking period (2015–2016, 2017, and 2018).

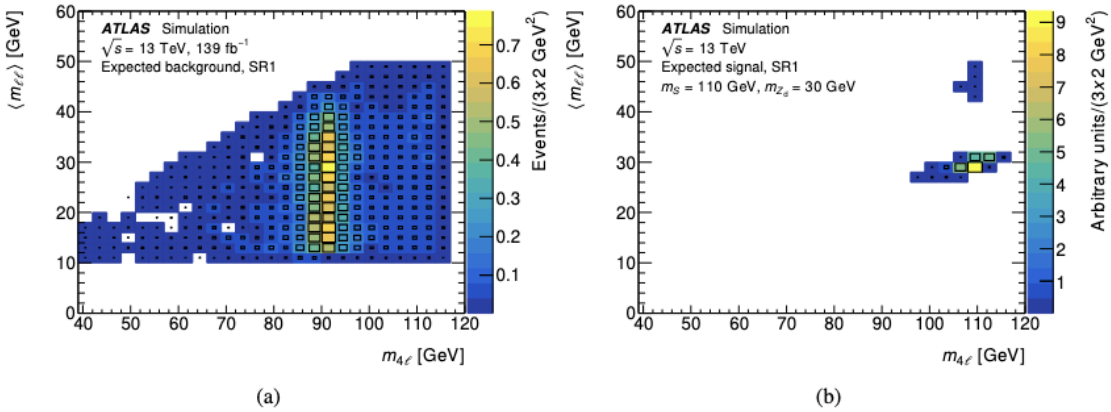


Figure 6.8: (a) Estimated background and (b) expected signal shape for $(m_S, m_{Z_d}) = (110\ \text{GeV}, 30\ \text{GeV})$ in SR1 in the $(m_{4\ell}, \langle m_{\ell\ell}\rangle)$ plane, using both histograms and box representations. The signal normalization is arbitrary.

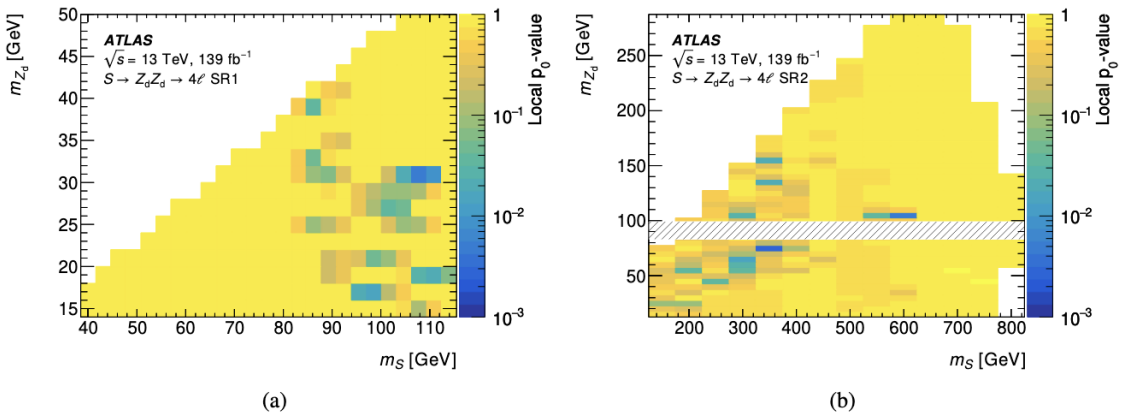


Figure 6.9: Local p_0-values in the $(m_{4\ell}, \langle m_{\ell\ell} \rangle)$ plane for (a) SR1 and (b) SR2, evaluated in slices in $m_{4\ell}$. The horizontal band in the SR2 figure shows the region excluded by the Z boson veto requirement, $|m_{ab,cd} - m_Z| > 8$ GeV.

7

Search for Dark Vector Bosons and New Scalars in ZdZd→2l2j Final State

This chapter presents a search for dark vector bosons and additional scalar particles in the two-lepton, two-jet final state. The analysis is motivated by the channel's higher branching ratio, despite the increased background contamination.
Signal events are selected and reconstructed using a TMVA-based Boosted Decision Tree (BDT), which significantly enhances background suppression.
A detailed truth-level study is conducted, with results evaluated across multiple mass points. Different jet-pairing strategies are investigated to optimize signal reconstruction efficiency. Key kinematic variables distinguishing signal from background are analyzed, and statistical-only exclusion limits are derived.
This search plays a vital role in the combined interpretation of multiple channels, improving sensitivity in future dark sector signature searches.

7.1 Analysis overview

The following analysis presents a search for dark vector bosons (Z_d) produced in pairs either via the decay of the Standard Model (SM) Higgs boson or a new heavy scalar, with one Z_d decaying leptonically and the other hadronically, resulting in a final state with two leptons and two jets (2ℓ2j). The research uses pp collision data collected by the ATLAS detector at the Large Hadron Collider (LHC), giving an integrated luminosity of 139 fb^{-1} at a center-of-mass energy of $\sqrt{s} = 13$ TeV.
The dark vector bosons appear in many theoretical applications of the SM model that include hidden or dark sectors, which may potentially address fundamental questions such as the nature of dark matter. These models will introduce a new U(1) gauge symmetry with an associated gauge boson, usually called a dark photon or Z_d, which can interact with SM particles by kinetic mixing with the SM hypercharge boson. The 2ℓ2j final state provides several potential results for this research:

- Improved branching fraction: Compared with the 4ℓ final state, the semileptonic decay mode has a significantly larger branching fraction due to the higher hadronic decay probability of Z_d.
- Distinctive signature: The presence of two leptons provides a clearer experimental signature than fully hadronic channels, enabling efficient triggering and background rejection.
- Mass reconstruction: Both leptonic and hadronic Z_d candidates can be fully reconstructed, enabling precise measurements of Z_d mass and parent scalar properties.

The analysis targets two main production scenarios:

- Higgs SM decays: $h \to Z_d Z_d \to 2\ell 2j$, where h is the 125 GeV SM Higgs boson. This makes it possible to probe the Higgs portal to the dark sectors with relatively light Z_d bosons.
- Heavy scalar decays: $S \to Z_d Z_d \to 2\ell 2j$, where S is a new scalar with mass $m_S > 125\ GeV$ or$m_S < 125\ GeV$. This scenario explores extended scalar sectors that could be connected to dark sectors.

This analysis complements earlier searches for dark photons in all-lepton channels and extends sensitivity to regions of parameter space where the Z_d has significant branching fractions towards quarks. These results provide an interpretation in the context of various theoretical frameworks, including the hidden abelian Higgs model and the dark SUSY scenario, by placing constraints on the kinetic mixing parameter ϵ and the masses of the Z_d and the parent scalar particles.

7.2 Data and Monte Carlo Samples

7.2.1 LHC dataset

The analysis is based on data from proton-proton collisions collected with the ATLAS detector at the LHC. The data set corresponds to an integrated luminosity of 139 fb^{-1} at a center-of-mass energy of $\sqrt{s} = 13$ TeV as mentioned previously with events selected using single lepton and dilepton triggers to ensure high efficiency for the targeted $2\ell 2j$ final state. Data quality requirements follow standard ATLAS recommendations to ensure optimum detector performance throughout the data-taking period.

7.2.2 Monte Carlo Samples

Monte Carlo (MC) simulations have been used to modulate the signal and background processes. Signal samples are generated using `MadGraph5` interfaced with `Pythia8`, implementing the hidden abelian Higgs model. Predominant signal production mode is gluon-gluon fusion, and Z_d bosons can decay into leptons or jets, with emphasis on light-flavored jets (u, c, b, s) and electrons or muons in the final state.

The following background processes are taken into account in this analysis:

- $Z \to \ell\ell$ + jets,
- $t\bar{t}$ and single vertex,
- Production of dibosons (ZZ, ZW, WW).

All MC samples are processed by a full simulation of the ATLAS detector and reconstructed using the same algorithms applied to the data. The normalization of simulated samples is based on the most accurate theoretical cross sections available [91].

7.3 Event selection and reconstruction

Event selection for the $Z_dZ_d \to 2\ell 2j$ search is designed to maximize signal acceptance while removing substantial backgrounds from the SM. Indeed, the selection strategy follows a tiered approach, beginning with object-level requirements, then event preselection, and concluding with the formation and selection of $2\ell 2j$ quadruplets that are potential candidates for signals.

7.3.1 Event Preselection

Pre-selecting events for $Z_dZ_d \to 2\ell 2j$ analysis lays the foundations for identifying candidate signals, while removing background interference from the SM. Preselection begins with the definition of the target signal region and base object requirements, as shown in Table 7.1.

Parameter	**Criteria**	**Signal Region**
Mass range	m	20 GeV $< m_{Z_d} <$ 55 GeV 70 GeV $< m_S <$ 110 GeV
Baseline electrons	p_T η ID QQ $z_0 \sin\theta$	$p_T > 7$ GeV $\lvert\eta\rvert < 2.47$ Medium ID Not from a bad cluster $z_0 \sin\theta < 0.5$ mm
Baseline muons	p_T η ID $z_0 \sin\theta$ d_0	$p_T > 5$ GeV (15 GeV if calo-tagged) $\lvert\eta\rvert < 2.7$ Medium ID $z_0 \sin\theta < 0.5$ mm (stand-alone muons exempt) $d_0 < 1$ mm (stand-alone muons exempt)

Table 7.1: Baseline object definitions and mass range requirements.

For electrons, baseline selection requires a minimum transverse momentum of 7 GeV, pseudorapidity in $|\eta| < 2.47$, and fulfillment of the medium ID criteria. The electrons must not come from the wrong calorimeter groups, and must have a longitudinal impact parameter $z_0 \sin\theta < 0.5$ mm which ensures that they are associated with the primary vertex.
Similar quality requirements apply to muons, with a minimum p_T of 5 GeV for standard muons or 15 GeV for calorimeter-labeled muons, and a pseudorapidity $|\eta| < 2.7$. The muons must meet medium ID and impact parameter requirements, with exemptions granted for stand-alone muons.

7.3.2 Truth Study for Jet Selection

To optimize jet selection for the $Z_dZ_d \to 2\ell 2j$ analysis, truth-level studies were performed with simulated signal samples. These studies have focused on identifying the most efficient strategy for selecting the pair of jets likely to come from the decay of a Z_d boson.

The major challenge in the $2\ell 2j$ end state is to match the jets correctly, as a mismatch can significantly damage the mass resolution and hence the sensitivity of the search. Truth studies have examined various algorithms for jet pairing, including :

a. **Minimum Invariant Mass Difference:**
This approach explores the minimum invariant mass difference between the dileptons (2) and dijets (2j). It effectively addresses the fundamental challenge posed by $Z_d Z_d$ particles, which share identical mass values in the signal model. By selecting jet pairs whose invariant mass closely matches the dilepton invariant mass, this method ensures consistency between the reconstructed masses of both Z_d candidates.
The mathematical formulation involves minimizing $|\Delta m| = |m_{\ell\ell} - m_{jj}|$ across all possible jet pair combinations. This approach leverages the expected mass symmetry of the two Z_d bosons in the signal model.

b. **Leading p_T Jets Selection:**
This more straightforward method focuses on selecting the jets with the highest transverse momentum in each event. The leading and sub-leading jets (ranked by p_T) are used to reconstruct the dijet invariant mass (m_{jj}). This approach is simpler but relies on the assumption that jets from Z_d decay typically have higher p_T than jets from other sources, which may not always be true, especially in lower mass signal regions.

c. **Boosted Decision Tree (BDT) Analysis:**
The TMVA method combines several discriminating variables into one final discriminator, achieving better separation between signal and background than using any single variable alone. This approach also makes correlations between variables visible and exploitable for improved jet selection.
Variables considered in the multivariate analysis likely include kinematic properties (such as jet p_T, η, and ϕ), angular correlations between jets and leptons, and mass-related variables that exploit the expected mass relationships in signal events.

TMVA Training Details
For this analysis, the jet pairs used in BDT training were preselected on the basis of a selection based on minDetaR between quaks and jets , which is a physics-motivated starting point. To improve the efficiency of the BDT algorithm, a complete evaluation of the kinematic variables was carried out. This

process involved identifying the most effective predictors for optimizing background rejection while maintaining high signal efficiency.
Analysis of the significance variables revealed a clear hierarchy of discriminating features. The most powerful variables for distinguishing signal from background are :

(a) $m_{\ell\ell}$ (dilepton invariant mass): $9.751e^{-01}$

(b) m_{jj} (dijet invariant mass): 3.956e-01

(c) $m_{jj\ell\ell}$ (four-body invariant mass): $3.788e^{-01}$

(d) $\Delta\eta_{jj}$ (pseudorapidity separation between jets): $2.885e^{-01}$

(e) $\eta_{\ell\ell}$ (pseudorapidity of dilepton system): $2.302e^{-01}$

(f) $p_{T_{\ell\ell}}$ (transverse momentum of dilepton system): $2.178e^{-01}$

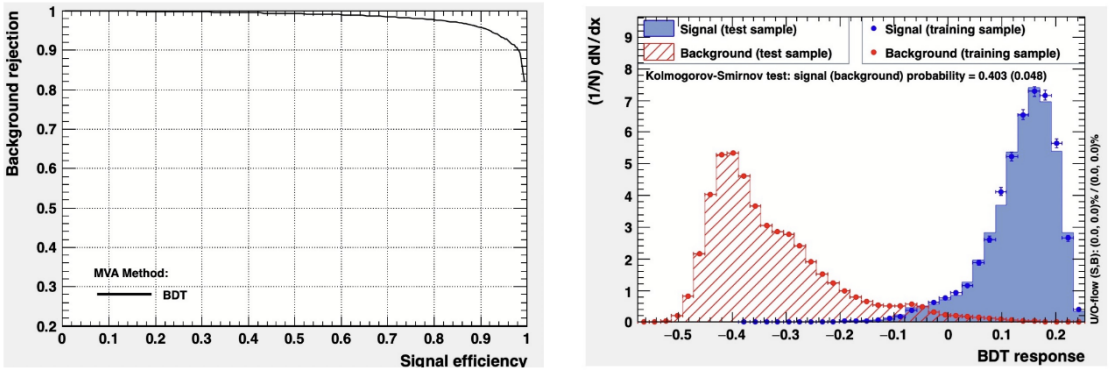
Additional variables with significant discriminating power include angular correlations between jets and leptons ($\Delta\phi_{jj}$, $\Delta\phi_{\ell\ell}$), transverse momentum variables, and various combinations of kinematic properties.
The BDT's performance was evaluated using its curve of background rejection versus signal efficiency, demonstrating excellent discrimination capability. The BDT response distribution showed a clear separation between signal events (predominantly scoring positively) and background events (mainly scoring negatively), confirming the algorithm's effectiveness.

Performance and Validation The BDT's performance was evaluated using its curve of background rejection versus signal efficiency, Figure 7.1a, demonstrating excellent discrimination capability. in Figure 7.1b, the BDT response distribution showed a clear separation between signal events (predominantly scoring positively) and background events (mainly scoring negatively), confirming the algorithm's effectiveness.

d. Jets Pairing Performance Comparison:

Three distinct approaches for jet pairing were evaluated across $20 < (m_{Z_d} < 55, 70 < m_S < 110)$ mass points, as showen in Figure 7.2:

- **BDT-based jet-pairing:** The efficiency was consistently high, ranging from around 80% to 90% for all mass points, with maximum performance of around 90% for the mass point (40, 95).



(a) (b)

Figure 7.1: (a) represent the Background Rejection versus Signal Efficiency for BDT Classifier, while (b) show the BDT Response Distribution for Signal and Background Samples.

- **Minimizing $|m_{\ell\ell} - m_{jj}|$:** Shows performance comparable to that of the BDT method, with efficiency generally 5-10% lower, but reaching almost equivalent performance for certain mass points such as (35, 95) and (50, 110).
- **Selecting two highest-p_T jets:** Efficiency was significantly lower, ranging from 45% to 65%, confirming that this simple approach is not optimal for this analysis.

For these comparisons, efficiency was defined as the percentage of events with $|m_{\ell\ell} - m_{jj}| < 50$ GeV, representing the success rate in correctly identifying jet pairs from Z_d decay.
Both the BDT-based approach and the method based on minimization of $|m_{\ell\ell} - m_{jj}|$ proved highly effective in selecting the correct pair of jets. While the BDT approach offered marginally better efficiency, the mass difference-based method delivered comparable results with lower computational complexity.

7.3.3 Leptons Selection

Lepton selection in the $2\ell 2j$ final-state analysis follows the same requirements as those established in the 4ℓ analysis to ensure optimum signal coherence and efficiency. Each lepton in the quadruplet has to pass the isolation cuts, with FCLoose applied for electrons [84] and $FCLoose_FixedRad$ for muons [85], including proximity

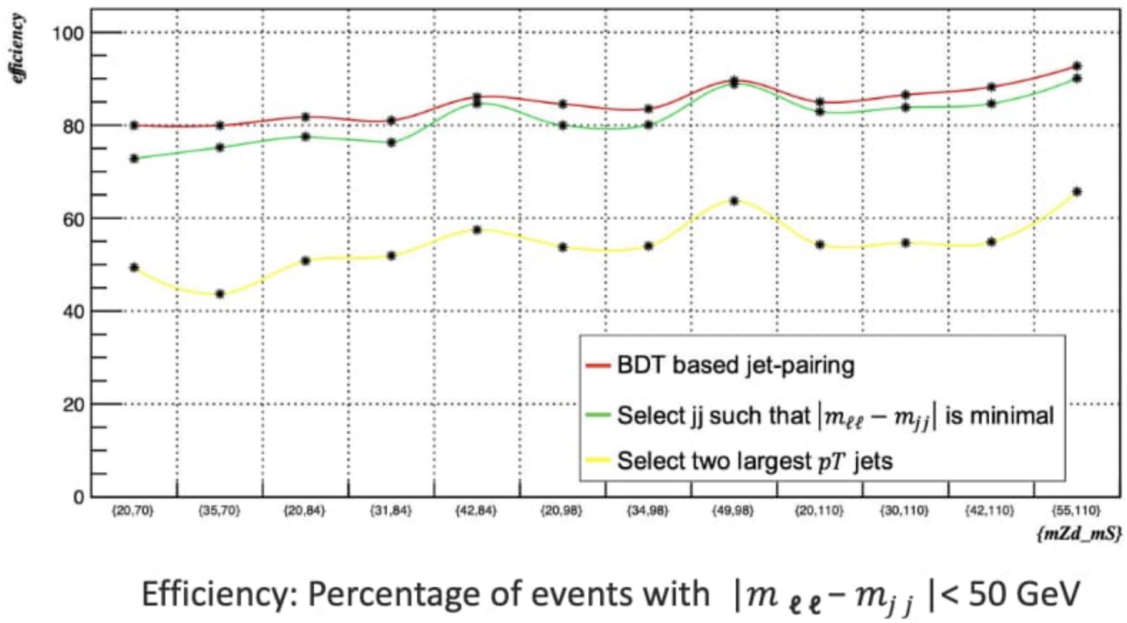


Figure 7.2: Efficiency of Jet Pairing Methods as a Function of (m_{Z_d}, m_S) Mass Points in $Z_d Z_d \to 2\ell 2j$ Events

corrections to account for the presence of other leptons in the event. Moreover, all electrons must satisfy the Loose likelihood identification criteria.
Regarding impact parameter requirements, the impact parameter magnitude across the beam line, $|d_0^{\mathrm{BL}}|/\sigma$, must be less than 3 for muons and less than 5 for electrons; this does not apply to stand-alone muons, since they do not have an inner detection track.
The isolation is implemented using calorimeter- and track-based variables. The calorimeter isolation variable, E_T^{cone20}, sums the energy in a cone of $\Delta R = 0.2$ around the lepton, and the tracks' isolation variables sum the transverse moments of the tracks within a cone of variable size, with corrections applied to effect the removal of contributions from other leptons in the event. The specific isolation thresholds are $E_T^{\mathrm{cone20}}/p_T < 0.2$ and $p_T^{\mathrm{cone20}}/p_T < 0.15$ for FCLoose, and $E_T^{\mathrm{cone20}}/p_T < 0.3$ and $\max(p_T^{\mathrm{cone30}}/p_T, p_T^{\mathrm{cone20}}{}_{\mathrm{TTVA}}/p_T) < 0.15$ for FCLoose$_{F}ixedRad$
$Kinematicrequirementsalsoincludetheleadingleptonhaving\mathrm{p}_{T,\ell_1}$ >20 GeV and the sub-leading lepton p_{T,ℓ_2} >15 GeV, as indicated in the summary of selection criteria in Tbale 7.2.
The efficiency of these lepton selection criteria was investigated as a function of

(m_{Z_d}, m_S), with the results presented in the efficiency graph, Figure 7.3. The difference between loose and medium identification, as well as between the thresholds $p_T > 15$ GeV and $p_T > 20$ GeV, is minimal, confirming that the chosen selection delivers robust performance.

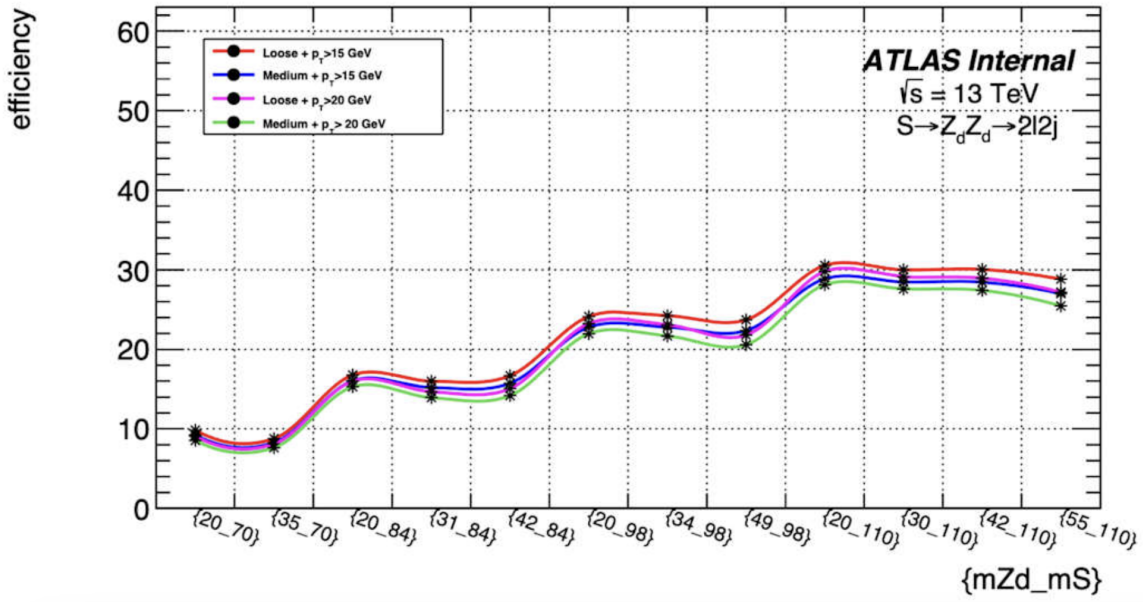


Figure 7.3: Lepton selection efficiency as a function of (m_{Z_d}, m_S) for different identification and p_T thresholds.

7.3.4 Jets Selection

For $Z_dZ_d \to 2\ell 2j$ analysis, jets represent a critical element of the final state, necessitating careful selection to optimise signal sensitivity. Those criteria have been adapted to the characteristics of the expected signal and the ability to reject background.
The jets are reconstructed applying the anti-k_t algorithm with a radius parameter of $R = 0.4$, as applied to the topological energy clusters in the calorimeter. This analysis is based on the following kinematic requirements for the jets:

- Transverse momentum: $p_T > 15$ GeV
- Pseudorapidity range: $|\eta|$ <4.5

These relatively flexible kinematic requirements ensure high acceptance of signal events over a wide Z_d mass range, which is particularly important for lower-mass region where decay events may have low momentum.
Following the initial identification of jets meeting these criteria, the selection of the specific pair of jets assigned to the Z_d decay is carried out using the algorithm identified as optimum in the truth study outlined in section 8.3.2. Specifically, both of the jets required to form the quadruplet $2\ell 2j$ are selected by minimizing $|m_{ell} - m_{jj}|$ with order p_T. This approach exploits the fundamental signal topology feature: the two Z_d bosons should have identical masses, which results in similar invariant masses for the dilepton and dijet systems.
Following the initial identification of jets meeting these criteria, the selection of the specific pair of jets assigned to the Z_d decay is carried out using the algorithm identified as optimum in the truth study outlined in section 8.3.2. Specifically, both of the jets required to form the quadruplet $2\ell 2j$ are selected by minimizing $|m_{ell} - m_{jj}|$ with order p_T. This approach exploits the fundamental signal topology feature: the two Z_d bosons should have identical masses, which results in similar invariant masses for the dilepton and dijet systems.
In events with more than two jets passing the selection criteria, all the possible jet pairings are evaluated, and the pair that minimizes the absolute difference between the dilepton and dijet invariant masses is selected. If several jet pairs give similar mass differences, then the higher jet pair (p_T) is preferred, since energy jets are more likely to come from the decay of a massive particle than from additional QCD radiation.
In order to reduce contamination from pile-up, jets with $p_T < 60$ GeV and $|\eta| < 2.4$ should satisfy the jet vertex tagger (JVT) requirement at the average working point. This guarantees that the selected jets originate from the primary vertex instead of additional proton-proton interactions in the same cluster crossing or in nearby cluster overlaps.
Combining these selection criteria guarantees optimum jet matching efficiency while maintaining high signal acceptance, especially in the targeted mass range of $20 < m_{Z_d} < 55$ GeV. This approach, in combination with the lepton selection described in the previous section, forms the basis for the construction of the $2\ell 2j$ quadruplet essential for this analysis.

7.3.5 Kinematic Variables and Event Selection Framework

Kinematic requirements for the $Z_d Z_d \to 2\ell 2j$ analysis plays a crucial factor in the definition of the signal region and in maximizing sensitivity to potential dark vector

boson signals. Such requirements, detailed in Table 7.2, may be classified in various groups depending on their physical motivation and the topological constraints of the event.

. **Topological Requirements**
To ensure good object separation and clean event reconstruction, angular separation is required:

  – $DeltaR > 0.1$ between same-flavor leptons, avoiding merged lepton

  – $DeltaR > 0.2$ between jets, assuring $well - resolved$ hadronic energy deposits

  – $DeltaR > 0.4$ between jets and leptons, minimizing lepton isolation contamination by nearby jets

. **Invariant Mass Criteria**
Several mass requirements aim the specific mass ranges of the dark vector bosons and the parent scalar:

  – LooseSR: dilepton and dijet systems must have invariant masses above 20 GeV ($m_{ell} > 20$ GeV and $m_{jj} > 20$ GeV), thereby rejecting low-mass resonances and reducing combiner backgrounds.

  – Veto H: Four-body invariant mass must be less than 115 GeV ($m_{jj} < 115\,GeV$), which concentrates the search on scalar particles lighter than the Higgs boson SM.

  – ZVeto: $m_{ell\ell}$ and m_{jj} must be less than 60 GeV, thereby suppressing the background caused by the production of Z bosons at the shell. This is coherent with the target signal region where the dark vector boson mass is between 20 and 55 GeV.

. **Dynamic Ratio and Missing Energy**
Two further kinematic conditions offer powerful discrimination of background:

  – Missing energy constraint: The missing transverse momentum should be relatively small with $p_{T,met}$ <50 GeV. With this condition, backgrounds with true missing energy from neutrinos (such as $t\bar{t}$ and $W+$ jets), are rejected.

– Mass ratio requirement: The invariant mass ratio of dileptons and dijets must satisfy $0.5 < m_{ell}/m_{jj} < 1.1764$. This requirement is based on a fundamental feature of the signal: the two Z_d bosons have identical masses, which implies that their decay products must have similar invariant masses. it is particularly useful for rejecting backgrounds where the dilepton and dijet systems originate from background.

These kinematics requirements define a region in phase space optimized for the detection of dark vector bosons with masses between 20 and 55 GeV, generated from scalar parents with masses between 70 and 110 GeV. Precise adjustment of these thresholds balances signal acceptance and background rejection, offering maximum sensitivity to targeted physical signatures.

7.4 Background composition

Precise modelling of background processes is fundamental to the search of dark vector bosons and new scalars in the $Z_d Z_d \to 2\ell 2j$ final state. Main backgrounds arise from SM processes that generate final states with two leptons and two jets, either directly or by misidentification. An understanding of these backgrounds is essential for optimizing the analysis strategy and interpreting any signal appropriately.

7.4.1 Irreducible Backgrounds

Irreducible backgrounds produce final states which can't be separated from the signal on the detector level. For the $2\ell\,2j$ analysis, these are :

- $Z \to \ell\ell$ **+ jets:** This process represents the dominant irreducible background, where a Z boson decays into a pair of leptons in association with jets from the initial-state emission. The dilepton invariant mass typically peaks at the mass of the Z boson ($\sim$91 GeV), which is generally higher than the Z_d target mass range that we are targetting. However, the large production cross-section makes this background significant even after applying the mass window requirements.

- **Diboson production:** Processes such as WW, WZ and ZZ may produce final states with two leptons plus hadronic activity. Specifically, $ZZ \to 2\ell\,2q$ can closely imitate the signal topology when the invariant masses of the two candidate bosons lie in the signal region. While these processes have smaller

	cuts	**Signal Region**
Mass range	m	20 GeV $< m_{Z_d} <$ 55 GeV
		70 GeV $< m_S <$ 110 GeV
Baseline electrons	p_T	$p_T > 7$ GeV
	η	$\|\eta\| < 2.47$
	ID	Medium ID
	QQ	Not from a bad cluster
	$z_0 \sin\theta$	$z_0 \sin\theta < 0.5$ mm
Baseline muons	p_T	$p_T > 5$ GeV (15 GeV if calo-tagged)
	η	$\|\eta\| < 2.7$
	ID	Medium ID
	$z_0 \sin\theta$	$z_0 \sin\theta < 0.5$ mm (stand-alone muons exempt)
	d_0	$d_0 < 1$ mm (stand-alone muons exempt)
Quadruplet formation	Quadruplet	At least one quadruplet formed from two leptons and two jets
	Jets_eventClean	Require jet cleaning
	Overlap removal	Overlap between leptons and jets is applied
	p_T	$p_{Tj1} > 20$ GeV, $p_{Tj2} > 20$ GeV
Quadruplet Selection	p_T	$p_{Tl1} > 20$ GeV and $p_{Tl2} > 15$ GeV
	η	$\eta_j < 4.5$ & $\eta_l < 2.5$
	Trigger matched	Leptons in quadruplet responsible for firing at least one trigger
	ΔR	$\Delta R > 0.1$ between same-flavor leptons, $\Delta R > 0.2$ between jets and $\Delta R > 0.4$ between jets and leptons
	Muon quality	Number of StandAlone or CaloTagged $\mu < 2$
Quadruplet Ranking	Minimal Δm	Select quadruplet with smallest $\Delta m = \|m_{\ell\ell} - m_{jj}\|$
Event Selection	Electron ID	All e in quadruplet pass medium working point
	Isolation	All leptons in quadruplet pass Fixed CutLoose working point ($l_isIsoCloseBy = 3$)
	Electron quality	All leptons medium ID or better
	Impact Parameter	$\|d0BSig\| < 5(3)$ for $e(\mu)$ in quadruplet
	Loose SR	$m_{\ell\ell} > 20$ GeV and $m_{jj} > 20$ GeV
	H Veto	$m_{jjll} < 115$ GeV
	Z Veto	$m_{\mu\mu} < 60$ GeV && $m_{jj} < 60$ GeV
	Met cut	$p_{T,met} < 50$ GeV
	Medium SR	$m_{\ell\ell}/m_{jj} > 0.5$ && $m_{\ell\ell}/m_{jj} < 1.1764$

Table 7.2: Summary of cuts and signal region selections.

cross sections than $Z+$ jets, they contribute to the background due to their similar final-state topology.

- **Single and pair-produced top quarks:** Both the production of pairs of top quarks ($t\bar{t}$) and the production of a single top associated with a W boson may produce two leptons from the leptonic decays of W bosons, alongside jets from the hadronization of b quarks. Such backgrounds are particularly important when b jets have not been identified separately.

7.4.2 Reducible Backgrounds

Reducible backgrounds arise in processes whose final state differs from the signal but may replicate it due to misidentification of the object or an incomplete detector reconstruction:

- $W \to \ell\nu$ **+ jets:** Leptonic W boson decays produced with jets contribute to the background when an additional jet is misidentified as a lepton. This background is reduced through strict lepton identification criteria and isolation requirements.

- **QCD multijet events:** This background appears when jets are misidentified as leptons. Although the probability of misidentifying jets is low, because of the large cross- section of multiple-jet QCD events, this background is potentially significant. It is removed with rigorous lepton quality requirements and is usually estimated using data-driven techniques.

- $Z \to \tau\tau$ **+ jets:** When the two τ leptons disintegrate leptonically, two leptons and jets can be produced. Typically, the presence of neutrinos in *tau* decays results in a missing transverse momentum that is larger than the signal.

7.5 Signal simulation

the signal simulation for the $Z_d Z_d \to 2\ell 2j$ search adopts a global approach to modeling dark vector boson production and decay.

7.5.1 Production Mechanism

The S scalar particle decays into dark vector bosons and is mainly produced by gluon-gluon fusion processes in proton-proton collisions. This mode of production provides the highest cross section at LHC energies among scalar particles in a wide range of masses. At present, the analysis imposes no specific constraints on the mass of the scalar (m_S), making it possible to explore both the mass region of the SM

Higgs boson and new potential scalars at different mass points.
As illustrated in Figure 7.4, the signal process follows the decay chain:
pp→S→ZdZd→$\ell\ell$jj
Feynman's diagram illustrates the coupling of the scalar S to two dark vector bosons

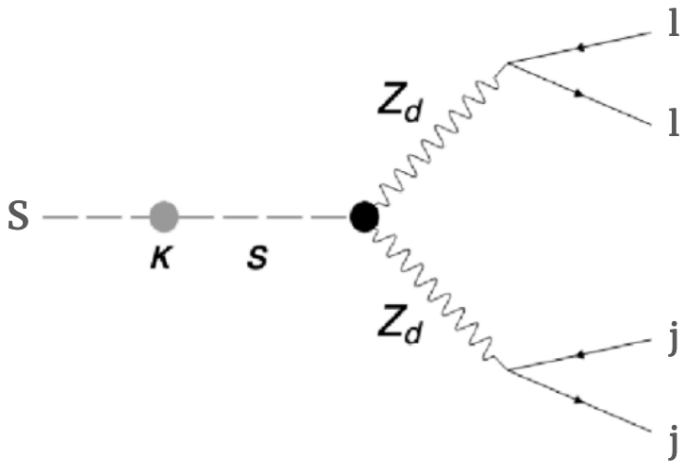


Figure 7.4: Feynman diagram illustrating the signal process: a scalar particle (S) decays into two dark vector bosons (Z_d), with one Z_d decaying leptonically ($\ell\ell$) and the other hadronically (jj).

Z_d through vertexes characterized by the coupling parameters κ and s. Each Z_d subsequently decays into a fermion-antifermion pair, one leptonically and the other hadronically to generate the final $2\ell 2j$ state.

7.5.2 Monte Carlo Generation

The signal samples are produced using MadGraph5 interfaced with Pythia8, using the theoretical framework of the hidden abelian Higgs model.
The model incorporates a dark gauge symmetry $U(1)_d$ that gives rise to the dark vector boson Z_d, providing a coherent framework for calculating production cross sections and decay branching ratios.
The simulation will focus specifically on:

- **Jet flavors**: hadronic decay of Z_d consists of charming quarks (c, $\bar{c}$), lower quarks (b, $\bar{b}$) and light flavors that hadronize into jets.

- **leptons**: electron and muon flavors are the only ones taken into account in Z_d lepton decay.

The choice of these decay products reflects the experimental signature targeted by the analysis, maximizing sensitivity while maintaining reasonable background levels.

7.5.3 Signal Regions Definition

Based on theoretical considerations and detector performance, the study establishes three distinct signal regions in the parameter space (m_S, m_{Z_d}).

- **SR1:**$20 < m_{Z_d} < 50$ GeV and $50 < m_S < 115$ GeV
  it targets scenarios where both the dark vector boson and scalar have relatively low masses, wich Includes the potential of exotic decays of particles lighter than the SM Higgs boson.

- **SR2:**$20 < m_{Z_d} < 58$ GeV and $115 < m_S < 130$ GeV
  Particularly focused on dark vector bosons generated from a scalar with a the Higgs SM boson mass it is sensitive to exotic Higgs decays into dark-sector particles

- **SR3:**$20 < m_{Z_d} < 395$ GeV and $130 < m_S < 800$ GeV
  investigates higher-mass regions where new heavy scalars might decay into dark vector bosons, so it extends the search to a wide range of theories beyond SM with new heavy resonances.

Figure 7.5 displays the distribution of simulated signal points in the (m_S, m_{Z_d}) plane, demonstrating complete coverage of the parameter space. The grid becomes more dense at lower masses where production cross-sections are higher, with progressively more sparse sampling at higher masses. This approach ensures optimum sensitivity across the entire parameter space. These signal regions are analyzed independently using optimized selection criteria for each mass range, where for this study we will be focussing in SR1.

7.6 Background Estimation Strategy

The estimation strategy for these backgrounds employs a combination of Monte Carlo simulations and data-driven techniques:

- **Monte Carlo simulation:** Mainly irreducible backgrounds are estimated using Monte Carlo simulations normalized to theoretical cross sections, along with corrections applied in order to accommodate lepton identification efficiency differences between data and simulations.

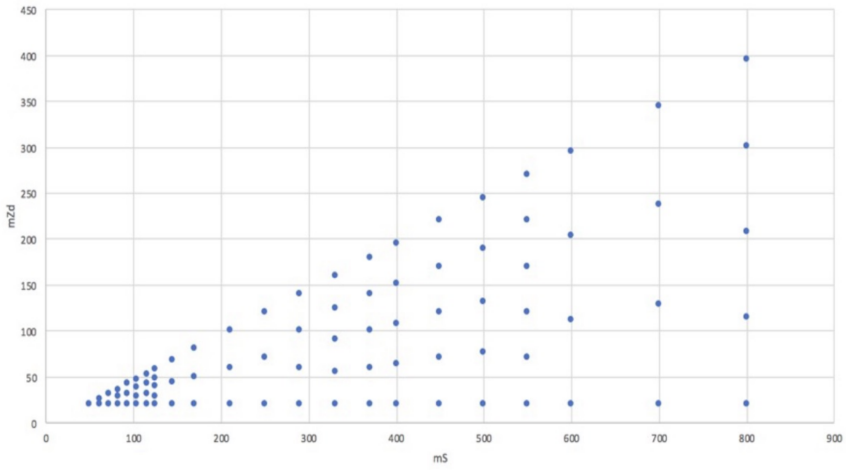


Figure 7.5: Scatter plot of simulated mass points in the (m_S, m_{Z_d}) plane, showing the range of scalar and dark vector boson masses probed in the analysis.

- **Control regions:** Control regions dedicated to specific background processes are defined to validate the background modeling and enforce their normalizations. For example, a control region with a dilepton invariant mass close to the mass of the Z boson is used to impose limits on the background of $Z+$ jets.
- **Data-driven methods:** For backgrounds that involve misidentified objects, such as jets misidentified as leptons, data-driven techniques are used. Such methods measure the likelihood of object misidentification in control regions and apply it to estimate background contributions in the signal region.

Both simulation and background estimation follow the methodologies established in previous ATLAS analyses, with updated software and extended data sets.

7.7 Event yields and Kinematic distributions

The cutflow table (Tableau reftab:finalcutflow) outlines the event selection process for the $Z_d Z_d \to 2\ell 2j$ analysis, providing details of the reduction in the number of events as each selection criterion is applied. The table specifically follows the selection efficiency for a signal reference point with $m_S = 110$ GeV for different m_{Z_d}, showing results separately for the electron channel (2e2j), the muon channel (22j), and their combination.
Following application of the full sequence of selection parameters, the event sample resulting from the $S \to Z_d \to 2\ell 2j$ analysis shows clear topological signal charac-

teristics. Distribution of the m_{ell}/m_{jj} ratio, presented in the Figure 7.6, shows a pronounced peak close to unity for all simulated signal samples with $m_S = 110$ GeV and m_{Z_d} values of 20, 30, 42 and 55 GeV, mirroring the expectations that the two Z_d bosons have the same mass and thereby produce dilepton and dijet systems with similar invariant masses. Meanwhile, the Standard Model background - comprising $Z+$ jets, $W+$ jets and top plus diboson processes - exhibits a larger, flatter distribution, with significant contributions out from the signal region, highlighting the discriminative power . The two- and three-dimensional distributions of m_{ell} as a function of m_{jj}, presented in the Figure 7.7 and Figure 7.8, provide a better illustration of the kinematic signature of the signal: events cluster closely around the point where the two invariant masses are equal to the real mass Z_d, leading to a localized, prominent peak.

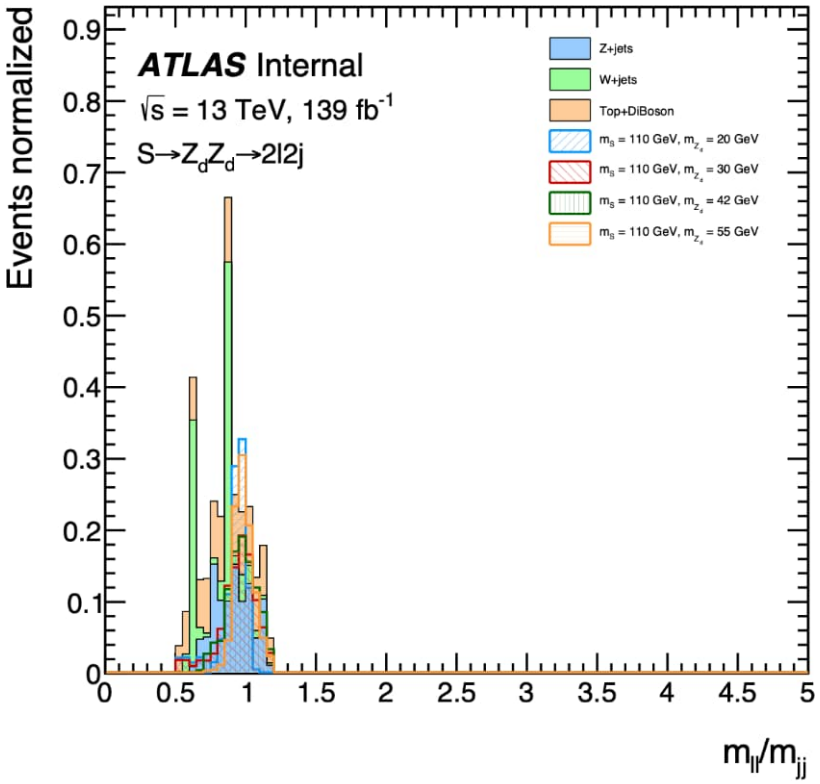


Figure 7.6: Normalized distribution of the mass ratio $m_{\ell\ell}/m_{jj}$ for background processes (Z+jets, W+jets, Top+Diboson) and $S \to Z_d Z_d \to 2\ell 2j$ signal samples with $m_S = 110$ GeV and $m_{Z_d} = 20, 30, 42, 55$ GeV.

Selection	$(m_S, m_{Z_d}) = (110, 30)$		All
	2e2j	2m2j	
All	60000.000	60000.000	60000.000
Overlap Event	60000.000	60000.000	60000.000
Cleaning	60000.000	60000.000	60000.000
Primary Vertex	59891.924	59891.924	59891.924
Jets event Clean	59845.832	59845.832	59845.832
Trigger	21196.917	21196.917	21196.917
make Quadruplet	3400.107	10229.631	13629.738
Overlap removal	3270.046	7013.509	10283.554
Kinematic	1027.183	1276.260	2303.443
Trigger Matched	1024.102	1208.911	2233.013
DeltaR	1023.067	1205.800	2228.867
Lepton quality	886.479	1195.261	2081.740
Muon quality	886.479	1195.261	2081.740
Isolation	786.709	1135.444	1922.154
Impact Parameter	786.709	1119.099	1905.809
Impact Parameter Z	780.422	1116.989	1897.411
Impact Parameter D	780.422	1116.989	1897.411
H Veto	145.024	272.998	418.023
Z Veto	123.829	215.212	339.041
Loose SR	122.794	210.062	332.856
Met Cut	105.599	179.203	284.803
Medium SR	95.179	161.715	256.893
Final	95.179	161.715	256.893

Table 7.3: Cutflow for $(m_S, m_{Z_d}) = (110, 50)$ showing the number of events passing each selection criterion for the 2e2j and 2m2j channels, as well as the total.

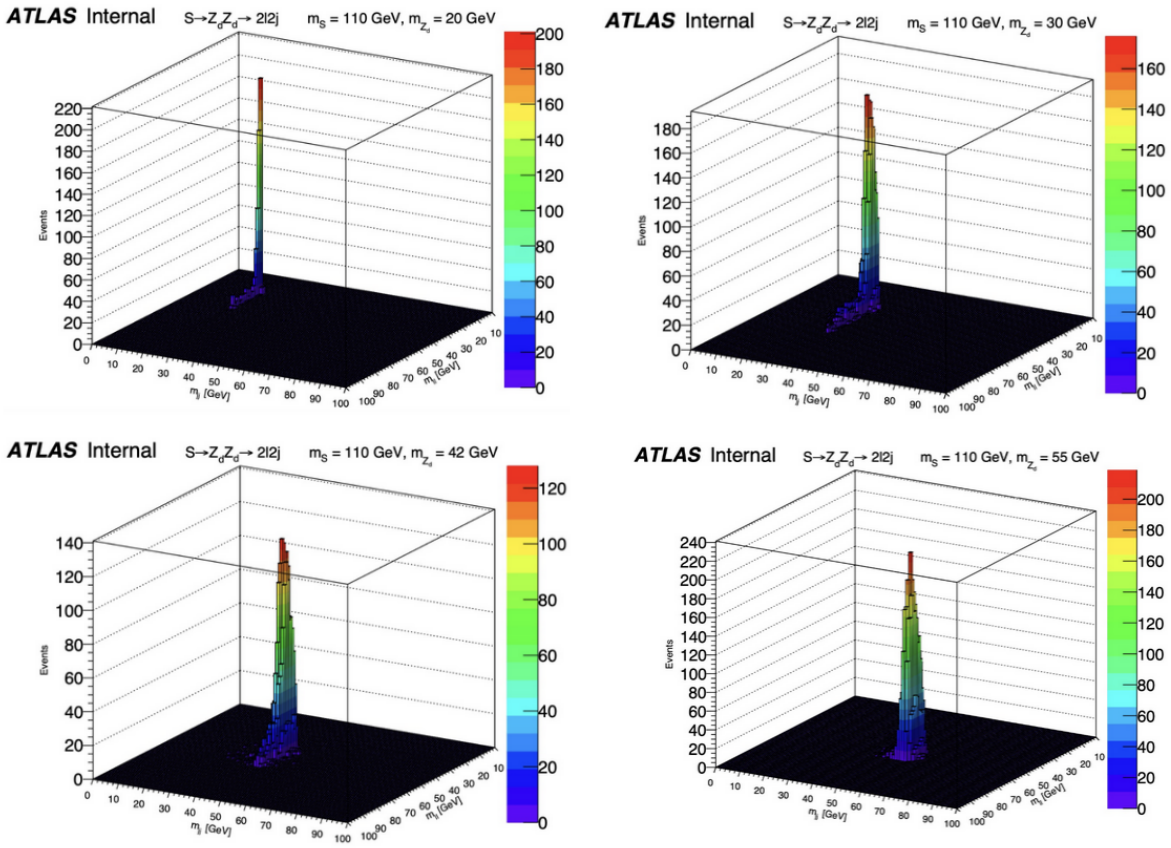


Figure 7.7: Three-dimensional distributions of $m_{\ell\ell}$ versus m_{jj} for $S \to Z_d Z_d \to 2\ell 2j$ signal events, for $m_S = 110$ GeV and $m_{Z_d} = 20, 30, 42, 55$ GeV. The prominent peaks demonstrate the strong correlation between the dilepton and dijet masses, both centered around the Z_d mass.

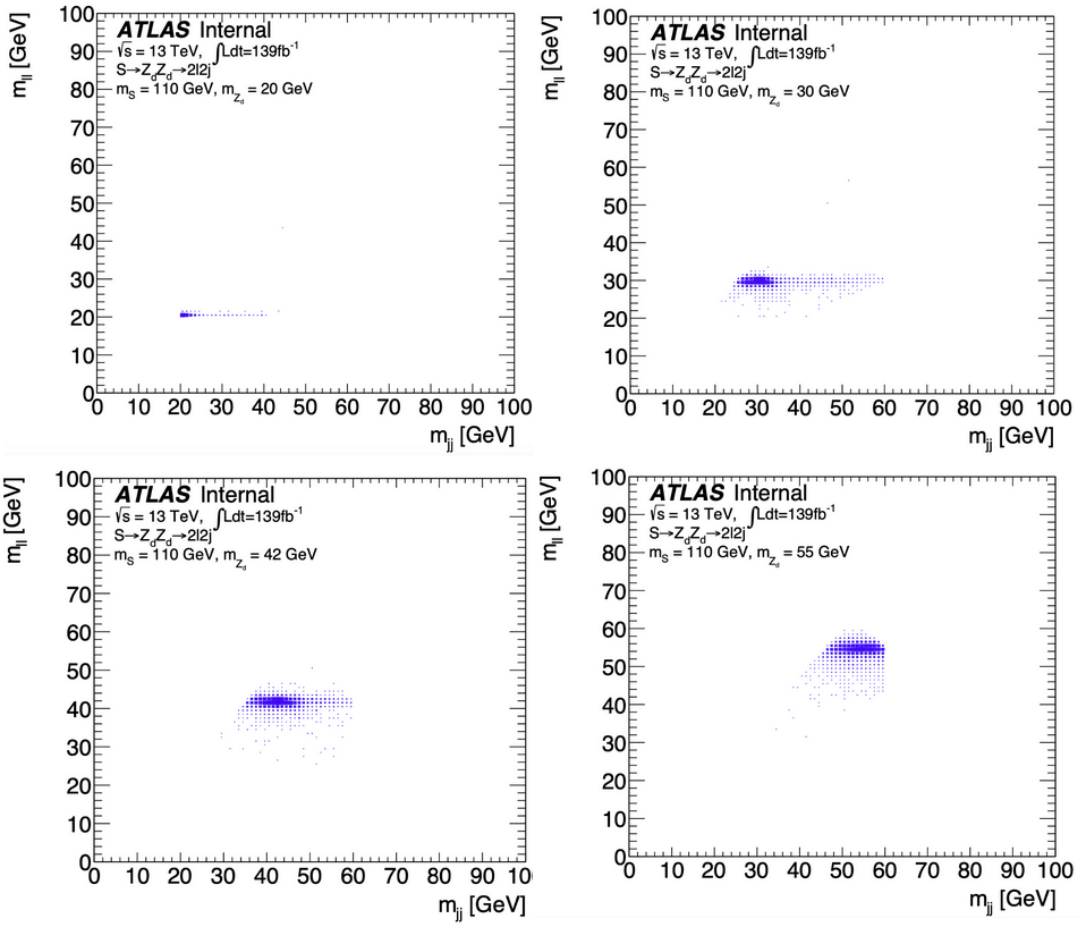


Figure 7.8: Distribution of the dilepton invariant mass ($m_{\ell\ell}$) versus dijet invariant mass (m_{jj}) for simulated $S \to Z_d Z_d \to 2\ell 2j$ signal samples with $m_S = 110$ GeV and $m_{Z_d} = 20, 30, 42, 55$ GeV. Each panel shows the characteristic clustering of events around the true Z_d mass for different mass hypotheses.

Conclusions and Future Work

This thesis, structured across eight chapters, presents a comprehensive investigation into the search for dark vector bosons and new scalar particles at the ATLAS experiment. It is motivated by the well-known limitations of the Standard Model and the mounting theoretical and observational evidence pointing toward physics beyond it. The work brings together both theoretical context and experimental advancements, beginning with a review of the Standard Model, its extensions—including the hidden Abelian Higgs model—and the phenomenology of dark sectors. The experimental chapters detail the ATLAS detector, recent upgrades, and the advanced reconstruction techniques essential for the precise identification of leptons and jets.

A substantial part of this study is devoted to the development, implementation, and validation of analysis strategies for two complementary final states: the fully leptonic (ZdZd $\to 4\ell$) and the semileptonic (ZdZd $\to 2\ell 2$j) decay channels. For each channel, meticulous event selection, background modeling, and signal simulation were conducted using state-of-the-art Monte Carlo tools and data-driven techniques. Optimized kinematic and topological variables, alongside multivariate methods, were employed to enhance sensitivity to potential new physics signals while efficiently suppressing Standard Model background contributions.

The detector performance studies performed as part of this research provide critical insights for future ATLAS operations. In particular, measurements of jet energy scale and resolution involving the High-Granularity Timing Detector (HGTD) demonstrated its remarkable capabilities, especially in the forward region ($2.4 < \eta < 4.0$), thanks to its 30 ps time resolution. These measurements confirmed that resolution improves with increasing transverse momentum, with distinct behavior across η regions. Such precision enables effective rejection of out-of-time pileup contributions, improving the reconstruction of jets and other physics objects. This has direct implications for analyses like ZdZd $\to 2\ell 2$j, where accurate jet reconstruction significantly impacts signal sensitivity.

In addition, thermal performance studies of the ITk-band modules conducted at Brookhaven National Laboratory confirmed the readiness of ATLAS components for

upcoming data acquisition periods. These technical investigations provide an essential baseline for the physics analyses discussed in the subsequent chapters.

Although no statistically significant excess above the Standard Model expectations was observed in the explored parameter space, the analyses yielded stringent constraints on the existence of dark vector bosons and new scalar particles. These results extend the sensitivity of previous searches and contribute valuable input for future experimental directions. The methodologies developed—including enhanced lepton and jet selection, robust background estimation, and detailed studies of cutoff effects—will serve as a solid foundation for future analyses at the LHC and other high-energy physics facilities.

In conclusion, this thesis drives forward the search for dark sector physics by delivering both novel experimental results and methodological advancements. While no conclusive evidence of new phenomena has yet been found, the work reinforces the scientific imperative for continued exploration and lays the groundwork for future discoveries in our quest to uncover the fundamental nature of the universe.

Bibliography

[1] ATLAS Collaboration. Search for a new scalar decaying into new spin-1 bosons in four-lepton final states with the atlas detector. *Physics Letters B*, 865:139472, 2025.

[2] ATLAS Collaboration. Search for Higgs bosons decaying into new spin-0 or spin-1 particles in four-lepton final states with the ATLAS detector with 139 fb^{-1} of pp collision data at $\sqrt{s} = 13$ tev. *Journal of High Energy Physics*, 03:041, 2022.

[3] ATLAS Collaboration. Measurement of ZZ production cross-sections in the four-lepton final state in pp collisions at $\sqrt{s} = 13.6$ TeV with the ATLAS experiment. *arXiv preprint*, 2023.

[4] ATLAS Collaboration. Measurement of the higgs boson mass in the $H \to ZZ^* \to 4\ell$ decay channel using 139 fb^{-1} of $\sqrt{s} = 13$ TeV pp collisions recorded by the ATLAS detector at the LHC. *Physics Letters B*, 843:137880, 2023.

[5] A high granularity timing detector for the atlas phase-ii upgrade. *INSPIRE High Energy Physics*, 2024.

[6] Asmaa Aboulhorma and Farida Fassi. Jet energy scale and resolution in the high-granularity timing detector in ATLAS upgrades at HL-LHC. *Andromeda Proceedings*, BSM 2021, 2021.

[7] ATLAS Collaboration. Search for new phenomena in events with an energetic jet and missing transverse momentum in pp collisions at $\sqrt{s} = 13$ tev with the atlas detector. *Phys. Rev. D*, 103:112006, 2021.

[8] Various. Quantum electrodynamics lagrangian. *Wikimedia Commons*, 2025. Accessed: 2025-03-09; Equation extracted from Standard Model Diagram.

[9] CERN. Origins of the Brout-Englert-Higgs mechanism. *CERN Website*, 2023.

[10] T. W. B. Kibble. Englert-brout-higgs-guralnik-hagen-kibble mechanism. *Scholarpedia*, 4(1):6441, 2009.

[11] A. M. Sirunyan et al. Measurements of the Higgs boson width and anomalous HVV couplings from on-shell and off-shell production in the four-lepton final state. *Phys. Rev. D*, 99:112003, 2019.

[12] LHC Higgs Cross Section Working Group. Lhc higgs cross section working group. *CERN TWiki*, 2018. Accessed: 2018-01-03.

[13] ATLAS Collaboration. The higgs boson visualization. *ATLAS Open Data*, 2025. Accessed: 2025-03-09.

[14] Ilya Tsukerman, for the ATLAS, and CMS Collaborations. Measurements of the higgs boson by atlas and cms. *Journal of Physics: Conference Series*, 1390(1):012030, 2019.

[15] ATLAS Collaboration. Observation of a new particle in the search for the Standard Model Higgs boson with the ATLAS detector at the LHC. *Phys. Lett. B*, 716:1–29, 2012.

[16] CMS Collaboration. Observation of a new boson at a mass of 125 gev with the cms experiment at the lhc. *Physics Letters B*, 716:30–61, 2012.

[17] Stephen P. Martin. A supersymmetry primer. *Advances in Series Direct High Energy Physics*, 18:1–98, 1998.

[18] Dan Hooper and Stefano Profumo. Dark matter and collider phenomenology of universal extra dimensions. *Physics Reports*, 453:29–115, 2007.

[19] Martin Schmaltz and David Tucker-Smith. Little higgs theories. *Annual Review of Nuclear and Particle Science*, 55:229–270, 2005.

[20] A. Boyarsky, M. Drewes, T. Lasserre, S. Mertens, and O. Ruchayskiy. Sterile neutrino dark matter. *Progress in Particle and Nuclear Physics*, 104:1–45, 2019.

[21] Edward W. Kolb. The early universe. *CRC Press Publications*, 2018. Book.

[22] D. Curtin and et al. Exotic decays of the 125 gev higgs boson. *Physical Review D*, 90, 2014. https://arxiv.org/pdf/1312.4992.pdf.

[23] H. Davoudiasl, H.-S. Lee, and W. J. Marciano. "dark" z implications for parity violation, rare meson decays, and higgs physics. *Physical Review D*, 85(11):115019, 2012. https://arxiv.org/pdf/1203.2929.pdf.

[24] D. Curtin, R. Essig, S. Gori, and J. Shelton. Illuminating dark photons with high-energy colliders. *Journal of High Energy Physics*, 2015, 2015.

[25] J. F. Gunion, B. Grzadkowski, H. E. Haber, and J. Kalinowski. Limits from lep data on icp/i-violating nonminimal higgs sectors. *Physical Review Letters*, 79:982–985, 1997.

[26] G. Bélanger, B. Dumont, U. Ellwanger, J. F. Gunion, and S. Kraml. Global fit to higgs signal strengths and couplings and implications for extended higgs sectors. *Physical Review D*, 88, 2013.

[27] L. Evans and P. Bryant. LHC machine. *JINST*, 3(08):S08001, August 2008.

[28] ATLAS Collaboration. Observation of a new particle in the search for the Standard Model Higgs boson with the ATLAS detector at the LHC. *Phys. Lett. B*, 716:1, 2012. arXiv:1207.7214 [hep-ex].

[29] CMS Collaboration. Observation of a new boson at a mass of 125 GeV with the CMS experiment at the LHC. *Phys. Lett. B*, 716:30, 2012. arXiv:1207.7235 [hep-ex].

[30] ATLAS Collaboration. Observation of $H \to b\bar{b}$ decays and VH production with the ATLAS detector. *Phys. Lett. B*, 786:59–86, 2018. arXiv:1808.08238 [hep-ex].

[31] CMS Collaboration. Observation of Higgs Boson decay to Bottom Quarks. *Phys. Rev. Lett.*, 121(12):121801, September 2018. arXiv:1808.08242 [hep-ex].

[32] ATLAS Collaboration. Observation of four-top-quark production in the multi-lepton final state with the ATLAS detector. *Eur. Phys. J. C*, 83(6):496, 2023. arXiv:2303.12812 [hep-ex].

[33] CMS Collaboration. Observation of four top quark production in proton-proton collisions at $\sqrt{s} = 13$ TeV. *arXiv preprint*, 2023. arXiv:2305.13439 [hep-ex].

[34] E. Mobs. The cern accelerator complex - august 2018. complexe des accélérateurs du cern - août 2018. *CERN Document Server*, August 2018. Accessed: 2025-03-09.

[35] ATLAS Collaboration. The ATLAS experiment at the CERN Large Hadron Collider. *JINST*, 3(08):S08003, August 2008. JINST 3 (2008) S08003.

[36] CMS Collaboration. The CMS experiment at the CERN LHC. *JINST*, 3(08):S08004, August 2008. JINST 3 (2008) S08004.

[37] LHCb Collaboration. The LHCb detector at the LHC. *JINST*, 3(08):S08005, August 2008. JINST 3 (2008) S08005.

[38] ALICE Collaboration. The ALICE experiment at the CERN LHC. *JINST*, 3(08):S08002, August 2008. JINST 3 (2008) S08002.

[39] G. Aad et al. The ATLAS experiment at the CERN Large Hadron Collider. *JINST*, 3:S08003, 2008. JINST 3 (2008) S08003.

[40] Maciej Wielgosz, Andrzej Skoczeń, and Matej Mertik. On the impact of selected modern deep-learning techniques to the performance and celerity of classification models in an experimental high-energy physics use case. *Nuclear Instruments and Methods in Physics Research Section A*, 982:164347, 2020. ResearchGate Link.

[41] ATLAS Collaboration. Studies concerning the ATLAS IBL calibration architecture. *ATL-INDET-PROC*, 2013. ResearchGate Link.

[42] ATLAS Collaboration. The ATLAS insertable B-Layer Technical Design Report. *CERN Technical Design Report*, (ATLAS-TDR-19), September 2010. ATLAS-TDR-19.

[43] Joao Pequenao. Computer generated image of the ATLAS calorimeter. *CERN Document Server*, March 2008. CERN-GE-0803013.

[44] G. Aad et al. The ATLAS experiment at the CERN Large Hadron Collider. *JINST*, 3:S08003, 2008. JINST 3 (2008) S08003.

[45] ATLAS Collaboration. Atlas tile calorimeter: technical design report. *CERN*, 1996. Technical Design Report, CERN-LHCC-96-042, ATLAS-TDR-3.

[46] ATLAS Collaboration. Commissioning of the atlas muon spectrometer with cosmic rays, 2010. Accessed: 2025-03-09.

[47] T. Colombo and ATLAS Collaboration. Data-flow performance optimisation on unreliable networks: the ATLAS data-acquisition case. *J. Phys. Conf. Ser.*, 608:012005, 2015.

[48] ATLAS Collaboration. Technical design report for the atlas inner tracker strip detector. *CERN*, 2017. Technical Design Report.

[49] ATLAS Collaboration. Atlas liquid argon calorimeter phase-ii upgrade: Technical design report. *CERN Reports*, 2017. Technical Design Report.

[50] ATLAS Collaboration. Technical design report for the phase-ii upgrade of the atlas muon spectrometer. *CERN Reports*, 2017. Technical Design Report.

[51] ATLAS Collaboration. Technical design report: A high-granularity timing detector for the atlas phase-ii upgrade. *CERN Reports*, 2020. Technical Design Report, CERN-LHCC-2020-007.

[52] ATLAS Collaboration. Plots from test beam measurement of atlas itk short strip module at warm and cold operational temperature. *CERN Document Server*, 2023.

[53] G. Pellegrini and et al. Technology developments and first measurements of low gain avalanche detectors (lgad) for high energy physics applications. *Nuclear Instruments and Methods in Physics Research A*, 765:12–16, 2014.

[54] ATLAS Collaboration.

[55] R. Frühwirth. Application of Kalman filtering to track and vertex fitting. *Nuclear Instruments and Methods in Physics Research Section A: Accelerators, Spectrometers, Detectors and Associated Equipment*, 262(2-3):444–450, 1987.

[56] Reconstruction and identification of electrons. *CERN Technical Reports*, 2009.

[57] ATLAS Collaboration. Measurements of $W^{\pm}Z$ production cross sections in pp collisions at $\sqrt{s} = 8$ TeV with the ATLAS detector and limits on anomalous gauge boson self-couplings. *ATLAS Conference Notes*, (ATLAS-CONF-2016-024), 2016.

[58] ATLAS Collaboration. Electron reconstruction and identification in the ATLAS experiment using the 2015 and 2016 LHC proton–proton collision data at $\sqrt{s} =$ 13 TeV. *The European Physical Journal C*, 79, 2019.

[59] A. Hocker et al. Tmva - toolkit for multivariate data analysis with root: Users guide. Technical report, CERN, Geneva, 2007. Cited on page 56.

[60] data set at $\sqrt{s} = 13$ tev. *Eur. Phys. J. C*, 81:578, 2021. 44 p.

[61] M. Cacciari, G. P. Salam, and G. Soyez. The anti-k_t jet clustering algorithm. *Journal of High Energy Physics*, 2008:063, 2008. Cited on page 61.

[62] M. Cacciari, G. P. Salam, and G. Soyez. The anti-k_t jet clustering algorithm. *JHEP*, 04:063, 2008.

[63] Atl-phys-pub-2022-038. *ATLAS Public Notes*, 2022.

[64] Tagging and suppression of pileup jets with the ATLAS detector. *ATLAS Conference Notes*, 2014.

[65] Selection of jets produced in 13 TeV proton-proton collisions with the ATLAS detector. *ATLAS Conference Notes*, (ATLAS-CONF-2015-029), Jul 2015.

[66] D. Krohn, J. Thaler, and L.-T. Wang. Jet trimming. *JHEP*, 02:084, 2010.

[67] M. Cacciari, G. P. Salam, and G. Soyez. The catchment area of jets. *JHEP*, 04:005, 2008.

[68] ATLAS Collaboration. Electron and photon energy calibration with the ATLAS detector using LHC Run 1 data. *Eur. Phys. J. C*, C74:3071, 2014.

[69] Electron efficiency measurements with the ATLAS detector using the 2015 LHC proton-proton collision data. *ATLAS Conference Notes*, 2016.

[70] ATLAS Collaboration. Measurement of the photon identification efficiencies with the ATLAS detector using LHC Run-1 data. *The European Physical Journal C*, 76, Dec 2016.

[71] ATLAS Collaboration. Identification and energy calibration of hadronically decaying tau leptons with the ATLAS experiment in pp collisions at $\sqrt{s} = 8$ TeV. *The European Physical Journal C*, 75, July 2015.

[72] ATLAS Collaboration. Performance of missing transverse momentum reconstruction with the ATLAS detector using proton–proton collisions at $\sqrt{s} = 13$ TeV. *The European Physical Journal C*, 78, Nov 2018.

[73] ATLAS Collaboration. Technical design report: A high-granularity timing detector for the ATLAS Phase-II upgrade. *CERN Technical Reports*, (CERN-LHCC-2020-007), 2020.

[74] ATLAS Collaboration. Overview of the atlas high granularity timing detector. *Technical Report*, (ATL-HGTD-PROC-2023-005), 2023.

[75] N. Cartiglia. Ultra-fast silicon detector. *Instrumentation Seminar*, 2015.

[76] I. Perić. A novel monolithic pixelated particle detector implemented in high-voltage cmos technology. *Nucl. Instrum. Meth. A*, 582:876–885, 2007.

[77] C. David. A new strips tracker for the upgraded atlas itk detector. *Technical Report*, 01, 2018.

[78] Technical design report for the atlas inner tracker strip detector. *Technical Report*, 2017.

[79] Usbtc08 logger. *Pico Technology*.

[80] Sht85 sensor. *Sensirion*.

[81] Raspberry pi 4. *Raspberry Pi Foundation*.

[82] Influx database. *Grafana Documentation*.

[83] Grafana open-source software. *Grafana Labs*.

[84] Electron reconstruction and identification in the atlas experiment using the 2015 and 2016 lhc proton-proton collision data at $\sqrt{s} = 13$ tev. *Eur. Phys. J. C*, 79(8):639, 2019.

[85] Muon reconstruction performance of the atlas detector in proton–proton collision data at $\sqrt{s} = 13$ tev. *Eur. Phys. J. C*, 76(5):292, 2016.

[86] W. Lampl et al. Calorimeter clustering algorithms: Description and performance. *Technical Report*, 2008.

[87] D. Boye. The search for a dark vector boson and a new scalar with the atlas detector. 2020.

[88] R. Contino, M. Ghezzi, C. Grojean, M. Mühlleitner, and M. Spira. ehdecay: An implementation of the higgs effective lagrangian into hdecay. *Computer Physics Communications*, 185:3412–3423, 2014.

[89] F. Siegert. Monte carlo tuning with atlas data. 2011.

[90] Systematic correction tools.

[91] ATLAS Collaboration. Measurement of the zz^* production cross section in proton-proton collisions at $\sqrt{s} = 13$ tev with the ATLAS detector. *CERN Report*, 2653360, 2020.

Résume

Cette thèse s'inscrit dans le cadre de la recherche de nouvelles particules au-delà du Modèle Standard, en s'appuyant sur les données de l'expérience ATLAS au Grand Collisionneur de Hadrons (LHC). L'analyse se concentre sur la recherche de bosons vecteurs sombres (Zd) et de nouveaux scalaires (S), à travers deux états finaux complémentaires : le canal entièrement leptonique ($ZdZd \to 4\ell$) et le canal semi-leptonique ($ZdZd \to 2\ell 2j$). Pour maximiser la sensibilité aux signaux recherchés, des techniques avancées de sélection d'événements et de reconstruction sont mises en œuvre. Les résultats sont interprétés dans le cadre du Modèle de Higgs Abélien Caché. Parallèlement à cette étude phénoménologique, la thèse comprend un volet instrumental dédié à l'amélioration des performances du détecteur ATLAS dans les conditions d'interactions multiples (pileup) attendues au LHC à haute luminosité. Des études sont menées sur l'échelle énergétique et la résolution des jets pour le Détecteur Temporel à Haute Granularité (HGTD), mettant en évidence des gains significatifs dans la région avant ($2.4 < \eta < 4$). En complément, une analyse des performances thermiques des modules à bandes du trajectographe interne (ITk), réalisée au Brookhaven National Laboratory (BNL), permet de contribuer à l'optimisation de la reconstruction des traces et des performances globales du détecteur dans un environnement à pileup élevé.

Mots-clefs (5) : LHC, New physics, Dark matter, Beyond Standard Model, ATLAS experiment.

Abstract

This thesis is dedicated to the search for new particles beyond the Standard Model, based on data from the ATLAS experiment at the Large Hadron Collider (LHC). The analysis focuses on the search for dark vector bosons (Zd) and new scalar particles (S), through two complementary final states: the fully leptonic channel ($ZdZd \to 4\ell$) and the semi-leptonic channel ($ZdZd \to 2\ell 2j$). Advanced event selection and reconstruction techniques are employed to maximize sensitivity to the targeted signals. The results are interpreted within the framework of the Hidden Abelian Higgs Model. In parallel with this phenomenological study, the thesis includes an instrumental component aimed at enhancing the ATLAS detector's performance under the high pileup conditions expected at the High-Luminosity LHC. Studies of the energy scale and jet resolution for the High Granularity Timing Detector (HGTD) show significant improvements in the forward region ($2.4 < \eta < 4$). Additionally, thermal performance analyses of strip modules for the Inner Tracker (ITk), conducted at Brookhaven National Laboratory (BNL), contribute to the optimization of track reconstruction capabilities and the overall detector performance in a high pileup environnement.

Keywords (5) : LHC, New physics, Dark matter, Beyond Standard Model, ATLAS experiment.